UNIVERSITÄT BONN

igg

Institut für Geodäsie und Geoinformation

Schriftenreihe

Analysis and mitigation of site-dependent effects in static and kinematic GNSS applications

Florian Zimmermann



60

Bonn 2020

Florian Zimmermann · **Analysis and mitigation of site-dependent effects in static and kinematic GNSS applications**

Diese Arbeit wurde am 29. Mai 2019 als Dissertation zur Erlangung des Grades Doktor der Ingenieurwissenschaften (Dr.-Ing.) der Landwirtschaftlichen Fakultät der Rheinischen Friedrich-Wilhelms-Universität Bonn vorgelegt.

Referent:	Prof. Dr.-Ing. Heiner Kuhlmann
1. Korreferent:	Prof. Dr.–Ing. Steffen Schön
2. Korreferent:	Prof. Dr.–Ing. habil. Volker Schwieger

Tag der mündlichen Prüfung: 2. September 2019

Diese Dissertation ist auf bonndoc - dem Publikationsserver der Universität Bonn elektronisch publiziert:
https://nbn-resolving.org/urn:nbn:de:hbz:5n-55736

Schriftenreihe des Instituts für Geodäsie und Geoinformation
der Rheinischen Friedrich-Wilhelms-Universität Bonn

Herausgeber: Prof. Dr. Jan-Henrik Haunert
Prof. Dr.-Ing. Theo Kötter
Prof. Dr.-Ing. Heiner Kuhlmann
Prof. Dr.-Ing. Jürgen Kusche
Prof. Dr. techn. Wolf-Dieter Schuh
Prof. Dr. Cyrill Stachniss

Die Aufnahme dieser Arbeit in die Schriftenreihe wurde von den Herausgebern der Reihe einstimmig beschlossen.

Dieses Werk ist einschließlich aller seiner Teile urheberrechtlich geschützt.
Abdruck auch auszugsweise nur mit Quellenangabe gestattet.
Alle Rechte vorbehalten.

Schriftenreihe Heft 60

Bonn 2020 2699-6685 (Online)

Institut für Geodäsie und Geoinformation

Analysis and mitigation of site-dependent effects in static and kinematic GNSS applications

Dissertation

zur

Erlangung des akademischen Grades

Doktor der Ingenieurwissenschaften (Dr.–Ing.)

der

Landwirtschaftlichen Fakultät

der

Rheinischen Friedrich–Wilhelms–Universität Bonn

vorgelegt von

M.Sc. Florian Zimmermann

aus Quito, Ecuador

Bonn 2019

Referent:	Univ.–Prof. Dr.–Ing. Heiner Kuhlmann
Korreferenten:	Univ.–Prof. Dr.–Ing. Steffen Schön
	Univ.–Prof. Dr.–Ing. habil. Volker Schwieger
Tag der mündlichen Prüfung:	02. September 2019

Angefertigt mit Genehmigung der Landwirtschaftlichen Fakultät der Universität Bonn

Publikation: Diese Dissertation ist auf dem Hochschulschriftenserver der ULB Bonn `http://nbn-resolving.de/urn:nbn:de:hbz:5n-55736` elektronisch publiziert.

Analysis and mitigation of site-dependent effects in static and kinematic GNSS applications

Abstract

Satellite signals are subject to various error sources on their way from the satellite to the receiving antenna. Nowadays, in many fields of application, the site-dependent parts, which can be separated into far-field multipath, NLOS reception and signal diffraction, the influence of the satellite geometry and antenna near-field effects, are one of the accuracy limiting factors in satellite-based positioning. This is due to the fact that the dependence on the individual antenna environment considerably impedes a minimization of the influences and established strategies, such as double-differencing in relative positioning approaches, are generally not applicable.
Although these effects have been subject to scientific research since the earliest developments in the field of satellite-based positioning, an all-embracing solution is still lacking. Therefore, this topic has not lost its relevance and there is still a need for further investigations to deepen the understanding and expanding the portfolio of available mitigation techniques.

In this dissertation, the four different effects are addressed against the background of high-precision static and kinematic GNSS applications. In this context, the main focus of the investigations is on the detection and exclusion of affected satellite signals, by integrating detailed environment models derived from terrestrial measurements. Based on these methodological and empirical analyses, four main aspects can be highlighted for the different effects:

- Since antenna near-field effects primarily affect the measuring sensor itself, and thus, the striven detection and exclusion for mitigation is not applicable in this case, alternatively the mitigation of the influence by special antenna setups is empirically analyzed. As a result, achievable accuracies in the sub-millimeter range can be demonstrated using exactly identical antenna setups.
- By simulating generic obstruction scenarios, the influence on the positional accuracy of the deterioration of the satellite geometry, potentially caused by an elimination of satellite signals, can be identified as uncritical. Furthermore, a method for integrating measures for the quality of the satellite geometry in the waypoint planning of UAVs is developed, which enables the adaption and optimization of the flight route in the planning phase, as well as during the UAV flight.
- Based on point clouds of terrestrial laser scanners, a method for the determination of elevation masks that are adaptive to the present antenna environment is developed, which enables an effective detection and exclusion of signals that are subject to NLOS reception or signal diffraction. This mitigation strategy can be applied to static and kinematic GNSS applications and by additionally integrating Fresnel zones, also the propagation characteristics of electromagnetic waves are considered.
- As a preparatory step for the development of methods for detecting and excluding far-field multipath, the prerequisites for the occurrence of the effect are investigated. By comparison of simulated and observed SNR time series and by considering Fresnel zones, an overlap of 50% between Fresnel zone and reflecting surface can be identified as already being sufficient for potential far-field multipath influences.

In the overall view, the findings and methods developed in this dissertation represent a relevant contribution to the superordinate goal of a holistic mitigation of site-dependent effects, and thus, enable a significant improvement of the positional accuracy under difficult GNSS conditions. In addition, this thesis adopts the currently forced trend from a pointwise to an area-based object acquisition by revealing and exploiting the potential of a detailed and efficient acquisition of the antenna environment by terrestrial laser scanners for mitigating and analyzing site-dependent effects in satellite based positioning applications.

Analyse und Minimierung stationsspezifischer Abweichungen bei statischen und kinematischen GNSS-Anwendungen

Zusammenfassung

Satellitensignale unterliegen auf ihrem Weg von der Satelliten- zur Empfangsantenne einer Vielzahl an Einflüssen die zu Abweichungen führen. Heutzutage stellen in vielen Anwendungsbereichen insbesondere die stationsspezifischen Anteile, welche sich in Mehrwegeeffekte aus dem Fernfeld, NLOS-Empfang und Signalbeugung, den Einfluss der Satellitengeometrie und Antennennahfeldeffekte untergliedern lassen, einen der genauigkeitsbegrenzenden Faktoren in der satellitengestützten Positionsbestimmung dar. Dies ist dadurch begründet, dass durch die Abhängigkeit von der individuell vorliegenden Antennenumgebung eine Minimierung der Einflüsse erheblich erschwert wird und etablierte Strategien, wie beispielsweise die Differenzbildung in relativen Positionierungsansätzen, in der Regel nicht anwendbar sind.
Obwohl diese Effekte bereits seit den frühesten Entwicklungen auf dem Gebiet der satellitengestützten Positionsbestimmung untersucht wurden, ist eine vollumfängliche Lösungsstrategie auch in der heutigen Zeit noch nicht verfügbar. Daher hat diese Thematik nicht an Relevanz verloren und es besteht noch immer der Bedarf an weiteren Untersuchungen zur Vertiefung des Verständnisses und zur Erweiterung des Portfolios an verfügbaren Minimierungsansätzen.

In dieser Arbeit werden die vier unterschiedlichen Effekte vor dem Hintergrund der hochpräzisen Positionsbestimmung in statischen und kinematischen GNSS-Anwendungen adressiert. Der wesentliche Fokus der Untersuchungen liegt hierbei auf der Detektion und Elimination betroffener Satellitensignale durch die Einbindung detaillierter Umgebungsmodelle aus terrestrischen Messverfahren. Auf Basis dieser methodischen und empirischen Analysen lassen sich für die einzelnen Effekte vier Hauptaspekte herausstellen:

- Da Antennennahfeldeffekte primär den Messsensor selbst beeinflussen und folglich die angestrebte Detektion und Elimination zur Minimierung nicht geeignet ist, wird alternativ die Minimierung des Einflusses durch spezielle Antennenaufbauten empirisch analysiert. Daraus resultierend werden mit exakt identischen Antennenaufbauten erreichbare Genauigkeiten im Submillimeterbereich nachgewiesen.
- Der Einfluss auf die Positionsgenauigkeit der potentiell durch eine Signalelimination hervorgerufenen Verschlechterung der Satellitengeometrie kann durch Simulationen generischer Abschattungsszenarien als unkritisch identifiziert werden. Darüber hinaus wird eine Methode zur Integration der Qualität der Satellitengeometrie in die Wegpunktplanung von UAVs entwickelt, welche sowohl in der Planungsphase, als auch während des UAV-Fluges eine Anpassung und Optimierung der Flugroute ermöglicht.
- Auf Basis mittels terrestrischer Laserscanner erzeugter Punktwolken wird eine Methode zur Erzeugung von Elevationsmasken entwickelt, welche adaptiv gegenüber der vorliegenden Antennenumgebung sind und eine effektive Detektion und Elimination von Satellitensignalen erlauben, die NLOS-Empfang oder Signalbeugung unterliegen. Diese Minimierungsstrategie ist sowohl in statischen, als auch kinematischen Anwendungen einsetzbar und ermöglicht bei zusätzlicher Einbindung von Fresnel Zonen auch die Berücksichtigung der Ausbreitungseigenschaften elektromagnetischer Wellen.
- Als vorbereitender Schritt für die Entwicklung von Methoden zur Detektion und Eliminierung von Fernfeld-Mehrwegeeffekten werden die Voraussetzungen für die Entstehung der Effekte untersucht. Durch Vergleich simulierter und beobachteter SNR-Zeitreihen und der Berücksichtigung von Fresnel Zonen kann eine Überlappung von 50% zwischen Fresnel-Zone und Reflektorfläche als bereits ausreichend für eine potentielle Mehrwegebelastung identifiziert werden.

In der Gesamtbetrachtung liefern die in dieser Arbeit gewonnenen Erkenntnisse und entwickelten Methoden einen relevanten Beitrag zu dem übergeordneten Ziel einer ganzheitlichen Minimierung stationsspezifischer Abweichungen und ermöglichen so eine signifikante Verbesserung der Positionsgenauigkeit unter schwierigen GNSS-Bedingungen. Darüber hinaus nimmt diese Arbeit den in den letzten Jahren forcierten Trend von einer punktweisen zu einer flächenhaften Objekterfassung an, indem das Potenzial einer detaillierten und effizienten Erfassung der Antennenumgebung mittels terrestrischer Laserscanner zur Minimierung und Analyse stationsspezifischer Abweichungen bei der satellitengestützten Positionsbestimmung aufzeigt und genutzt wird.

Contents

Preface **1**

1 Motivation and objectives **3**

1.1 Motivation . . . 3

1.2 Objectives . . . 5

2 Scientific context **7**

2.1 Studies on the satellite geometry . . . 7

2.2 Studies on far-field multipath . . . 8

2.3 Studies on NLOS reception and signal diffraction . . . 9

2.4 Studies on antenna near-field effects . . . 10

3 Theoretical basics **13**

3.1 Global Navigation Satellite Systems (GNSS) . . . 13

3.1.1 Observations and error budget . . . 13

3.1.2 Absolute and relative position determination . . . 14

3.2 Site-dependent effects . . . 16

3.2.1 Satellite geometry . . . 16

3.2.2 Far-field multipath . . . 17

3.2.3 NLOS reception and signal diffraction . . . 19

3.2.4 Antenna near-field . . . 20

3.3 Fresnel zones . . . 23

4 Content of relevant publications **29**

5 Summary of most important results **35**

5.1 Minimization of antenna near-field effects by appropriate measurement strategies 35

5.1.1 Design of field experiments 35

5.1.2 Analysis of results 36

5.1.3 Summary 38

5.2 Analysis of the influence of the satellite geometry and its consideration in kinematic applications 40

5.2.1 Influence of satellite obstructions on the positional accuracy 40

5.2.2 Optimized waypoint planning of UAVs 42

5.2.3 Summary 43

5.3 Mitigation of NLOS reception and signal diffraction in static and kinematic applications . . . 45

5.3.1 The concept of Obstruction Adaptive Elevation Masks 46

5.3.2 OAEM performance in static applications 51

5.3.3 OAEM performance in kinematic applications 54

5.3.4 OAEM determination without availabilty of georeferenced point clouds 56

5.3.5 Summary 61

5.4 Analysis of far-field multipath under consideration of Fresnel zones 63

6 Further considerations **69**

6.1 Integration of other GNSS 69

6.2 OAEM determination on mobile platforms 70

6.3 Advanced satellite selection based on Fresnel zones 71

6.4 Influence of antenna calibration parameters from different facilities 72

7 Conclusion and outlook **75**

8 List of further publications **79**

List of Figures **81**

List of Tables **83**

Abbreviations **85**

References **87**

Preface

This cumulative dissertation presents the investigations and results of the analysis and mitigation of site-dependent effects in static and kinematic GNSS applications. The thesis is based on the following five publications that were all subject to a peer-review process and are listed as category 1 publications in the Agricultural Faculty of the University of Bonn:

- Publication A (peer-review):
  Zimmermann, F., Eling, C., & Kuhlmann, H. (2016). Investigations on the Influence of Antenna Near-field Effects and Satellite Obstruction on the Uncertainty of GNSS-based Distance Measurements. *Journal of Applied Geodesy*, 10(1), 53–60

- Publication B (peer-review):
  Zimmermann, F., Eling, C., & Kuhlmann, H. (2017a). Empirical assessment of obstruction adaptive elevation masks to mitigate site-dependent effects. *GPS Solutions*, 21(4), 1695–1706

- Publication C (peer-review):
  Zimmermann, F., Eling, C., Klingbeil, L., & Kuhlmann, H. (2017b). Precise Positioning of UAVs–Dealing with challenging RTK-GPS measurement conditions during automated UAV flights. *ISPRS Annals of Photogrammetry, Remote Sensing & Spatial Information Sciences*, IV-2/W3, 95–102

- Publication D (peer-review):
  Zimmermann, F., Holst, C., Klingbeil, L., & Kuhlmann, H. (2018). Accurate georeferencing of TLS point clouds with short GNSS observation durations even under challenging measurement conditions. *Journal of Applied Geodesy*, 12(4), 289–301

- Publication E (peer-review):
  Zimmermann, F., Schmitz, B., Klingbeil, L., & Kuhlmann, H. (2019). GPS Multipath Analysis using Fresnel Zones. *Sensors*, 19(1), 25

The publications are summarized in Chapter 4 and in Chapter 5, the most important aspects and results are emphasized. The author of this dissertation has made the main contribution to all publications and in particular provided the respective methodological progress. In Publication C, the author of this dissertation is responsible for all methodical statements regarding the usage of obstruction adaptive elevation masks in kinematic GNSS applications. The development and analysis of the geometry maps was done in collaboration with the coauthors.

1. Motivation and objectives

From the earliest developments in the early 1960s to the present, satellite based positioning and navigation has become an indispensable part of the modern society. At the latest after the deactivation of the selective availability (SA) mode in May 2000, the American Global Positioning System (GPS) and, at times, the Russian counterpart Global'naya Navigatsionnaya Sputnikova Sistema (GLONASS) , enabled instantaneous positioning around the globe [Teunissen & Montenbruck, 2017]. Both are following the principle idea that if the position of the satellites is known and the distance between the satellite and an antenna on the earth can be measured using a transmitted satellite signal, the position of the user antenna can be determined. As a consequence, the usage of satellite based positioning techniques in various civilian and scientific applications rapidly increased in the last decades.
Geodesy and surveying was one of the fields of application where the highest accuracy requirements lead to essential improvements in satellite-based positioning [Ashkenazi, 2006]. The development of differential carrier-phase based techniques enabled the mitigation or at least minimization of the majority of errors influencing the positional accuracy and millimeter to centimeter accurate positioning solutions could be achieved after long observation durations and good measurement conditions [Leick et al., 2015]. Nowadays, site-dependent effects are still one of the accuracy limiting factors in GNSS applications. Although these effects have been subject to scientific research for decades and numerous methods and mitigation techniques have already been developed, a comprehensive and all-embracing solution of this problem is still lacking [Smyrnaios et al., 2013]. Due to the high dependency of the effects on the local antenna environment and the addressed applications, there is still a need for further investigations on this topic to increase the understanding of the different effects and to enlarge the amount of available mitigation techniques.
This dissertation contributes to the achievement of this overarching goal. Particularly, the detection and exclusion of affected signals using precise 3D information about the antenna environment is investigated. The motivation for these investigations and the resulting objectives are explained in more detail in the following Sections 1.1 and 1.2.

1.1 Motivation

Site-dependent effects is a collective term for error sources that are influencing the satellite signals and the accuracy of the position determination individually, depending on the specific antenna location. Imaging two antennas that are placed within a distance of a few kilometers to each other, it can be assumed that due to the large distance of approximately 20000 km between the satellite and the antennas, the satellite signal will propagate along almost the same path. Therefore, the influence of the atmosphere on the signal will be similar along both line-of-sights. In contrast, the local environment at both antennas usually differs from each other and consequently, also the errors arising from the antenna environment will be different [Hofmann-Wellenhof et al., 2008]. Site-dependent GNSS effects can be divided into four categories:

1) **Satellite geometry** – the distribution of the available satellites in the sky can be deteriorated by obstacles in the antenna environment.
2) **Far-field multipath** – the direct signal is superimposed by a reflected signal that reaches the antenna on one or more indirect paths.
3) **Non-line-of-sight reception and signal diffraction** – the direct signal path is blocked and the antenna receives only a reflected signal (NLOS reception) or the satellite signal is diffracted at the edge of an obstacle.
4) **Antenna near-field effects** – the phase center characteristic of the antenna is influenced by the closest vicinity of the antenna.

In the following, some of the main reasons for the increasing relevance of these effects are given and the reasons for the fundamental procedure of this dissertation are described. In particular, this includes reasons for the integration of environment models, which result from developments in the recent years in the field

of sensor technology and open data, and arguments for the decision to develop minimization strategies that rest on detection and elimination algorithms. On the basis of these preliminary considerations, the objectives of this dissertation are formulated and specifically defined for the individual effects in Section 1.2.

Reasons for the increasing relevance of site-dependent effects

One of the main reasons for the increasing relevance of site-dependent effects lies in the steadily growing number of application areas in which high-precision GNSS-based coordinate solutions are required. In the classical fields of geodesy, such as reference frame observations or establishment of reference station networks [Bruyninx, 2004; Feldmann-Westendorff et al., 2016], the GNSS observation conditions were, and still are, one of the key factors for the site selection [IGS, 2015]. That means, the antenna is placed preferably far away from reflecting surfaces and a nearly free horizon is targeted . Hence, ground-reflected signals are the main observation error arising from the environment, which can be minimized by a sufficiently long observation duration and a specialized antenna design [Seeber, 2003; Filippov et al., 1998; Kunysz et al., 2000]. In many other areas of application, the observation conditions need to be subordinated, since either such antenna locations cannot be found in the working environment, or, due to the location of the object of interest, unfavorable GNSS conditions cannot be prevented at all [Georgiadou & Kleusberg, 1988; Kersten & Schön, 2017]. At the same time, the accuracy requirements remain high, leading to an increasing demand of advanced mitigation techniques. A typical example for challenging GNSS conditions are urban scenarios, where in addition to a degraded satellite geometry and ground-based reflections, the signals can be reflected from arbitrarily oriented surfaces and diffraction effects and non-line-of-sight (NLOS) reception can occur, if the direct signal path is blocked [Groves et al., 2013].

A further reason for the growing importance of site-dependent effects is the transition from static to kinematic measurements, which has been increasingly forced in recent years, [Kuhlmann et al., 2014]. Although techniques, such as fast ambiguity resolution [Verhagen & Teunissen, 2006] or network-based real-time-kinematic (RTK) positioning [Wanninger, 2006; Rizos, 2002], substantially facilitate kinematic GNSS applications, the advantages of static measurements, i.e. high redundancy and a changing satellite constellation, do not exist anymore. In the context of kinematic GNSS positioning and site-dependent effects, the advent of autonomous mobile mapping applications, i.e object acquisition from a moving platform without any user intervention, represents one of the most challenging tasks in the field of engineering geodesy [Klingbeil et al., 2014b; Kuhlmann & Klingbeil, 2016]. For a safely and fully autonomous navigation of the vehicle, an accurate satellite-based position estimation is essential, especially in a case of emergency, when an intervention from the user-side is not possible [Eling, 2016].

Reasons for the integration of antenna environment models

Using a model of the antenna environment in mitigation approaches seems to be reasonable, since site-dependent effects are highly depending on the local environment. Nevertheless, often this implies the acquisition of the antenna environment with terrestrial measurements, which can entail a very time- and cost-consuming process, especially when the antenna environment has a complex structure and additional measurements are necessary to transform the environment model to a global coordinate frame. In recent years, the technical developments in the area of terrestrial laser scanners (TLS) were driven by the change from a pointwise to an area-based acquisition of objects [Holst, 2015]. Thus, nowadays, affordable and efficient laser scanners are available that enable a fast, precise and detailed acquisition of the surrounding environment [Burghof, 2018]. For this reason, the integration of a highly detailed model of the antenna environment into minimization approaches should not be considered as an additional time-consuming and complex task, but rather as a logical step that accounts for current developments in the field of TLS.

A further reason is the constantly increasing number of freely available georeferenced 3D models, especially in urban regions. For example, the Land Surveying Office of North Rhine-Westphalia, Germany, provides 3D building models in different levels-of-detail (LOD) from aerial flights, freely accessible for the entire state

territory[1]. The use of these models has already been established in various fields of application [Biljecki et al., 2015] and especially in the field of urban navigation they are frequently used to improve the position determination under difficult GNSS conditions [Bourdeau et al., 2012; Wang et al., 2013; Groves, 2016]. It is obvious that the accuracy and resolution of LOD models are not comparable to dense TLS point clouds. Nevertheless, they represent an alternative opportunity to integrate the antenna environment into the data processing process, even for high-precision GNSS applications.

Reasons for detection and exclusion strategies

In the next few years, there will be four Global Navigation Satellite Systems (GNSS) globally available for the satellite-based position determination. Besides the American GPS and the Russian GLONASS system, in 2019, the European Galileo system will reach is fully operational constellation (FOC) status, consisting of 26 satellites and together with the Chinese BeiDou system, leading to an enormous increase of available satellites [Teunissen & Montenbruck, 2017]. As a consequence, a profound and careful selection of satellite signals, which are not influenced by site-dependent effects, could become more important in the future. Even with a conservative estimate of 20 available satellites at a certain location, 10 satellites would still be available if 50 percent are excluded after these signals have been identified as being subject to one or more of the aforementioned effects. In comparison, this roughly corresponds to the current average availability of GPS satellites, whereby no selection of unaffected signal was made here [Santerre et al., 2017]. Consequently, the question arises if it is still necessary to integrate heavily influenced satellite signals into the position determination and trying to minimize their negative influence by, for example, special filtering or weighting strategies [Brunner et al., 1999; Lau & Cross, 2006]. Instead, detecting and excluding affected satellite signals could be more expedient in this context.

1.2 Objectives

The main objective of this dissertation is the development of analysis and mitigation strategies for the four site-dependent GNSS effects, categorized in Section 1.1. Therefore, in view of multi-GNSS availability and considering that a model of the antenna environment is available, a solid detection and exclusion strategy is targeted. This results in the following specific objectives that can be formulated for each site-dependent effect:

1. **Analysis of the influence of the satellite geometry and its consideration in kinematic applications**

   The exclusion of satellite signals can deteriorate the quality of the satellite geometry. Therefore, the extend of this influence needs to be analyzed and quantified beforehand to ensure that a detection and exclusion strategy to improve the positional accuracy does not have the opposite effect. Furthermore, measures for the quality of the satellite geometry are often used to predict the expectable measurement conditions at a certain location and can be applied as one criteria in the site-selection process. Nevertheless, if satellite positions are predicted, e.g. with the parameters from an almanac, the antenna environment needs to be taken into account to obtain preferably realistic estimates of the quality measures. Therefore, in this dissertation, the consideration of the quality of the satellite geometry in conjunction with the antenna environment is investigated in the context of the waypoint planning of unmanned aerial vehicles (UAV).

2. **Mitigation of NLOS reception and signal diffraction in static and kinematic applications**

   The origin of NLOS reception and signal diffraction is the blockage of the direct line-of-sight path between the satellite and the user antenna. Hence, possible blocking sources in the antenna environment need to be identified to perform a geometrical visibility check of the received satellite signals. For this

[1] https://www.bezreg-koeln.nrw.de/brk_internet/geobasis/hoehenmodelle/

step, the aforementioned environment models can be utilized. Therefore, one of the major goals of this thesis is to develop a method for the detection and exclusion of NLOS reception and signal diffraction, which integrates such environmental models and considers the propagation characteristics of electromagnetic waves. Furthermore, the developed method shall be applicable in both, static and kinematic GNSS applications.

3. **Analysis of far-field multipath under consideration of Fresnel zones**

   The detection of satellite signals that are affected by far-field multipath can indirectly be performed by identifying potential reflectors in the antenna environment, contributing to the reflection process. Besides tracing the satellite signals from the geometrical optics view, this identification process requires in-depth knowledge on the relation between the occurrence of far-field multipath and the size, orientation and roughness of the reflecting surface. The empirical investigation of this relation represents a further objective of this dissertation and can be understood as a necessary preparatory step for the development of a detection and exclusion algorithm for mitigating far-field multipath. In this context, particularly the concept of Fresnel zones shall be considered and the accordance with theoretical assumptions shall be scrutinized.

4. **Minimization of antenna near-field effects by appropriate measurement strategies**

   In comparison to the objectives 1 to 3, antenna near-field effects are a special case in the context of mitigating site-dependent effects. On the one hand, the measuring sensor itself is influenced by the immediate surrounding of the antenna, and thus, all received satellite signals are affected in this case. On the other hand, objects in the closest vicinity of the antenna are reflecting the received signals. Due to the small distance to the antenna, it is very likely that all signals are affected as well. Consequently, a satellite selection strategy based on the antenna environment is not an option for the mitigation of antenna near-field effects. Alternatively, the possibility of minimizing antenna near-field effects by means of advanced measurement strategies is empirically analyzed in this dissertation.

These objectives and preliminary considerations are taken up repeatedly in the course of the work and are addressed in particular in Chapter 5.

The scientific context relevant to this dissertation is presented in Chapter 2. Chapter 3 describes the theoretical basics of the satellite-based position determination and provides a detailed description of the site-dependent effects, as well as of the concept of the Fresnel zones, which is relevant in this context. The five first-author publications, founding the core of this dissertation, are briefly summarized in Chapter 4. Chapter 5 highlights the most important aspects of the publications, specifically with reference to the previously defined objectives of this thesis. Chapter 6 gives an overview of further considerations, which have arisen in the course of the work, but have not been considered in detail so far. The dissertation ends with a conclusion and outlook (Chapter 7) as well as a list of other publications not directly in the focus of this dissertation (Chapter 8).

2. Scientific context

Since the beginnings of satellite-based positioning and the advent of GPS, the influence of site-dependent effects on satellite signals have been subject to scientific research and its relevance for high precision applications is well known. For example in 1988, Georgiadou & Kleusberg [1988] stated that for short baseline applications, 'distance independent measurement errors originating in the receiving equipment and its immediate environment will contribute the major portion of the total error budget'. Although in the following three decades a large number of studies on this topic were carried out and a variety of publications were published, the topic has not lost its relevance.
Many of the approaches developed are often highly specialized and focus on a particular application or problem. Since the term site-dependent effects actually covers the four different effects mentioned in Chapter 1, which partially differ in their origin and impact on the observations, this is a logical consequence, since an all-embracing solution strategy does not seem attainable. Nevertheless, some approaches to mitigate or analyze the individual effects have proven to be very promising and effective. In the following Sections 2.1 – 2.4, an excerpt of these approaches, as well as some studies that are closely related to the strategies developed in this dissertation, are briefly described.

2.1 Studies on the satellite geometry

In the early days of GPS, forecasting the available satellite constellation and assessing its quality in terms of dilution of precision (DOP) values was an important and indispensable step in project planning [Seeber, 2003]. In order to identify and avoid observation periods with unfavorable measurement conditions, the almanac data of the GPS satellites could be used to precompute and analyze the satellite positions.
Based on the prototype GPS constellation available in 1984 and for the planned fully operational GPS constellation, the impact of the satellite geometry on the propagation of different systematic errors is analyzed in a sophisticated simulation approach in Santerre [1991]. One of the main findings was the proof of the high correlation between the relative tropospheric zenith delay, the clock parameters and the station height.
In [Abraha et al., 2016], the impact of satellite obstructions on the accuracy of long-term precise point positioning (PPP) solutions is analyzed. Therefore, the obstruction profile of a site of the International GNSS Service (IGS) with limited satellite visibility is extracted and simulated on the observations of several globally distributed and unobstructed IGS sites. It is shown that the impact of satellite obstruction depends on the latitude of the analyzed station. Furthermore, with values up to 8 millimeters, the root-mean-square (RMS) of the up-component is more affected than the east and north components, respectively.
Since this dissertation focuses on short baseline applications, a similar analysis is carried out for this case in Publication A [Zimmermann et al., 2016], whereby instead of one site-specific obstruction profile, four generic obstruction scenarios are simulated on observations collected under ideal measurement conditions.

Although DOP values only allow for a rough estimation of the expectable positional accuracy, they are still frequently used as an criterion to assess the quality of antenna locations. For example, a decree to the North Rhine-Westphalian law on cadastral surveying specifies a maximum permissible positional DOP (PDOP) value of 6 [SMBI.NRW, 2017]. In the context of unmanned aerial vehicles (UAV), the quality of the satellite geometry is one of the parameters considered when assessing the planned flight path in terms of efficiency and safety. Since the navigation of the UAV mainly depends on satellite-based positioning, unexpected obstructions of satellite signals can deteriorate the positional accuracy and therefore, lead to safety-critical situations, or can negatively influence the accuracy of the mapping product. In Gandor et al. [2015], a mission planner for UAVs is presented, where for certain waypoints and time stamps the satellite positions are forecasted using the data of an almanac and the actual satellite visibility is checked using a digital terrain model. This allows for a spatial and temporal optimization of the trajectory in advance of the UAV flight. However, in applications, such as exploration or fully autonomous mapping, the UAV needs to frequently adapt the flight path on its own in real-time [Nieuwenhuisen & Behnke, 2015], and thus, the satellite visibility cannot be assessed in advance.

To overcome this issue, geometry maps are determined in Publication C [Zimmermann et al., 2017b]. Under the assumption that the 3D environment of the region of interest is either a-priori known from a given 3D model, or reconstructed during the UAV flight based on the measurements of the onboard sensors, a visibility analysis is performed. The result is a grid of PDOP values, which can contribute to the decision-making process with the aim to find the best flight path for surveying and mapping applications at any location.

2.2 Studies on far-field multipath

Far-field multipath occurs when the direct satellite signal that has arrived through the line of sight (LOS) path is superimposed by a reflected signal that reaches the antenna on one or more indirect paths. Due to the motion of the satellite, this leads to a short periodic error in both, the observation and coordinate domain, whereby the period and the magnitude of the error mainly depend on the satellite-antenna-reflector geometry [Smyrnaios et al., 2013]. A more detailed description of far-field multipath is given in Section 3.2.2.

The majority of far-field multipath mitigation techniques are either data-driven approaches, or they are related to the receiver architecture, such as different correlator spacings or the Multipath Estimation Delay-Lock-Loop [Irsigler, 2008] or special antenna designs [Kunysz et al., 2000; Bedford et al., 2009; Rao et al., 2013; Zhang & Schwieger, 2017]. Nevertheless, the most straight forward and intuitive way of mitigating far-field multipath is to place the antenna in an ideally multipath-free environment, i.e. an area with free horizon and without any reflecting materials. However, in the vast majority of applications this ideal antenna environment cannot be found and even in case of a nearly free horizon, ground reflections can still have a significant impact on the positioning solution [Hartinger, 2001]. Far-field multipath typically appears as an oscillation in the coordinate or observation residuals with a period of approximately 5 to 30 minutes, whereby the period length mainly depends on the satellite-antenna-reflector constellation [Eissfeller, 1997; Ray & Cannon, 1999]. Due to its periodic characteristic, the far-field multipath error can largely be reduced by averaging over a sufficient long observation duration. However, in applications where the antenna is moving, the configuration rapidly changes and, thus, minimization by averaging is not an option [Hofmann-Wellenhof et al., 2008]. The same holds for applications where high-rate observations of a static antenna need to be processed kinematically and therefore, averaging cannot be applied [Wübbena et al., 2001].
Already in the early days of GPS, the use of the repeatability of the satellite constellation has gained attention. Under the assumption that the antenna environment and the antenna position do not change, the far-field multipath effect will recur approximately after one sidereal day [Hofmann-Wellenhof et al., 2008]. By correlating and subtracting the GPS time series or observations of two consecutive days, it becomes possible to determine corrections to minimize the far-field multipath error in both, the coordinate and the observation domain [Bock, 1991; Choi et al., 2004; Lau, 2012]. The main challenge in the context of sidereal filtering is the determination of the exact repeat time of each satellite. Since the repeat time varies by system and satellite, this approach will become very complex, especially in view of multi-GNSS applications [Agnew & Larson, 2007; Knöpfler, 2015].
Multipath stacking techniques also take advantage of the repeatability of the satellite constellation. Under the same assumptions, i.e. an unchanged antenna environment and position, the phase-residuals of long-term PPP solutions are allocated to an azimuth and elevation grid and after a robust aggregation, the multipath environment can be mapped to a skyplot [Fuhrmann et al., 2015; Dong et al., 2016]. Afterwards, these multipath stacking maps can be used to identify multipath emitting areas by direction and to determine observation corrections based on the incidence angle of the satellite [Fuhrmann et al., 2015; Dong et al., 2016]. Especially for permanent stations, multipath stacking maps are a suitable technique, since long observation durations are necessary for a complete coverage of the hemisphere.
In 2001, Böder et al. [2001] proposed an approach known as absolute station calibration, where an antenna on a moving robot is used to decorrelate the influence of the respective far-field multipath and in a second step, to calibrate a nearby reference station for the multipath error. Although practical experiments demonstrated a significant reduction of the effect, the high effort and costs prevented the implementation as an operative procedure.
A further approach to reduce multipath effects is to use several closely spaced antennas, so-called antenna

arrays [Ray et al., 1999]. Here, the temporal and spatial correlations of the multipath effect at the antennas are used to derive correction values, either in the observation or in the coordinate domain [Ray et al., 1999; Zhang & Schwieger, 2016]. In the case of a single dominant reflector, a significant reduction of the multipath effect can be achieved with these techniques [Zhang, 2016].
If a model of the antenna environment is available, ray-tracing techniques can be applied in order to analyze the signal paths between given satellite and antenna positions [Bradbury et al., 2007; Lau & Cross, 2007]. By determining the reflection points on the reflecting surfaces in the antenna surroundings, possible paths of reflected signals can be identified from a geometrical point of view. Hence, ray-tracing enables an assessment of the multipath level at certain positions. Furthermore, based on additional knowledge of the dielectric properties of the reflecting materials, observation corrections can also be derived.
However, the occurrence of far-field multipath mainly depends on the roughness of the reflecting surface and the size of the active scattering region, which can be determined using the concept of Fresnel zones. That means, from a theoretical point of view, only if the reflecting surface is smooth and large enough, multipath can occur [Hannah, 2001]. Since the majority of the aforementioned mitigation techniques deal with signals that are already affected by multipath, the Fresnel zones are seldom taken into account.
This gap is one of the aspects that is addressed in this dissertation. Especially in view of an advanced satellite signal selection, an essential step is the identification of potential reflectors in the antenna environment. Therefore, the theoretical prerequisites for multipath occurrence are empirically investigated and scrutinized in Publication E [Zimmermann et al., 2019].

2.3 Studies on NLOS reception and signal diffraction

The main difference between far-field multipath and the NLOS and diffraction effects is their independence from the direct signal (cf. Figures 3.3/3.4, pp. 18/19). The receiver interprets the affected signals as signals that are propagating on the direct signal path, although it actually only receives indirect signals. Hence, the resulting error is theoretically unbounded and cannot be avoided by special hardware design. Similar to far-field multipath, a careful site selection is the most straight forward way of minimizing both effects. Nevertheless, also very distant objects, such as buildings or mountain ridges can cause NLOS reception and signal diffraction [Klostius et al., 2006; Strode & Groves, 2016].
NLOS reception is a very common phenomena in dense urban areas that can significantly deteriorate the positioning solution [Groves, 2013]. In stand-alone GNSS applications, such as navigation or distinguishing between pedestrian walkways and traffic lanes, where accuracies on the meter level are sufficient, often 3D building models are used to predict the satellite availability or to detect signal deteriorations in order to improve the positioning solution [Bourdeau et al., 2012; Groves et al., 2012; Wang et al., 2013]. Alternatively, the satellite visibility can be determined from camera systems that are aligned to the zenith direction or are equipped with fish-eye lenses [Meguro et al., 2009; Moreau et al., 2017]. These techniques can be used to efficiently enhance the navigation solution on the meter level.
Signal diffraction is usually associated with a significant drop in signal strength [Wieser, 2002]. Hence, in several studies, the signal-to-noise ratio (SNR) has been used to improve the stochastic model of GNSS observations. A very well-known example is the SIGMA-Δ model, proposed in Brunner et al. [1999]. Herein, the differences between measured SNR values and a SNR template function are integrated into the variance model of the undifferenced GPS observations, whereby the template function represents the highest SNR values of a signal at certain elevations and of a specific antenna-receiver combination. Consequently, a high difference between the template function and the measured SNR indicates signal diffraction and inflates the variance of the respective phase observation. The effectiveness of the SIGMA-Δ model is mainly limited by the amount of contaminated signals and the complex relationship between signal attenuation and phase observation errors [Wieser, 2002].
A further approach to minimize the influence of signal diffraction and NLOS reception is to replace the standard fixed-angle elevation mask with an azimuth-dependent elevation mask that represents the physical horizon from the antenna point of view. In Klostius et al. [2006], the azimuth-dependent elevation mask was determined using theodolite measurements and compared to a high fixed-angle elevation mask in mountainous regions. It was found that the azimuth-dependent elevation mask mitigates diffraction effects and leads to

a higher positional accuracy, since the negative impact on the satellite geometry is lower compared to a high constant cut-off angle. In Kersten & Schön [2017], the derivation of dynamic and azimuth-dependent elevation masks without terrestrial measurements directly from the measured SNR values is proposed. By comparing the SNR values to template functions generated under laboratory conditions, outliers can be erased and afterwards, the dynamic elevation mask can be determined by interpolating between the lowest elevations of the remaining SNR signals of the individual satellite tracks. The approach was tested in several urban scenarios, and it was shown that the quality of a network solution can be improved after application of the dynamic elevation masks to the carrier-phase observations.
Although both approaches work well, they have two drawbacks. In Klostius et al. [2006] the corresponding azimuth and elevation values of the physical horizon are measured with a theodolit, which can become very time- and cost-consuming if the antenna environment is complex. Furthermore, the antenna position needs to be known and positional uncertainties are not considered. In Kersten & Schön [2017], the physical horizon is determined from the measured SNR values. On the one hand, this makes the elevation mask adaptive to changes in the antenna environment. On the other hand, the spatial resolution of the SNR values is limited by the available satellite tracks and an interpolation is necessary to determine the complete dynamic elevation mask. Consequently, the coincidence between the elevation mask and the actual physical horizon may decrease during short observation periods.
The approach followed in the context of this dissertation is very similar in principle, whereby in Publications B – E [Zimmermann et al., 2017a,b, 2018, 2019] terrestrial laser scans are used and the problems mentioned above are explicitly addressed and investigated during the development of the respective mitigation strategies.

2.4 Studies on antenna near-field effects

Investigations on antenna near-field effects are usually linked to the calibration of the antenna with respect to the antenna phase center offset and variations. Nowadays, antenna calibrations are either performed on a robot [Wübbena et al., 2000], or in an anechoic chamber [Zeimetz, 2010].
By comparing the phase center offset (PCO) and phase center variation (PCV) values of the same antenna, but calibrated with different near-field situations, i.e. including tribrach, adapters, etc., the magnitude of the near-field effect with respect to the standard setup can be determined [Schmitz et al., 2004; Dilßner, 2007; Zeimetz & Kuhlmann, 2008]. Nevertheless, the calibration parameters are only valid for the actual near-field situation present during the calibration procedure [Aerts et al., 2016]. Therefore, a preferably realistic reproduction of the near-field situation of the observation site during the antenna calibration enables the determination of site-specific calibration patterns and thus a minimization of near-field multipath [Wübbena et al., 2006]. However, due to size and weight limitations of the calibration facilities, the feasibility of this approach is often limited.
Since calibration parameters are provided by different facilities, their consistency among each other, as well as with type mean values is often scrutinized and investigated, leading to partially ambiguous results. In Baire et al. [2014], the calibration parameters of six antennas derived from robot and chamber calibrations are compared and the results indicate that the differences of several millimeters in both, the coordinate domain and the calibration parameters, are related to different near-field effects.
In Kallio et al. [2018], antenna calibration parameters from different facilities are compared using the observations collected at a special pillar network, called Revolver [Jokela et al., 2016]. By swapping and rotating the antennas on the concrete pillars in several observation sessions, residual offsets of the calibration patterns in the sub-millimeter range are determined if calibrations patterns from the same facility are used. The influence of calibration patterns from different facilities in the coordinate domain is determined in a zero baseline test, leading to differences that are slightly lower than the differences documented in Baire et al. [2014].
For a set of three geodetic antennas, Becker et al. [2010] show a consistency better than one millimeter between robot and chamber calibrations, whereas the comparison of type mean values of 15 antenna types, derived from robot or chamber calibrations, presented in Aerts & Moore [2013] reveals inconsistencies in the range of several millimeters.
Without considering antenna calibration parameters, Elósegui et al. [1995] investigate the influence of signal

scattering on permanent stations. It is demonstrated that reflections from the pillar surface lead to substantial errors in the vertical coordinate component and that microwave absorbing material on the top of the pillar helps to reduce the influence of near-by reflections. On the other hand, in [Aerts et al., 2016], it is shown that absorbing material in the reactive near-field of the antenna can influence the respective phase center characteristics.

Consequently, from the in parts contradictory results of the aforementioned studies, two conclusions can be drawn: 1) To prevent erroneous results, a careful and adequate comparison of the antenna calibration patterns from different facilities is necessary [Schön & Kersten, 2013]. Furthermore, Kersten & Schön [2016] recommend to analyze the impact on all estimated parameters, such as coordinates, clocks, tropospheric parameters and ambiguities by means of generic patterns. 2) In applications where high accuracy at the millimeter to sub-millimeter level is required, the near-field effects during the antenna calibration procedure, as well as arising from the antenna monumentation are one of the most critical factors.

In the framework of this dissertation, the latter aspect is addressed in Publication A [Zimmermann et al., 2016] by means of investigations on special antenna setups in the context of high-precision GNSS-based distance measurements.

3. Theoretical basics

This dissertation presents different methods for the analysis and mitigation of site-dependent GNSS effects, with a focus on static and kinematic short baseline applications. Amongst several other error sources, site-dependent effects are only one part of the GNSS error budget. However, since they usually cannot be mitigated by standard observation processing techniques, like e.g. double-differencing, the development of specialized analysis and mitigation techniques is of particular interest. This chapter presents the theoretical basics for the methods, developed in this thesis.

First, in Section 3.1, a brief overview on GNSS observations, the error budget and positioning techniques is given. In Section 3.2, the different site-dependent effects are explained in detail and in Section 3.3, the concept of Fresnel zones is introduced.

3.1 Global Navigation Satellite Systems (GNSS)

Besides the American GPS, several other satellite systems, such as the Russian GLONASS, the European Galileo or the Chinese BeiDou system can be used to estimate the position of a user antenna. Although each of these Global Navigation Satellite Systems (GNSS) differs in the technical realization, the basic principle is the same. By measuring the transit time of a transmitted signal and under the assumption that the positions of the transmitting satellites are known, the user can estimate its position, based on the concept of trilateration [Misra & Enge, 2001].

As it is also the case for any other geodetic measurement and positioning system, like e.g., TLS or tacheometers, the observations are affected by several error sources, influencing the positional accuracy. Therefore, in Section 3.1.1, the GNSS observations and the related observation errors are explained and in Section 3.1.2, different positioning techniques are briefly described. The methods and algorithms, developed in this dissertation, are tested and evaluated using GPS observations only. Thus, the description of the aforementioned aspects also focuses on GPS.

3.1.1 Observations and error budget

Generally, the GPS system provides two types of observations: 1) code observations and 2) carrier-phase observations. The code observations are a measure of the distances between the user and the satellites and are derived from the transit time, determined from the correlation of the received code-signal and a replica signal, generated by the receiver. Since all code observations at an instant of time have a common bias, the receiver clock error, they are also called pseudoranges. This phenomena is addressed later in this section. Carrier-phase observations are the phase differences between the receiver-generated carrier signal and the transmitted carrier signal of the satellite [Teunissen & Montenbruck, 2017]. Both observation types are subject to errors sources that can be divided into four groups:

1.) Satellite errors
Satellite errors include all errors that are related to the transmitting satellite. This includes the error of the satellite orbits and the satellite clock error, denoting the difference between the satellite atomic clock and the GPS reference time (Broadcast orbits and clocks $\approx 1\,m \ldots 2\,m$). Furthermore, due to the motion of the satellite on an eccentric orbit and the resulting change of the gravitational potential, relativistic effects are influencing the satellite clocks [Teunissen & Montenbruck, 2017].

2.) Atmospheric errors
The atmosphere can be divided into the dispersive part, called ionosphere, and the non-dispersive troposphere. Both atmospheric layers influence the transit time of the signal by altering the velocity of the signal propagation [Hofmann-Wellenhof et al., 2008].

3.) Receiver errors
Receiver errors include the aforementioned receiver clock error, which denotes the difference of the receiver internal clock to the GPS reference time, as well as internal errors, biases and the receiver noise [Teunissen & Montenbruck, 2017].

4.) Site-dependent errors
Site-dependent errors arise from the antenna environment and will be described in detail in Section 3.2. They are divided into antenna near-field effects, far-field multipath, NLOS reception and signal diffraction. Furthermore, the antenna phase center characteristics in terms of phase center offset and variations can be allocated to this effects, since they can directly be influenced by near-field effects. Theoretically, the site-dependent effects could also be allocated to the group of propagation and receiver errors. Nevertheless, since this dissertation focuses on the analysis and mitigation of these effects, they are grouped together in one extra group.

The observation equations for the code observations ρ and the carrier-phase observations Φ can be formulated as

$$\rho = r + c\,[\delta t_r - \delta t^s] + I_\rho + T_\rho + \epsilon_\rho \tag{3.1}$$

$$\Phi = r + c\,[\delta t_r - \delta t^s] - I_\Phi + T_\Phi + \lambda N + \epsilon_\Phi. \tag{3.2}$$

Herein, r denotes the geometric range between the satellite and the receiver antenna, δt_r and δt^s are the receiver and satellite clock errors, I and T are the ionospheric and tropospheric refraction and λ denotes the respective signal wavelength in meters. N are the unknown integer carrier-phase ambiguities, c is the speed of light and ϵ_ρ and ϵ_Φ include the observation noise and other remaining errors, such as receiver and satellite internal biases. The aforementioned site-dependent effects are also included in ϵ [Misra & Enge, 2001].

The accuracy of the two observation types can be expressed by the so called user equivalent range error (UERE). Depending on the measurement conditions, the UERE of the code observations varies between $1\,m \ldots 10\,m$, and for the phase observations, the UERE is in the millimeter to centimeter range [Teunissen & Montenbruck, 2017]. Hence, in applications with high accuracy requirements, usually the position determination is based on the more accurate carrier-phase observations.

3.1.2 Absolute and relative position determination

The position determination using GPS observations can be separated into absolute and relative positioning techniques. Absolute positioning techniques directly estimate the antenna position in the global coordinate frame, whereas in relative positioning techniques, the baseline vector between the user and a reference antenna is estimated. In this case, the absolute antenna position is determined by adding the baseline vector to the absolute coordinate of the reference antenna. In the following, both positioning techniques are briefly described.

Absolute position determination

Absolute positioning techniques that are only based on code observations (cf. Equation (3.1)) are called ‘code solutions‘ or ‘navigation solutions‘ and are often applied in applications, such as car or pedestrian navigation. Since the ionospheric and tropospheric delays (I_ρ and T_ρ) can be approximated by appropriate models, such as the Klobuchar or the Hopfield model [Teunissen & Montenbruck, 2017], and the satellite positions and the satellite clock error can be determined from the broadcast ephemeries, the remaining unknown parameters are the three antenna coordinates $\mathbf{X_r} = \begin{bmatrix} X_r & Y_r & Z_r \end{bmatrix}^T$ and the unknown receiver clock error δt_r [Misra & Enge, 2001]. Hence, at least four code observations are needed to estimate the position of the antenna. Due to the higher uncertainty of the code observations, the accuracies of these single point positioning (SPP) solutions are in the meter range, but can easily reach tenth of meters due to site-dependent effects [Hofmann-Wellenhof et al., 2008].

In recent years, precise point positioning (PPP) techniques became more popular. Here, undifferenced dual-frequency carrier-phase observations in combination with precise satellite orbit and clock information are utilized for a standalone antenna position determination [Zumberge et al., 1997]. Without the need for simultaneous observations at two stations and with achievable accuracies at the millimeter to centimeter level, PPP offers an alternative to the traditional relative positioning techniques. Nevertheless, this standalone, carrier-phase based approach entails some drawbacks. In contrast to differential approaches, PPP requires a much more careful modeling of systematic errors and a long convergence time is needed. However, since PPP techniques are not addressed in this dissertation, PPP is not further considered and it is referred to the relevant literature (see e.g. [Kouba & Héroux, 2001; Heßelbarth, 2011; Teunissen & Montenbruck, 2017]).

Relative position determination

In contrast to absolute positioning techniques, and as the name suggests, in relative positioning techniques the position of the user antenna, called *rover*, is determined relative to a second antenna, called *master*. By using simultaneous observations of the rover and master antenna, the baseline vector $\mathbf{b} = \begin{bmatrix} b_X & b_Y & b_Z \end{bmatrix}^T$ between the master and rover antenna is estimated. Afterwards, the absolute rover position $\mathbf{X_r}$ can be calculated by

$$\begin{bmatrix} X_r \\ Y_r \\ Z_r \end{bmatrix} = \begin{bmatrix} X_m \\ Y_m \\ Z_m \end{bmatrix} + \mathbf{b}, \tag{3.3}$$

where the subscripts r and m denote the rover and master coordinates, respectively [Misra & Enge, 2001].

The basic idea of this differential approach is to eliminate, or at least minimize, the majority of the aforementioned error sources. Therefore, single and double differences of the master and rover observations are formed. An illustration of the differential approaches is shown in Figure 3.1.

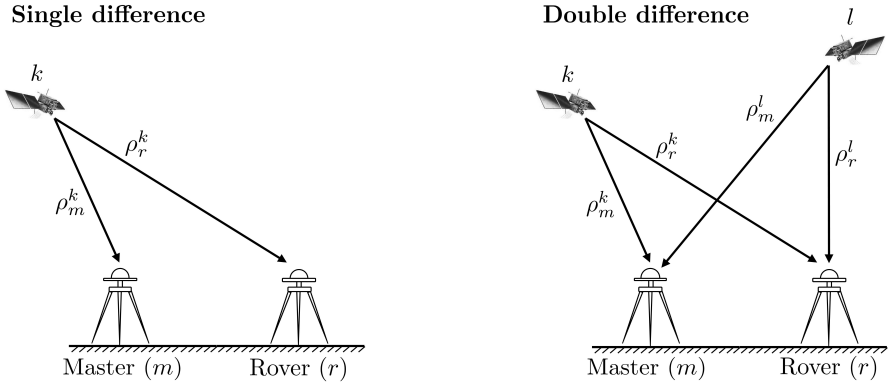


Figure 3.1: Single difference (left) and double difference (right) of pseudorange observations at master (m) and rover (r) antenna.

A single difference denotes the difference between the timely synchronized observations from master and rover to one satellite k. If the distance between the master and rover antenna is short, the satellite signals will pass the same part of the atmosphere and thus, the atmospheric delays I and T cancel out. Furthermore, also the satellite related errors are eliminated [Teunissen & Montenbruck, 2017]. The single difference of the code and phase observations ρ and Φ can be expressed as

$$\rho_{mr}^k = \rho_m^k - \rho_r^k = r_{mr}^k + c\,(\delta t_m - \delta t_r) + \epsilon_{\rho,mr}^k \tag{3.4}$$

$$\Phi_{mr}^k = \Phi_m^k - \Phi_r^k = r_{mr}^k + c\,(\delta t_m - \delta t_r) + \lambda N_{mr}^k + \epsilon_{\Phi,mr}^k. \tag{3.5}$$

Herein, $r^k_{mr} = r_m - r_r$ denotes the difference of the geometric ranges between satellite k at the master (m) and the rover antenna (r), respectively. The difference of two single differences ρ^k_{mr} and ρ^l_{mr}, respectively Φ^k_{mr} and Φ^l_{mr}, that are related to satellites k and l, is called double-difference and can be written as

$$\rho^{kl}_{mr} = \rho^k_{mr} - \rho^l_{mr} \ = r^{kl}_{mr} + \epsilon^{kl}_{\rho,mr} \tag{3.6}$$

$$\Phi^{kl}_{mr} = \Phi^k_{mr} - \Phi^l_{mr} = r^{kl}_{mr} + \lambda N^{kl}_{mr} + \epsilon^{kl}_{\Phi,mr}. \tag{3.7}$$

It is obvious that the receiver clock error $\delta t_{mr} = \delta t_m - \delta t_r$ is identical in the single differences of satellites k and l, and thus, cancels out. As a consequence, the remaining unknown parameters that need to be estimated are the baseline vector $\mathbf{b}$, included in the double-differenced geometric range r^{kl}_{mr}, and the unknown double-difference carrier-phase ambiguities N^{kl}_{mr} [Misra & Enge, 2001]. At this point, it is important to note that site-dependent effects are not eliminated by a differential approach.

The accuracy of the baseline parameters depends on the type of the carrier-phase ambiguity resolution. If the ambiguities are estimated as floating real values, the solution is denoted as float solution and in absence of site-dependent effects, the accuracy is in the range of a few decimeters. If the ambiguities can successfully be fixed to integer values, the solution is called fixed-solution and the accuracy is in the millimeter to centimeter range [Teunissen & Montenbruck, 2017]. Since the absolute position of the rover antenna is determined by adding the baseline vector to the absolute coordinate of the master, it is obvious that the absolute accuracy of the rover position depends on the absolute accuracy of the master coordinate.

3.2 Site-dependent effects

Site-dependent effects can be divided into errors related to the immediate vicinity of the receiving antenna, the so called antenna near-field, and into errors, often summarized as multipath effects. However, due to the different characteristics of multipath effects, it is necessary to distinguish between far-field multipath on the one hand and NLOS reception and signal diffraction on the other hand. Furthermore, in the context of site-dependent effects also the satellite geometry should be taken into account, since it can have an influence on the positional accuracy and a deteriorated satellite geometry, arising from signal obstructions, often entails one or more of the aforementioned effects.

In the following sections, the different site-dependent effects are described in detail and in the same order as they were introduced in Section 1.1 and Chapter 2.

3.2.1 Satellite geometry

The satellite geometry describes the configuration of the satellite positions with respect to the position of the receiving antenna. In most ground-based applications, only signals of satellites with a positive elevation angle can be observed by the antenna. Indicators for the quality of the satellite geometry are Dilution of Precision (DOP) values [Langley, 1999]. DOP values can be determined from the covariance matrix of the parameters $\mathbf{\Sigma_{xx}}$ of a non-linear least-squares SPP solution, given by

$$\mathbf{\Sigma_{xx}} = \sigma^2 \left(\mathbf{A}^T\mathbf{P}\mathbf{A}\right)^{-1}. \tag{3.8}$$

Herein, $\mathbf{A}$ denotes the Jacobian matrix, containing the partial derivatives of Equation (3.1) with respect to the parameters, i.e. the receiver antenna coordinates $\mathbf{X_r} = \begin{bmatrix} X_r & Y_r & Z_r \end{bmatrix}^T$ and the receiver clock error δt_r, and basically represents the relative geometry of the satellites and the antenna. Matrix $\mathbf{P}$ is the weighting matrix of the code observations and σ^2 is the a-priori variance of unit weight [Hofmann-Wellenhof et al., 2008]. Under the assumption of equal weights for all observations, i.e. $\mathbf{P} = \mathbf{I}$ (where $\mathbf{I}$ is the identity matrix), Equation (3.8) simplifies to

$$\mathbf{\Sigma_{xx}} = \sigma^2 \left(\mathbf{A}^T\mathbf{A}\right)^{-1} = \sigma^2\mathbf{D}. \tag{3.9}$$

From the diagonal elements of matrix $\mathbf{D}$ the geometrical DOP (GDOP), PDOP and time DOP (TDOP) can be determined following

$$\begin{aligned} GDOP &= \sqrt{D_{11} + D_{22} + D_{33} + D_{44}} \\ PDOP &= \sqrt{D_{11} + D_{22} + D_{33}} \\ TDOP &= \sqrt{D_{44}}. \end{aligned} \tag{3.10}$$

Furthermore, after transforming $\mathbf{\Sigma_{xx}}$ to a local topocentric coordinate system, the horizontal DOP (HDOP) and vertical DOP (VDOP) can be computed by

$$\begin{aligned} HDOP &= \sqrt{D_{11} + D_{22}} \\ VDOP &= \sqrt{D_{33}}. \end{aligned} \tag{3.11}$$

It becomes obvious that the DOP values can be used to roughly estimate the expectable positional accuracy by scaling the pseudorange error standard deviation σ. Since σ is an unknown quantity it can be estimated by the user equivalent range error (σ_{UERE}, cf. Section 3.1.1) that includes receiver noise, satellite clock and ephemeris errors, unmodeled atmospheric delays and the influences of the site-dependent effects [Langley, 1999]. The UERE is usually in the range of a few meters, whereby the dominating influences are the ionospheric delay and the site-dependent effects [Teunissen & Montenbruck, 2017].

In fact, the DOP values depend on the volume of a polyhedron formed by the tips of the satellite-receiver unit vectors and the larger the volume, the smaller the DOP values [Teunissen & Montenbruck, 2017]. Consequently, the expectable positioning accuracy will be higher if the satellites used for the position estimation are spread out in the sky. Furthermore, if the satellite geometry is deteriorated by obstacles or obstruction sources in the antenna environment, the DOP values will increase and a degraded positional accuracy can be expected.

Later in this thesis it is demonstrated that DOP values are rather insignificant for the positioning accuracy. In fact, the deviations in the distance measurements caused by site-dependent effects represent the dominant influence (cf. Sections 3.2.2 – 3.2.4). Consequently, in case of a comprehensive mitigation of these effects, even higher DOP values can be accepted without a significant loss of accuracy. This applies all the more the higher the number of available satellite signals is.

3.2.2 Far-field multipath

Far-field multipath occurs if the satellite signal that has arrived trough the line-of-sight (LOS) path is superimposed by a reflected signal that reaches the antenna on one or more indirect paths [Hofmann-Wellenhof et al., 2008]. The reflected signals are characterized by an extra geometrical path δ and a relative phase $\Delta\Phi_M$ with respect to the LOS signal [Smyrnaios et al., 2013]. Furthermore, the amplitude of the reflected signal is given by $A_M = \alpha A_D$, where α represents the attenuation factor of the reflection process and the antenna gain pattern and A_D is the amplitude of the direct LOS signal. The superimposition of the direct and reflected signals can be illustrated by means of a vector diagram, where the length of the vectors denotes the amplitude of the respective signal components and the angles between the vectors are related to the respective phase differences. In Figure 3.2, a vector diagram for the superimposition of the direct signal and one reflected signal is shown.

The angle between the direct signal with amplitude A_D and the reflected signal with amplitude A_M (red arrow in Figure 3.2) represents the multipath relative phase $\Delta\Phi_M$. The amplitude of the compound signal A_C is the sum of the two vectors A_D and A_M and the angle between the direct and the compound signal Φ_C can be interpreted as the phase error, resulting from the superimposition [Irsigler, 2008]. Following Smyrnaios et al. [2013], the phase error Φ_C and the amplitude of the compound signal A_C can be determined by

$$\Phi_C = \arctan\left(\frac{\alpha \sin \Delta\Phi_M}{1 + \alpha \cos \Delta\Phi_M}\right) \tag{3.12}$$

$$A_C = A_D \sqrt{1 + 2\alpha \cos \Delta\Phi_M + \alpha^2}. \tag{3.13}$$

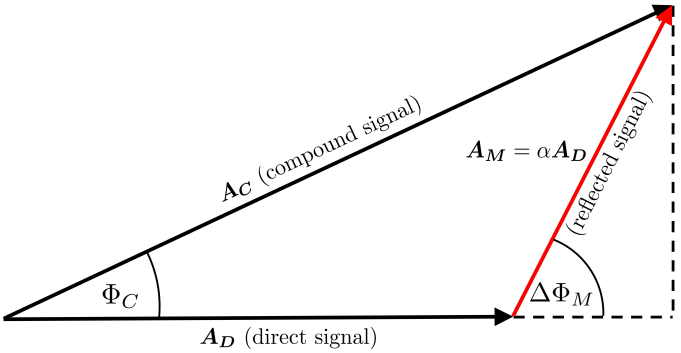


Figure 3.2: Vector diagram for far-field multipath (adopted from Zimmermann et al. [2019]).

From Equation (3.12), the maximal and minimum phase errors can be estimated. Under the assumption that the reflected signal is not attenuated, i.e. $\alpha = 1$, Φ_C reaches its maximum of 90° for $\Delta\Phi_M = 180°$, which corresponds to one quarter of the signal wavelength (≈ 4.8 cm for GPS-L1). On the other hand, for $\Delta\Phi_M = 0°$, the phase error becomes zero.

The extra geometrical path delay δ and the multipath relative phase $\Delta\Phi_M$ highly depend on the geometrical configuration between the satellite, the reflector and the user antenna, and therefore, change over time. In the left panel of Figure 3.3, the geometrical configuration for a horizontal and a vertical reflector is illustrated schematically. The right panel of Figure 3.3 shows the configuration for a horizontal reflector in more detail.

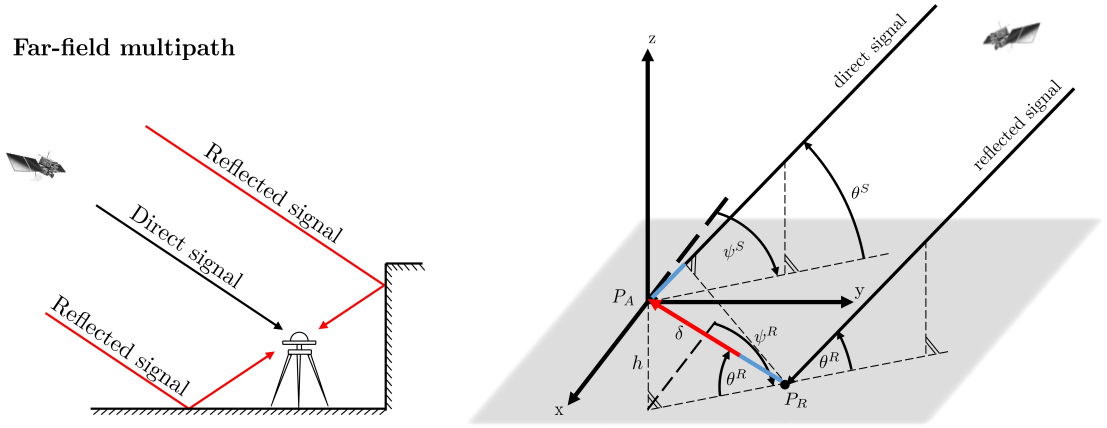


Figure 3.3: Far-field multipath for horizontal and vertical reflector (left). Detailed illustration of far-field multipath for a horizontal reflector (right) (adopted from Zimmermann et al. [2019]).

In the right panel of Figure 3.3, P_A and P_R denote the antenna phase center and the reflection point of the signal, following from the geometrical optics. θ^S and ψ^S denote the elevation and azimuth angle of the satellite signal with respect to P_A, and θ^R and ψ^R with respect to P_R, respectively. The antenna height is given by h and the extra geometrical path delay of the reflected signal (red part of signal path) is denoted by δ.
In the special case of a horizontal reflector, as shown in the right panel of Figure 3.3, the satellite and the points P_R and P_A form a vertical plane, leading to $\psi^R = \psi^S$ and $\theta^R = \theta^S$, respectively. Hence, the geometrical path delay $\delta(t)$ and the multipath relative phase $\Delta\Phi_M(t)$ only depend on the antenna height h and the satellite elevation $\theta^S(t)$ at an instant of time t and can be written as

$$\delta(t) = 2h \sin\theta^S(t) \tag{3.14}$$

$$\Delta\Phi_M(t) = \frac{2\pi}{\lambda} 2h \sin\theta^S(t), \tag{3.15}$$

where λ denotes the respective signal wavelength [Irsigler, 2008]. Due to the motion of the satellite, the multipath relative phase $\Delta\Phi_M\,(t)$ constantly changes. This leads to a periodic behavior of the phase error Φ_C, which can be noticed in the carrier-phase residuals or SNR time-series [Smyrnaios et al., 2013]. Furthermore, the amplitude of the compound signal A_C also varies, since the geometry changes in time.

The signal reflection depicted in Figure 3.3 shows a pointwise and specular reflection. Nevertheless, at this point it should be noted that the assumption of a pointwise reflection process actually does not hold true. Instead, there exist areas on the reflecting surface that contribute to the reflected signal, which are called Fresnel zones. Furthermore, the type of reflection, i.e. diffuse or specular, mainly depends on the satellite elevation angle and the roughness of the reflecting surface inside the Fresnel zones. Hence, in the context of far-field multipath, the location and size of these active scattering regions, as well as the roughness inside these regions needs to be considered. The concept of Fresnel zones and its relation to far-field multipath occurrence, as well as the distinction between specular and diffuse reflection, will be described in detail in Section 3.3.

3.2.3 NLOS reception and signal diffraction

If the direct LOS signal path between the satellite and the antenna is blocked by an obstacle, two phenomena can occur: 1) non-line-of-sight (NLOS) reception and 2) signal diffraction. In Figure 3.4, both phenomena are shown.

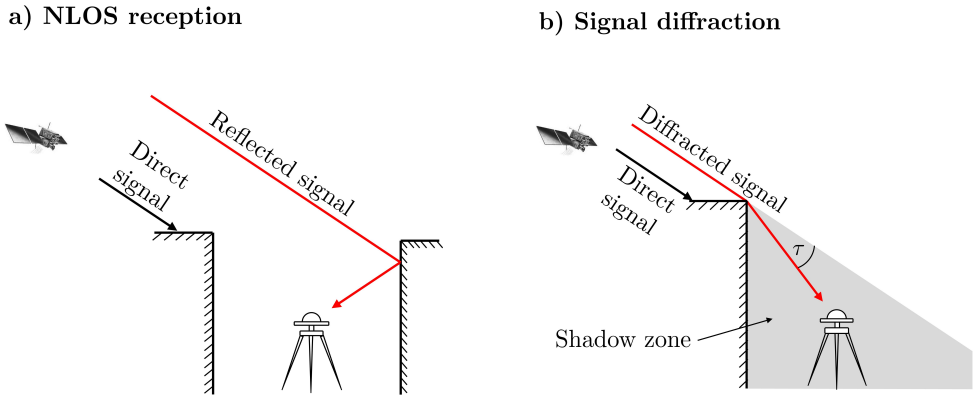


Figure 3.4: NLOS reception (left) and signal diffraction (right).

If the user antenna only receives the reflected signal, one speaks of NLOS reception (see left panel of Figure 3.4). In this case, the ranging error equals the difference between the indirect and the obstructed direct signal path and is typically in the range of several tens of meters [Groves et al., 2013]. Nevertheless, the error directly depends on the distance between the reflecting surface and the antenna. In comparison to far-field multipath, the error of NLOS reception is not limited, since it is completely independent from the direct signal.

Signal diffraction describes the phenomena, where the satellite signal is diffracted at the edge of an obstacle and is bended by the angle τ into the shadow zone that is actually not visible from the satellites point of view (see right panel of Figure 3.4). Diffraction effects can be explained by Huygen's principle, stating that all points on a wavefront can be seen as point sources that create secondary wavelets, forming a new wavefront [Vogel & Gerthsen, 2013]. If this wavefront propagates into the shadow zone, diffraction occurs. Theoretically, the error caused by diffraction is unlimited, only depending on the additional path length [Wieser, 2002]. Nevertheless, in the case of diffraction, the signal-to-noise ratio usually significantly drops and if the direct line-of-sight path to the obstructed satellite is far from the edges of the object, it will drop below the acquisition threshold of the receiver. Hence, the error caused by diffraction is usually in the range of several centimeters up to decimeters, whereby the diffraction angle τ can reach values up to $10° \ldots 20°$ (cf. Figure 5.13 on page 51).

Figure 3.4 represents the direct, reflected or diffracted signal as a straight line. However, in reality this is not applicable and especially in the case of signal diffraction the concept of Fresnel zones should be considered to account for the signal width. This issue will be addressed in Section 3.3.

It should be noted that for the occurrence of NLOS reception, similar to far-field multipath effects, a certain satellite-reflector-antenna constellation needs to exist from a geometrical point of view, to enable the reflected signal to reach the antenna. Hence, it can be assumed that diffraction effects occur more frequently than NLOS reception, at least during static GNSS applications. In Section 5.3, this aspect is further discussed.

3.2.4 Antenna near-field

In the case of far-field multipath (Section 3.2.2), the geometrical optics are used to describe the wave propagation, i.e. a planar wave front and parallel rays are considered. In the immediate vicinity of the antenna this simplified model cannot be used, since it does not account for the complex electromagnetic field characteristics in this region [Dilßner et al., 2008]. Usually, the space surrounding an antenna is subdivided into three regions: 1) the reactive near-field, 2) the radiating near-field, also named Fresnel region and 3) the far-field region, also named Fraunhofer region [Balanis, 2005], where the boundaries of the regions depend on the signal wavelength λ and the maximum antenna dimension D. In Figure 3.5, the respective field regions of an antenna are shown.

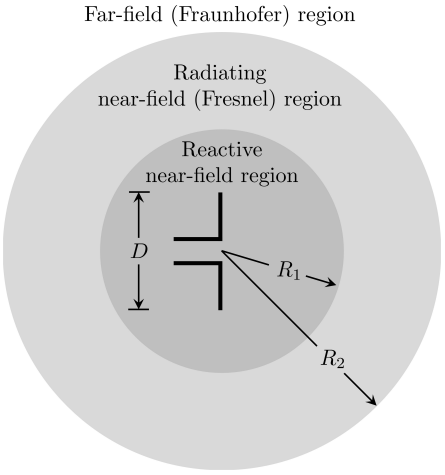


Figure 3.5: Field regions of an antenna (adopted from Balanis [2005]).

The far-field region describes the region, where the radiation pattern is independent from the distance to the antenna and geometrical optics provide an appropriate method to approximate the wave propagation. Thus, the electromagnetic properties of the antenna are not influenced by objects in this region [Dilßner, 2007]. Commonly, the far-field region is taken to exist from a distance of

$$R_2 = \frac{2D^2}{\lambda}. \tag{3.16}$$

The area surrounding the antenna with radial distances smaller than R_2 is called antenna near-field and can be divided into a reactive and radiating part. The immediate vicinity of the antenna is defined as the reactive near-field and is taken to exist at distances smaller than

$$R_1 = 0.62\sqrt{\frac{D^3}{\lambda}}. \tag{3.17}$$

The transition between the far-field and the reactive near-field region is the radiating near-field region. This region is bounded by R_1 and R_2 and here, the radiation pattern depends on the distance from the antenna [Dilßner, 2007].

In Table 3.1, the boundaries R_1 and R_2 are listed for two different antenna types, one Leica AS10 compact antenna and one Leica AR25 choke ring antenna, whereby the respective antenna dimension D is taken from the IGS antenna file *antenna.gra*[1]. Furthermore, the boundaries are determined for the three different GPS signal wavelengths (L1, L2 and L5).

		$\lambda_{L1} = 0.19$m		$\lambda_{L2} = 0.244$m		$\lambda_{L5} = 0.255$m	
		$R_1\,[m]$	$R_2\,[m]$	$R_1\,[m]$	$R_2\,[m]$	$R_1\,[m]$	$R_2\,[m]$
AS10 compact antenna	$D = 0.17$m	0.10	0.30	0.09	0.24	0.09	0.23
AR25 choke ring antenna	$D = 0.38$m	0.33	1.52	0.29	1.18	0.29	1.13

Table 3.1: Boundary values of field regions of two different antenna types (Leica AS10, Leica AR25) and the signal wavelengths of the GPS-L1, GPS-L2 and GPS-L5 frequency.

Objects in the near-field of the antenna can influence the measurements in different ways. On the one hand, they can lead to long-periodic multipath effects that cannot be minimized by averaging over long observation durations. Furthermore, due to the small distance between the reflecting object and the antenna, the reflected signals tend to be stronger than it is the case for signals that are reflected from more distant objects. On the other hand, if conducting objects, such as tribrachs or antenna adapters, are located inside the near-field region, they can change the whole antenna phase center characteristics by imaging and electromagnetic coupling [Wübbena et al., 2006].

Theoretically, coordinates that are estimated from GNSS observations refer to the antenna phase center, represented by one fixed point. In reality, the assumption of this ideal phase center does not hold true, since the location of the phase center depends on the direction of the incoming signal (azimuth α and elevation β) [Zeimetz, 2010]. The deviations from an ideal mean phase center (E) are described by the phase center variations (PCV). Furthermore, the phase center offset (PCO) represents the position of the mean phase center with respect to the antenna reference point (ARP), denoting the mechanical reference point of the antenna. In Figure 3.6, a respective antenna model is shown.

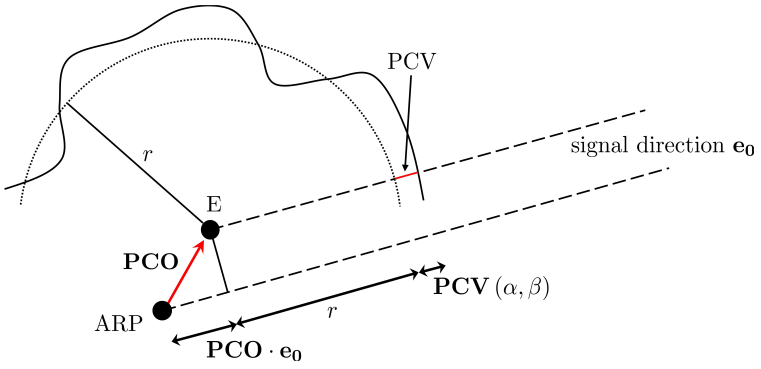


Figure 3.6: Antenna model (adopted from Zeimetz [2010]).

The measured phase r_{ARP} depends on the direction of the incoming signal and can be written as

$$r_{ARP} = r + \mathbf{PCO} \cdot \mathbf{e_0}\,(\alpha, \beta) + PCV\,(\alpha, \beta) + \epsilon, \tag{3.18}$$

where r is the error free value, $\mathbf{e_0}$ is the unit-vector in direction of azimuth α and elevation β and ϵ denotes the observation noise. In recent years, two procedures were proven to be the most effective approaches to calibrate GNSS antennas for the unknown PCO and PCV parameters: the absolute robot calibration and a calibration in an anechoic chamber [Wübbena et al., 2000; Zeimetz & Kuhlmann, 2008].

[1] ftp://igs.org/pub/station/general/antenna.gra

Empirical investigations using both, chamber and robot calibrations demonstrate that objects in the near-field of the antenna can lead to a relative change between the calibration patterns of up to several millimeters, depending on the antenna type and the signal wavelength [Dilßner, 2007; Zeimetz, 2010]. On the one hand, these investigations confirm that antenna calibration parameters are actually only valid for the near-field situation present during the calibration procedure (cf. Section 2.4). On the other hand, the influence of the near-field on the calibration patterns is the reason, why the antenna is often calibrated including the near-field components in high-precision applications [Hirt et al., 2011; Feldmann-Westendorff et al., 2016].

3.3 Fresnel zones

In the geometrical configurations of far-field multipath and NLOS reception, shown in Figure 3.3 and the left panel of Figure 3.4, the assumption of a pointwise reflection is made. Since GNSS satellites are transmitting the signals with an aperture angle of ±13.9°, this does not hold true [Rost, 2011]. Instead of a single reflection point, there are existing areas on the reflector surface that are contributing to the reflected signal. These active scattering regions are called Fresnel zones. The concept of Fresnel zones is illustrated in Figure 3.7 for a horizontal (left panel) and an arbitrarily oriented reflector (right panel).

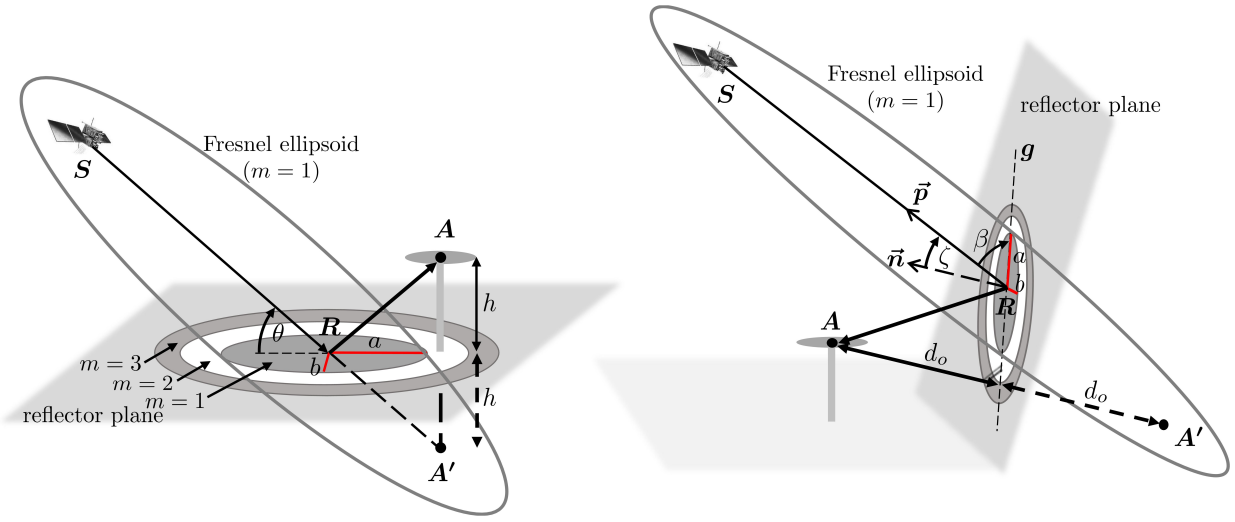


Figure 3.7: Fresnel zones for a horizontal reflector (left) and for an arbitrarily oriented reflector (right) (adopted from Zimmermann et al. [2019]). For reasons of clarity, the three-dimensional Fresnel ellipsoid is only depicted as a two-dimensional ellipse.

Between the satellite S and the mirrored antenna point A', a number (orders m) of ellipsoids of revolution can be formed, with S and A' representing the respective focal points [Rost, 2011]. The Fresnel ellipsoid of first order defines the region where most of the energy is transmitted. The intersection of the Fresnel ellipsoids and the reflector surface results in an ellipse that is called Fresnel zone. In the case of a horizontal reflector, the size and shape depends on the satellite elevation angle θ, the carrier wavelength λ and the vertical distance h between the antenna and the reflector. The semi-minor and semi-major axes of the first Fresnel zone are given by

$$\begin{aligned} b &= \sqrt{\frac{\lambda h}{\sin\theta} + \left(\frac{\lambda}{2\sin\theta}\right)^2} \\ a &= \frac{b}{\sin\theta} \end{aligned} \tag{3.19}$$

and the orientation of the major axis is defined by the direction of the satellite-antenna vector [Larson & Nievinski, 2013].

For a horizontal reflector, the size of the Fresnel zone F increases as the elevation angle decreases, and it reaches its minimum at an elevation angle of 90°. For an antenna height of $h = 1\text{m}$, this leads to $F \approx 0.6\text{m}^2$ and for $h = 5\text{m}$, this leads to $F \approx 3\text{m}^2$. Furthermore, the elevation angle determines the eccentricity of the ellipse (see Equation (3.19)). Thus, the Fresnel zone has a circular shape if the elevation angle is 90°, and it is stretched for decreasing elevation angles.

For vertical reflectors, or, in general, for reflectors with arbitrary orientation in space, as shown in the right panel of Figure 3.7, the parameters of the Fresnel zones, a and b, cannot directly be determined following Equation (3.19). Since the satellite elevation angle θ no longer equals the angle between the signal and the

reflector plane, it has to be substituted. For this purpose, at first, the incidence angle ζ of the satellite signal with respect to the reflector plane is determined by

$$\zeta = \arccos\left(\frac{\tilde{\mathbf{n}} \cdot \tilde{\mathbf{p}}}{\|\tilde{\mathbf{n}}\| \cdot \|\tilde{\mathbf{p}}\|}\right), \tag{3.20}$$

where $\tilde{\mathbf{n}}$ denotes the normal vector of the reflector plane and $\tilde{\mathbf{p}}$ is the vector between the satellite S and the reflection point R. Afterwards, the angle β can be expressed as

$$\beta = 90° - \zeta. \tag{3.21}$$

Moreover, the antenna height h is substituted by the orthogonal distance between the antenna and the reflector plane d_o, leading to

$$\begin{aligned} b &= \sqrt{\frac{\lambda d_o}{\sin\beta} + \left(\frac{\lambda}{2\sin\beta}\right)^2} \\ a &= \frac{b}{\sin\beta}. \end{aligned} \tag{3.22}$$

The orientation of the major axis a of the Fresnel zones is given by the orientation of the line, resulting from the intersection of the reflector plane and a plane defined by S, A and A'. Using Equation (3.22), the Fresnel zones can be determined for every planar reflector, without any limitations regarding the satellite-reflector-antenna configuration.

In the case of arbitrarily oriented reflectors, general statements regarding the size of the Fresnel zones are difficult, since, in this case, the size depends on both, the orientation of the reflector and the satellite azimuth and elevation angles. Table 3.2 illustrates this issue by means of a simulation for (i) a horizontal, (ii) a vertical and (iii) an arbitrarily oriented planar reflector. The three differently oriented reflectors are shown in Figure 3.8, whereby the reflector orientation is represented by the azimuth angle ψ_R and the elevation angle θ_R of the corresponding normal vector $\vec{\boldsymbol{n}}$.
For all three cases, the incidence angles for different satellite positions, given by the respective azimuth ψ and elevation angle θ, with respect to the normal vector $\vec{\boldsymbol{n}}$ are determined following Equation (3.20). Furthermore, for a reflector-antenna distance of $d_o = 5$ m and for $\lambda = 0.19$ m (GPS-L1), the semi-minor and semi-major axis a and b of the 1$^{\text{st}}$ Fresnel zones are computed following Equation (3.22). Finally, the size F of the Fresnel zones is determined by $F = ab\pi$. The results for both, the incidence angle ζ and the size F are listed in Table 3.2.

In the case of the horizontal reflector (cf. top panel of Figure 3.8), the size of the Fresnel zones decreases for increasing satellite elevations, independently from the satellite azimuth angle ψ. Since the incidence angles ζ are determined with respect to the normal vector of the reflector plane, they are complementary to the satellite elevation angle θ by $\zeta = 90° - \theta$.
In the case of the vertical reflector (cf. middle panel of Figure 3.8), the size of the Fresnel zones shows the opposite behavior. Here, F increases as the satellite elevation θ increases. This is reasonable, since here, at least at first glance, the situation is comparable to that of the horizontal reflector – only rotated by 90°. Nevertheless, in contrast to the horizontal reflector, the size of the Fresnel zones varies for different satellite azimuth angles and it becomes obvious that the magnitude of F cannot directly be related to the corresponding azimuth angle ψ. For example, the Fresnel zones are smaller at an azimuth angle of $\psi = 30°$ than at an azimuth angle of $\psi = 0°$. A direct relationship can only be established to the incidence angles of the satellite signals ζ: the larger the angle of incidence, the larger the Fresnel zone.
This is further emphasized using the example of the arbitrarily oriented reflector (cf. bottom panel of Figure 3.8). In this case, an increasing elevation angle θ no longer necessarily leads to an increasing size of the Fresnel zone. However, the relationship between the angle of incidence ζ and F remains unchanged.
It can be concluded that in case of a non-horizontal reflector, statements regarding the size of the Fresnel zones are actually only possible if the orientation of the reflector is known. Furthermore, the comparison of the sizes of the Fresnel zones, listed in Table 3.2, demonstrates that also the absolute values of F highly depend on the reflector orientation.

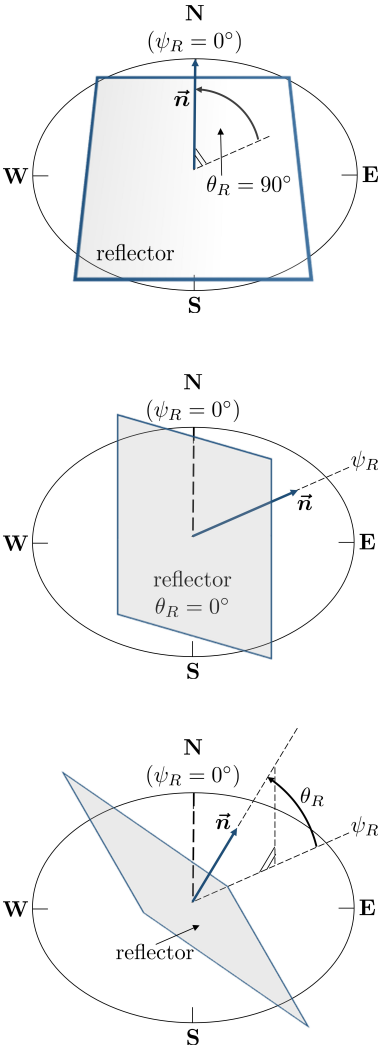


Figure 3.8: (Top) Horizontal planar reflector, i.e. the elevation angle of the normal vector is set to $\theta_R = 90°$. (Middle) Vertical planar reflector, where the azimuth angle of the vector is set to $\psi_R = 19°$. (Bottom) Arbitrarily oriented planar reflector, where the azimuth angle of the normal vector is set to $\psi_R = 19°$ and the elevation angle is set to $\theta_R = 57°$.

$\psi_R = n.d.$		**satellite elevation** θ							
$\theta_R = 90°$		**15°**		**30°**		**60°**		**75°**	
		ζ	$F[m^2]$	ζ	$F[m^2]$	ζ	$F[m^2]$	ζ	$F[m^2]$
satellite azimuth ψ	**0°**	75.0°	46.2	60.0°	12.2	30.0°	4.0	15.0°	3.2
	30°	75.0°	46.2	60.0°	12.2	30.0°	4.0	15.0°	3.2
	45°	75.0°	46.2	60.0°	12.2	30.0°	4.0	15.0°	3.2
	60°	75.0°	46.2	60.0°	12.2	30.0°	4.0	15.0°	3.2
	80°	75.0°	46.2	60.0°	12.2	30.0°	4.0	15.0°	3.2

$\psi_R = 19°$		**satellite elevation** θ							
$\theta_R = 0°$		**15°**		**30°**		**60°**		**75°**	
		ζ	$F[m^2]$	ζ	$F[m^2]$	ζ	$F[m^2]$	ζ	$F[m^2]$
satellite azimuth ψ	**0°**	24.0°	3.6	35.0°	4.5	61.8°	13.6	75.8°	51.8
	30°	18.5°	3.3	31.8°	4.2	60.6°	12.6	75.3°	48.0
	45°	29.8°	4.0	38.9°	5.0	63.3°	15.1	76.6°	57.4
	60°	43.2°	5.7	49.2°	7.1	67.8°	21.5	78.7°	82.5
	80°	62.1°	13.9	65.2°	17.3	78.7°	52.8	82.8°	203.9

$\psi_R = 19°$		**satellite elevation** θ							
$\theta_R = 57°$		**15°**		**30°**		**60°**		**75°**	
		ζ	$F[m^2]$	ζ	$F[m^2]$	ζ	$F[m^2]$	ζ	$F[m^2]$
satellite azimuth ψ	**0°**	44.4°	5.9	30.1°	4.0	10.3°	3.1	19.4°	3.4
	30°	42.8°	5.6	28.1°	3.9	6.5°	3.0	18.5°	3.3
	45°	46.4°	6.4	32.5°	4.2	13.8°	3.2	20.5°	3.4
	60°	52.1°	8.0	39.2°	5.0	21.3°	3.5	23.6°	3.6
	80°	61.8°	13.7	49.6°	7.2	30.9°	4.1	28.6°	3.9

Table 3.2: Incidence angles ζ for different satellite positions and size F of respective 1st Fresnel zones for a horizontal (top), a vertical (middle) and an arbitrarily oriented planar reflector (bottom). The azimuth angle ψ_R and the elevation angle θ_R of the normal vector of each reflector correspond to Figure 3.8. The reflector-antenna distance is set to $d_o = 5$m.

In the context of multipath occurrence it is necessary to distinguish between *diffuse* and *specular* reflection. Basically, the type of reflection depends on the signal wavelength λ, the satellite elevation θ and the roughness ΔH of the reflecting surface inside the first Fresnel zone, where roughness is usually described as the standard deviation of the difference to a mean surface height. With these values, the *Rayleigh criterion*,

$$\Delta H \leq \frac{\lambda}{8 \sin \theta}, \tag{3.23}$$

can be formulated and used to decide whether diffuse or specular reflection will occur [Irsigler, 2008]. If the Rayleigh criterion is not fulfilled, the reflecting surface inside the Fresnel zone will lead to diffuse reflection, i.e., the signal will be scattered in different directions. Hence, this type of reflection has a rather random nature and can be denoted as less critical. Contrarily, if the Rayleigh criterion is fulfilled, i.e. the surface inside the Fresnel zone is rather smooth compared to the signal wavelength, mostly specular reflection will occur, leading to the phenomena described in Section 3.2.2. In Table 3.3, the Rayleigh criterion, determined from Equation (3.23), is exemplarily compared to the surface roughness of four different reflecting surfaces, whereby the surfaces are separated into horizontal and vertical reflectors and the surface roughness is determined from TLS point clouds of representative locations.

horizontal reflector										
satellite elevation θ	5°	10°	20°	30°	40°	50°	60°	70°	80°	90°
Rayleigh-$\Delta H[cm]$	27.3	13.7	7.0	4.8	3.7	3.1	2.8	2.5	2.4	2.4
asphalt road	$\Delta H \approx 0.2cm - 0.5cm$									
field/meadow	$\Delta H \approx 10cm - 20cm$									
vertical reflector										
satellite elevation θ	0°	10°	20°	30°	40°	50°	60°	70°	80°	85°
Rayleigh-$\Delta H[cm]$	2.4	2.4	2.5	2.8	3.1	3.7	4.8	7.0	13.7	27.3
concrete wall	$\Delta H \approx 0.1cm - 0.3cm$									
stone wall	$\Delta H \approx 3cm - 5cm$									

Table 3.3: Comparison of Rayleigh criterion and surface roughness for different reflecting surfaces. For the vertical reflectors it is assumed that the azimuth of the satellite signal is orthogonal to the reflecting surface.

Table 3.3 demonstrates that for smooth surfaces, such as an asphalt road, mostly specular reflections can be expected for all satellite elevations. In contrast, if GNSS measurements are performed on a field, this is only the case for lower elevation angles. Under the assumption that the azimuthal direction of the satellite signal is orthogonal to a vertical reflector, i.e. the incidence angle only depends on the satellite elevation angle θ, the opposite behavior can be expected. If the roughness of the vertical reflector is large compared to the respective signal wavelength, only for satellite signals with higher elevation angles, mostly specular reflections will occur.
In general, it can be stated that in case of rough surfaces, specular reflections, and thus, strong far-field multipath effects, can mostly be expected at large incidence angles of the satellite signals (related to the normal vector of the reflector).

In addition to determining Fresnel zones on the reflecting surface, the concept can also be considered for the line-of-sight (LOS) transmission in order to characterize the type of signal propagation [Hannah, 2001]. In Figure 3.9, the Fresnel ellipsoid of the first order is shown for the LOS transmission between the satellite S and the antenna A.

The radius R_F of the Fresnel zone at any point D along the signal path can be determined by

$$R_F = \sqrt{\frac{\lambda d_S d_A}{d}}, \tag{3.24}$$

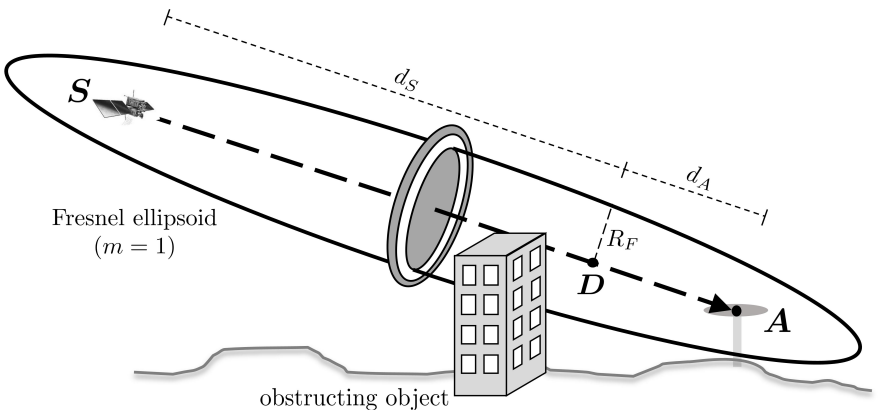


Figure 3.9: Fresnel ellipsoid of the first order for line-of-sight transmission between the satellite S and the antenna A including a building obstructing the signal path and parts of the first Fresnel zone (adopted from Zimmermann et al. [2019]).

where λ is the carrier wavelength, d_S denotes the distance between D and S, d_A denotes the distance between D and A, and $d = d_S + d_A$ is the total length of the signal path [Rost, 2011]. An obstructing object in the signal path with larger dimensions than the Fresnel zone at that point will lead to a complete blocking of the signal. If the obstructing object in the signal path is smaller than the Fresnel zone, the signal can be diffracted at the edges of the object. Without any obstruction source, the signal transmission will be undisturbed.
In order to get an impression of the dimensions of the Fresnel zones along the signal path, R_F is shown in Figure 3.10 for $d_A = 1 \ldots 1000$ m and $\lambda = 0.19$ m (GPS-L1). The total length of the signal path is set to $d = 20000$ km.

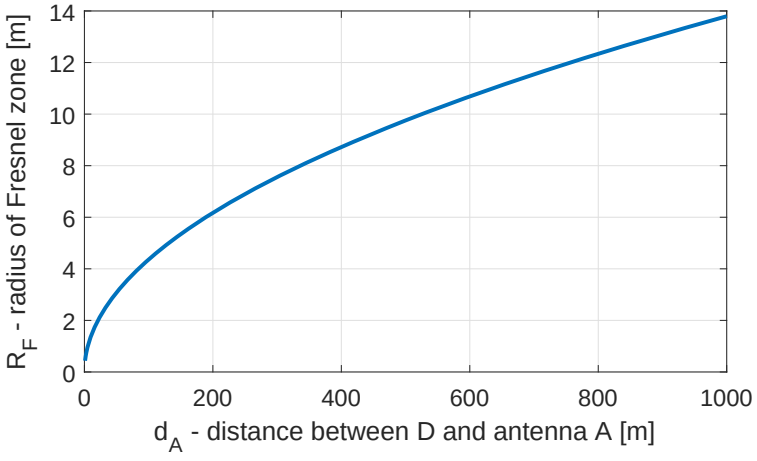


Figure 3.10: Radius of Fresnel zone for LOS transmission (adopted from Zimmermann et al. [2019]).

It becomes obvious that, especially for satellites at lower elevation angles, small objects in the environment can lead to diffraction effects[2]. Thus, Figure 3.10 emphasizes that the choice of a proper elevation mask is an important step during data processing.

[2]Although the average satellite-receiver distance for satellites with lower elevations can be approximated by $d = 25000$ km, the difference of 5000 km only leads to variations in R_F at the sub-millimeter level for the distances shown in Figure 3.10 and up to 7 cm at $d_A = 100$ km . Thus, the values of R_F can be generalized for all satellite elevation angles.

4. Content of relevant publications

In this chapter, the publications that form the basis of this cumulative dissertation are briefly summarized. According to the chronological progress, they are referred to as Publications A-E in the text. In Figure 4.1, they are related to the site-dependent GNSS effects that are addressed in the respective publication.

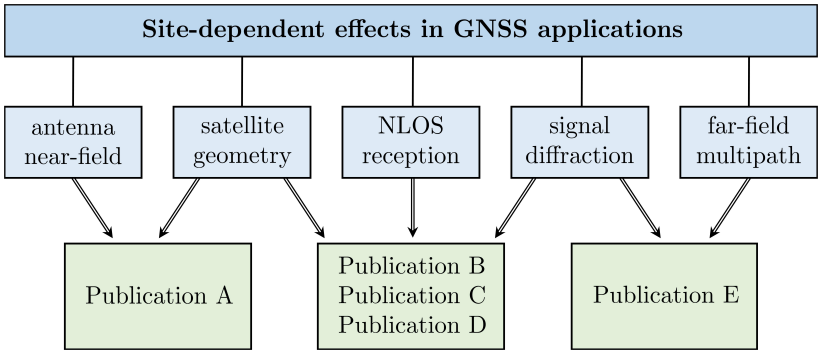


Figure 4.1: Content assignment of the relevant publications to clarify their respective contribution to the dissertation.

Besides the analysis of antenna near-field effects, Publication A contains investigations on the influence of satellite obstructions on GNSS measurements and forms the basis of the concept of obstruction adaptive elevation masks (OAEM), developed in Publication B. Publication C transfers the concept of obstruction adaptive elevation masks to kinematic applications and presents a simulation based analysis of geometry maps to improve the waypoint flight planning of UAV flights. Publication D enhances the concept of obstruction adaptive elevation masks for the georeferencing of TLS point clouds. Publication E adapts the concept of Fresnel zones for the identification and mitigation of signal diffraction and contains an analysis of theoretical assumptions regarding far-field multipath effects.

In the following sections, the publications are briefly summarized. The main aspects of the publications are then again addressed and highlighted in Chapter 5. In particular, the classification into the overall context of this dissertation is then carried out, taking into account the objectives, formulated in Section 1.2.

Publication A (peer-review)

- Zimmermann, F., Eling, C., & Kuhlmann, H. (2016). Investigations on the Influence of Antenna Near-field Effects and Satellite Obstruction on the Uncertainty of GNSS-based Distance Measurements. *Journal of Applied Geodesy*, 10(1), 53–60

In this publication, two of the aforementioned site-dependent effects are empirically analyzed. On the one hand, antenna near-field effects are investigated. Particularly, the ability of increasing the distance between the antenna mount and the antenna itself to minimize the influence of the effect is analyzed. On the other hand, satellite obstructions are simulated for data sets recorded under optimal GNSS measurement conditions and their influence on the positional accuracy is investigated.

For both parts, the data of an elaborate measurement campaign at an EDM calibration test site was used, where ideal GNSS measurement conditions can be found and nominal values with superior accuracy are available.

Investigations on antenna near-field effects

For this empirical investigation, different combinations of geodetic GNSS antennas and antenna spacers were tested. The antenna spacers are poles made out of two different materials and with three different

and accurately known lengths between 20 and 60 centimeters, intended to increase the distance between the top of the pillar and the GNSS antenna. A total number of 162 baselines were observed for at least 4 hours observation duration with the different antenna-spacer combinations. Afterwards, the differences to the nominal values were determined and analyzed. From the results, three conclusions can be drawn:

1.) Antenna spacers with a length of 60 cm are not suited for high-precision GNSS measurements, since the uncertainty of the leveling and centering of the antenna over the reference point of the pillar becomes too high.

2.) An equal combination of antenna and spacer type at two pillars enables the minimization of antenna near-field effects during the double-differencing process, and thus, an equal setup is more important than increasing the distance between the GNSS antenna and the top of the pillar. With this kind of setup, accuracies at the sub-millimeter level can be achieved.

3.) Even in case of an identical antenna setup, individual antenna calibrations cannot be neglected, since the direction dependent variations of the phase center cannot be reduced by forming double-differences.

Investigations on satellite obstructions

Four generic obstruction scenarios are simulated for the data sets with equal antenna setups, by defining obstructed areas between certain azimuth and elevation angles. Due to the excellent GNSS conditions at the EDM calibration site and the minimization of antenna near-field effects by the equal antenna setup, the influence of a deteriorated satellite geometry on the positional accuracy can be analyzed isolated from other site-dependent GNSS effects. Thereby, the DOP values are used as a quality measure for the satellite geometry.

It is found that the deterioration of the satellite geometry does not lead to a significant lower positional accuracy, because the high signal quality is not affected by the simulation procedure. This leads to the conclusion that the influence of the constellation quality is marginable compared to other systematic effects, such as far-field multipath or signal diffraction, that are usually accompanied with satellite obstructions.

In Chapter 5, the investigations on both, the antenna near-field effects (Section 5.1) and the influence of satellite obstructions (Section 5.2.1) are presented and discussed in more detail.

Publication B (peer-review)

- Zimmermann, F., Eling, C., & Kuhlmann, H. (2017a). Empirical assessment of obstruction adaptive elevation masks to mitigate site-dependent effects. *GPS Solutions*, 21(4), 1695–1706

In this publication, an algorithm for the detection and exclusion of NLOS reception and signal diffraction is developed. The algorithm is based on site specific and obstruction adaptive elevation masks (OAEM), determined from accurately georeferenced TLS point clouds. In contrast to elevation masks that reject satellite signals below a fixed elevation angle, the OAEM is able to identify and exclude NLOS reception and signal diffraction at all possible elevation angles.

Under the assumption that an initial position of the GNSS antenna is known with an accuracy of a few decimeters, the azimuth and elevation angles of the line-of-sight vectors between the antenna position and every point of the point cloud are determined. Afterwards, the elevation angles are allocated to an azimuthal grid with a predefined cell width and in every cell, the highest elevation angle is identified. To avoid that the uncertainty of the initial antenna position leads to elevation angles that are too low compared to the true, but unknown values, a cellwise adjustment is performed. Therefore, for every cell, the uncertainty of the identified elevation angle is determined following the law of error propagation and added to the respective elevation angle. Now, the OAEM is realized as a series of elevation angles for the predefined azimuthal grid.

Any satellite signal with an elevation angle lower than the OAEM value in the respective azimuthal direction is either subject to NLOS reception or signal diffraction and is excluded from the coordinate estimation process. The idea of simply excluding the signal rests on the findings of Publication A [Zimmermann et al., 2016], stating that the negative impact of the signal exclusion on the quality of the satellite geometry is negligible, if the remaining satellite signals are not affected by other systematic effects.

The algorithm is assessed by comparing the positioning solutions at two stations to reference coordinates, determined from terrestrial measurements. It is found that both, the positional accuracy and the percentage of epochs where the carrier-phase ambiguities could successfully be fixed to integer values is improved after the OAEM is applied to the raw data sets. While for the raw data sets only in 56%, respectively 74% of the observation epochs ambiguity-fixed solutions are available, the detection and exclusion of NLOS effects increases the percentage to 100% at both stations. Furthermore, the coordinate differences to the reference solution only vary between -1.8 mm and 0.6 mm at station A and -1.5 mm and 0.4 mm at station B, respectively. Compared to the results from the raw data sets (station A: -12.6 mm to 5.7 mm, station B: -16.8 mm to 6.9 mm) this represents a significant improvement, whereby especially the accuracy of the height component profits from the OAEM approach. The results are discussed in detail in Section 5.3.

Publication C (peer-review)

- Zimmermann, F., Eling, C., Klingbeil, L., & Kuhlmann, H. (2017b). Precise Positioning of UAVs– Dealing with challenging RTK-GPS measurement conditions during automated UAV flights. *ISPRS Annals of Photogrammetry, Remote Sensing & Spatial Information Sciences*, IV-2/W3, 95–102

In this publication, site-dependent effects are addressed in the context of unmanned aerial vehicles (UAV) as an example of kinematic GNSS applications. In order to improve the efficiency of using UAVs in mobile mapping applications, such as surveying, mining or archaeology, an automation of the flight and the processing of the collected data is currently aimed at. The ability of automating the mapping process depends on an accurate and direct georeferencing. Since the direct position estimation of UAVs is usually based on an onboard multi-sensor systems, consisting of RTK-GPS capable receivers and additional sensors like IMUs, the absolute positioning accuracy highly depends on the local GPS measurement conditions. In this context, two strategies to minimize the influence of site-dependent effects are analyzed: 1) a GPS constellation based flight planning on the basis of geometry maps and 2) the application of obstruction adaptive elevation masks to mitigate NLOS reception and signal diffraction during the position estimation process.

GPS constellation based flight planning

In contrast to a remotely controlled flight, the UAV has to consider its 3D environment during an autonomous flight, to be able to safely navigate close to the object of interest. One criteria to assess possible waypoints is the quality of the measurement conditions in terms of DOP values. Since DOP values determined from forecasted satellite positions do not consider the actual visibility of the satellites, a 3D model of the UAV environment, which is either a-priori known or determined from the onboard mapping sensors, is used to identify the visible satellites and to assess the quality of the satellite constellation from a geometrical point of view. Therefore, the LOS vectors from each waypoint to all satellites are determined. Afterwards, a vector-plane intersection is performed for all LOS vectors and planes of the 3D model. By testing whether the intersection points are inside the restricting polygon of each plane and if the intersection points are between the waypoint and the satellite, actually masked satellites are identified and excluded from the DOP value determination. This results in a geometry map, representing the quality of the satellite geometry at the waypoints along the planned flight path. The algorithm is evaluated using a real UAV trajectory and a 3D model that includes a building and vegetation. The results demonstrate that for certain parts of the UAV trajectory the DOP values clearly exceed values of 5 and that the geometry maps enable to identify these regions, while providing alternative waypoint candidates for the optimization of the UAV flight path under avoidance of unfavorable GNSS conditions.

OAEMs in kinematic GNSS applications

In order to mitigate the influence of NLOS reception and signal diffraction and to ensure a precise position estimation, the concept of obstruction adaptive elevation masks is transferred from static applications, as presented in Publication B [Zimmermann et al., 2017a], to this kind of kinematic applications. Due to the motion of the antenna, the obstruction adaptive elevation mask needs to be determined in every observation epoch to account for the constantly changing antenna environment. Based on the initial RTK solution and a georeferenced point cloud of the antenna environment, the algorithm developed in Publication B [Zimmermann et al., 2017a] is applied to determine the epochwise OAEMs. A dedicated field test is carried out to assess the performance of OAEMs in kinematic applications, whereby, instead of the data from a real UAV flight, raw observations were collected with a GPS antenna mounted on a prism pole. This allows for controlled terrestrial reference measurements. It is found that even under harsh GPS measurement conditions, the coordinate differences only vary between ±2cm, which corresponds to the increased percentage of epochs with fixed carrier-phase ambiguities.

The results of both parts are further discussed in Chapter 5, whereby the details on the GPS constellation based flight planning can be found in Section 5.2.2 and the usage of OAEMs in kinematic GNSS applications is assessed in Section 5.3.3.

Publication D (peer-review)

- Zimmermann, F., Holst, C., Klingbeil, L., & Kuhlmann, H. (2018). Accurate georeferencing of TLS point clouds with short GNSS observation durations even under challenging measurement conditions. *Journal of Applied Geodesy*, 12(4), 289–301

The results from publications B and C [Zimmermann et al., 2017a,b] demonstrate that the concept of obstruction adaptive elevation masks can efficiently be used to identify and exclude satellite signals that are subject to NLOS reception and signal diffraction, and that both, static and kinematic GPS applications can profit from this approach. However, the major drawback of this approach is the need for an accurately georeferenced model of the environment and an a-priori known initial antenna position with an accuracy in the range of a few decimeters. In Publication B [Zimmermann et al., 2017a], the initial antenna position is determined in a batch least-squares baseline solution using several hours of observation data. Hence, the initial positioning solution fulfills the accuracy requirements. In Publication C [Zimmermann et al., 2017b], the OAEM concept is transferred to a kinematic application. In the respective field test, the initial positioning solution was determined via RTK and after assessing the accuracy by terrestrial measurements it was found that both, the fixed and float solutions fulfill the aforementioned accuracy requirements. In both publications it is assumed that the antenna environment is represented by an a priori given, accurately georeferenced TLS point cloud. Nevertheless, especially in case of short observation durations, NLOS reception and signal diffraction effects can lead to positioning errors in the decimeters range. Since the transformation of the point cloud from the local scanner coordinate system to the global coordinate system is usually based on GPS measurements, the positional uncertainty directly affects the accuracy of the georeferencing, leading to erroneous OAEM values. To overcome this dilemma, an approach is presented that iteratively performs the georeferencing of the point cloud and the OAEM determination in two consecutive steps. Using the example of a dense point cloud and GPS observations, which were measured in an urban scenario, it is demonstrated that the approach can solve the aforementioned problem.
It turns out that, although the GPS measurements at the ground control points were partially performed under extremely challenging conditions, the algorithm allows for a reduction of the observation duration to five minutes, while still achieving a positional accuracy in the centimeter range. The key to the accurate positioning results are the initial states of the ground control point coordinates that are estimated during a single point positioning, enhanced by an RAIM-FDE (Receiver-Autonomous-Integrity-Monitoring - Fault-Detection and Exclusion) approach. The algorithm and the results are discussed in detail in Section 5.3.4.

Publication E (peer-review)

- Zimmermann, F., Schmitz, B., Klingbeil, L., & Kuhlmann, H. (2019). GPS Multipath Analysis using Fresnel Zones. *Sensors*, 19(1), 25

In this publication, the concept of Fresnel zones is considered in the context of analyzing and mitigating site-dependent effects. First, the performance of the obstruction adaptive elevation masks is further improved by determining Fresnel zones for the line-of-sight transmission between the user antenna and the satellite. This takes into account that most of the signal energy is not transmitted on a straight line, but inside an ellipsoid of revolution. As a consequence, at every point on the signal path, the satellite signal has a certain width that equals the diameter of the ellipsoid. If an object in the antenna environment intersects this region, diffraction effects can occur, even if the line-of-sight vector to the satellite is not obstructed by the object.

If all signals that are subject to NLOS reception or signal diffraction are successfully identified and excluded by applying obstruction adaptive elevation masks, far-field multipath is the accuracy limiting site-dependent effect, influencing the remaining satellite signals. The identification of satellite signals that are potentially influenced by far-field multipath requires the determination of the regions on the reflecting surface that are contributing to the reflection process. These regions are called Fresnel zones and can be determined by intersecting the respective Fresnel ellipsoid with the reflector surface. The theory on far-field multipath defines a complete overlap of the first Fresnel zone and the reflector as one prerequisite for multipath occurrence. Following this theoretical assumption, a reflection point of a signal, determined from the geometrical optics, that is located on the reflector surface would not be a sufficient criteria to decide whether the signal is influenced by far-field multipath.
Hence, in order to analyze the relation between far-field multipath occurrence and the location and size of the Fresnel zone, a dedicated field test on a building roof is performed. Since the roof is spatially limited and horizontal, it represents an ideal, controlled environment to analyze this issue for one dominant reflector. The analysis is performed by comparing simulated and real observed signal-to-noise ratio time series and relating the results to the percentage of overlap between Fresnel zone and reflector. It is found that an overlap of 50% is sufficient to induce far-field multipath effects.

A detailed analysis of the results is given in Chapter 5, whereby the integration of the Fresnel zones into the OAEM concept for diffraction mitigation is discussed in Sections 5.3.1 and 5.3.2 and the relationship between Fresnel zones and far-field multipath occurrence is analyzed in Section 5.4.

5. Summary of most important results

In the previous chapter, the relevant publications on which this cumulative dissertation is based on were briefly summarized. In the overall view, the major findings and aspects can be further emphasized. Taking into account the preliminary considerations described in Chapter 1, the following sections distinguish between investigations on antenna near-field effects (Section 5.1) and on the satellite geometry (Section 5.2), the mitigation of NLOS reception and signal diffraction (Section 5.3) and the analysis of far-field multipath (Section 5.4). Each of these aspects contributes to the overarching goal of gaining a deeper understanding of the different site-dependent effects and enlarging the number of available analysis and mitigation techniques.

5.1 Minimization of antenna near-field effects by appropriate measurement strategies

Objects in the immediate vicinity of the antenna can change the antenna phase center characteristics of the receiving antenna and can introduce an uncalibrated bias in the coordinate solution (cf. Section 3.2.4). Since the receiving sensor itself is affected by near-field effects, a satellite selection strategy, as suggested in Chapter 1, cannot be realized. Thus, the investigations on near-field effects are driven by the basic idea of testing special antenna setups for their ability of minimizing the effect. In particular, this implies increasing the distance between the antenna mount and the antenna itself by using antenna spacers in combination with different geodetic high-grade antennas. Consequently, the following three questions arise:

- What is an appropriate field experiment design to empirically investigate the influence of antenna near-field effects on the GNSS baseline accuracy?
- Is it possible to reduce the influence of near-field effects by increasing the distance between the antenna monumentation and the antenna itself?
- Does this kind of antenna setup have any limitations regarding handling and practicability?

Within the framework of this dissertation, studies were carried out to answer these questions. They are documented in Publication A [Zimmermann et al., 2016]. The following sections summarize the main findings of these investigations.

5.1.1 Design of field experiments

An empirical investigation of near-field effects poses several challenges for the field tests to be carried out:

1) For an isolated analysis of the near-field influence, the separability from other systematic error sources must be ensured. Ideally, the entirety of the remaining error sources, described in Chapter 3, can completely be eliminated.
2) An evaluation of the influence on the positioning accuracy requires the availability of nominal values with superior accuracy.
3) The antenna spacers must be precisely manufactured, particularly an exact straightness and an accurately known length must be guaranteed.
4) A high-precision leveling and centering of the antenna above the reference point of the pillar must be performed to avoid deviations arising from a possible tilting of the antenna-spacer combination.

In order to account for requirements 1) and 2), a measurement campaign was performed on the EDM calibration test site of the University of Armed Forces in Munich, Germany. The calibration site consists of eight horizontally and vertically aligned concrete pillars, distributed on a total length of 1100m. For both, the distance and height differences between the pillars, nominal values with superior accuracy are available that were determined during an intercomparison program in 2012 [Heister, 2012; Heunecke, 2015]. Moreover,

the pillars were build on an earth-mound and since there are no obstruction sources in the surrounding of the pillars, GNSS measurements can be performed under optimal GNSS measurement conditions. In particular, this includes a nearly multipath-free environment 3 to 4 meters above the surrounding surface level and a nearly free horizon. Hence, NLOS reception and signal diffraction can be excluded and a constantly good satellite geometry is available. Since highest accuracies are targeted, the relative positioning approach, described in Section 3.1.2, is applied. Thanks to the short baselines of maximal 1100 meters, this leads to an elimination of the atmospheric and satellite related errors (see Section 3.1.1) by forming double-differences of the carrier-phase observations. Therefore, far-field multipath and antenna related effects, i.e. near-field effects and phase center corrections, are the remaining influences. In order to minimize far-field multipath, the minimum observation duration of an observation session is set to 4 hours to ensure an effective minimization by averaging. Furthermore, high-grade geodetic antennas are used (Trimble Zephyr Geodetic, Trimble Zephyr 2 and Leica AT504GG Choke Ring) that are designed to reduce the influence of far-field multipath. Finally, all antennas were calibrated for their phase center offsets and variations in an anechoic chamber beforehand. Consequently, due to the chosen location, as well as the measurement and processing strategy, an isolated analysis of the antenna near field influences becomes possible.

The antenna spacers are made out of two different materials (aluminum and carbon fiber) and with three different lengths (20cm, 40cm, 60cm) and were manufactured in the in-house precision mechanics lab. The exact straightness of the spacers was carefully verified on a lathe machine and the lengths of the spacers were controlled with a caliper, showing a very low variation in the range of 0.01 to 0.02 millimeters.

Leveling and centering of the antenna spacer is the most crucial step during the whole measurement process, since a possible tilting of the antenna spacers directly influences the baseline accuracy. Previous investigations on antenna near-field effects (cf. Section 2.4) document magnitudes of the influence in the sub-millimeter to millimeter range. Hence, the remaining uncertainties from the leveling and centering should not exceed a few tenth of a millimeter. A precise tubular level with a sensitivity of 0.1mm/1m is sufficient to limit the uncertainty to 0.06mm in the case of the 60cm spacer. However, initial tests have shown that the use of a precise tubular level is not practicable, as this is associated with the adaptation of an additional carrier plate at the tip of the spacer, which must be unscrewed again before the antenna is attached. Hence, the antenna is directly adapted on the spacer and after a course leveling with the level of the tribrach and the alignment of the antenna to the northern direction, two orthogonally arranged tacheometers are used to precisely control and adjust the leveling of the antenna before and after every observation session. The angular precision of the tacheometers is 0.3mgon, which equals 0.02mm at a distance of 5 meters. Since the tacheometers are placed close by to the concrete pillars, the uncertainty of this leveling strategy does not exceed this value. Hence, even though this procedure is extremely time-consuming, it meets the high accuracy requirements regarding the antenna leveling.

5.1.2 Analysis of results

During the five-day measurement campaign, in total 162 baselines were observed with different combinations of antenna spacers and antenna types. Then, a baseline solution was carried out, the 3D-vectors were separated into their distance and height component and compared to the known nominal values of the EDM calibration baseline site. First, the distance differences of all observed baselines, shown in Figure 5.1, are used to answer the question, whether the antenna setup in general has any limitations.

It becomes obvious that the largest differences appear when at least at one pillar an antenna spacer with a length of 60cm is used. This indicates that despite the huge effort, the process of centering and leveling of the antenna spacers (cf. Section 5.1.1) gets critical from a certain spacer height. In addition, as the length of the spacer increases, the lever arm also increases and the entire antenna setup becomes more unstable and, for example, much more susceptible to wind. Based on these results, it can therefore be concluded that spacers with a length of 60cm are not suited for high-precision GNSS measurements and as a consequence, all baselines, where 60cm spacers were used, are not considered in the further analysis.

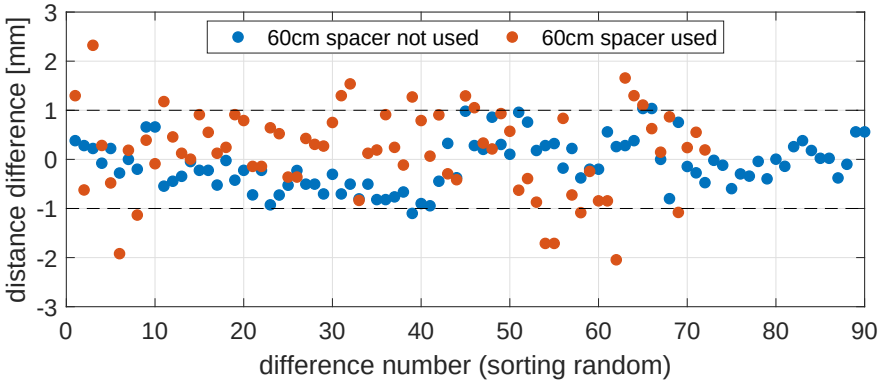


Figure 5.1: Distance differences of all observed baselines. The red dots denote baselines were at least one 60cm spacer was used and the blue dots denote baselines were 60cm spacers were not used.

In order to answer the main question whether near-field influences can be reduced by increasing the distance between the antenna and the monumentation, the remaining differences are split into two data sets, *equal* and *mixed*. The data set *equal* contains all differences of baselines with an equal combination of antenna type and spacer, e.g. 20cm spacer and Trimble Zephyr Geodetic antenna, used at both pillars. Accordingly, the data set *mixed* contains all mixed spacer and antenna combinations.
In Figure 5.2, the 2D-distance and height differences for data set *equal* are shown, sorted by the respective baseline lengths. For a better visualization, they are color coded. In addition, the antenna types used for each baseline are denoted by Z1 (Trimble Zephyr Geodetic), Z2 (Trimble Zephyr 2) and L (Leica AT504GG Choke Ring).

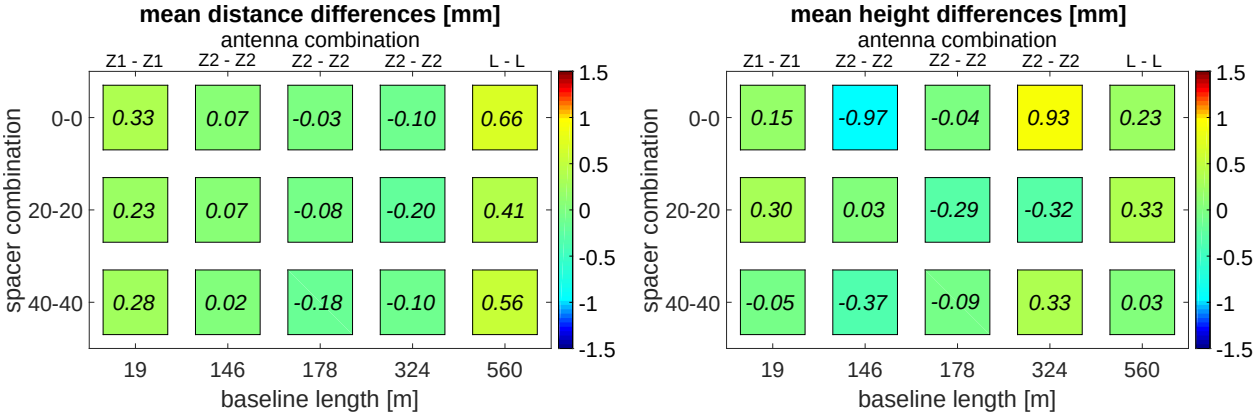


Figure 5.2: Mean distance (left) and height differences (right) in millimeters of equal spacer and antenna combinations, sorted by the respective baseline length. The left vertical axis denotes the spacer length at the two pillars. The respective antenna types are denoted by Z1 (Trimble Zephyr Geodetic), Z2 (Trimble Zephyr 2) and L (Leica AT504GG Choke Ring).

Figure 5.2 shows that all differences to the reference solution are less than one millimeter in both components. No systematic effect is visible, neither related to the different spacer lengths, nor related to the different antenna types used at the pillars. This indicates that independent from the spacer length, a very high accuracy level is achieved when identical antenna setups are used. If it were possible to reduce the near field influence by using longer spacers, a gradual improvement in accuracy from the spacer combination 0-0 to 40-40 should have been visible in Figure 5.2. Nevertheless, the following comparison of the results from data set *equal* to data set *mixed* shows the possibility of an alternative mitigation approach.

In Table 5.1, the mean values of the differences and the respective standard deviation for both data sets are compared. Additionally, in Figure 5.3, the differences of the distance and height component are shown.

Distance component	mean [mm]	σ [mm]
Equal	0.14	0.31
Mixed	-0.21	0.53
Height component	**mean [mm]**	**σ [mm]**
Equal	0.02	0.46
Mixed	-0.65	0.87

Table 5.1: Mean difference values and standard deviations for equal and mixed antenna-spacer combinations.

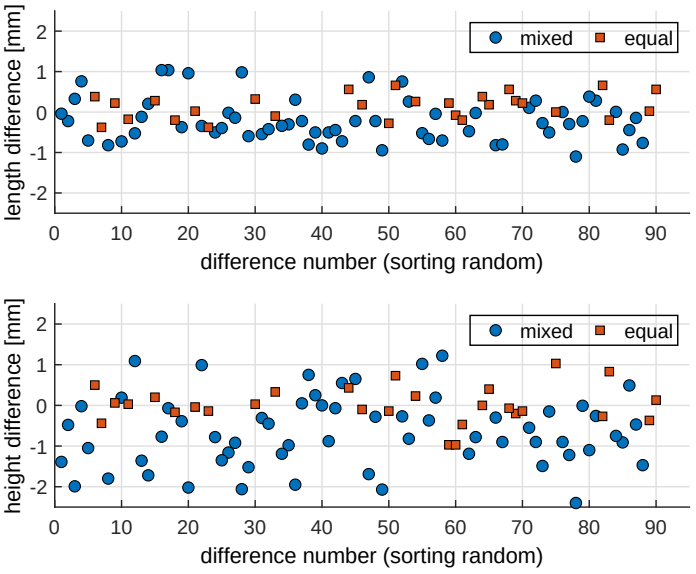


Figure 5.3: Distance differences (top) and height differences (bottom) for equal (red squares) and mixed (blue dots) spacer-antenna combinations.

In comparison to the results for equal antenna setups, the mean value of the distance differences of the data set *mixed* is shifted by 0.35mm and the standard deviation is increased by a value of 0.22mm. The same trend applies for the height component of the baselines. Here, the mean value is shifted by 0.63mm and the standard deviation is increased by a factor of nearly 2. Especially from Figure 5.3 it becomes obvious that the height component is more affected by a mixed antenna setup than the distance component.
The data sets *equal* and *mixed* only differ at their baseline lengths and their kind of spacer and antenna combinations. In data set *equal*, the measurement setup for the five observed baselines (cf. Figure 5.2) is completely identical in each case. This includes the same spacer and antenna type, as well as the same placement of the antenna cables. By comparison, in the data set *mixed*, different antenna types and spacer lengths were combined. Due to the short baseline lengths and the minimal height variation of the pillars, significant ionospheric or tropospheric effects can be excluded as a reason for the decreasing accuracy level. Hence, only the different spacer and antenna types at both stations can cause this deterioration, and thus, the increasing standard deviations and shifted mean values can be ascribed to the different near-field situations at both pillars. In addition, the higher influence of the different near-field situations on the height component corresponds to the results obtained in Dilßner [2007] from zero-baseline tests.

In consequence it can be concluded that equal antenna setups lead to a similar near-field situation at both pillars, and thus, the reduction of the near-field influence becomes possible by forming double-differences during the relative position estimation.

5.1.3 Summary

In the two previous Sections 5.1.1 and 5.1.2, the possibility of reducing antenna near-field effects from a metrological point of view and the associated requirements were described. The following conclusions can be drawn from these investigations, which were also included in guidelines for high-precision GNSS-based distance measurements [Bauch et al., 2016; Astrua et al., 2017] and for the application of GNSS antenna corrections [Görres et al., 2018].

1.) An equal antenna setup at both ends of a GNSS baseline enables the minimization of antenna near-field effects during the double-differencing process.

2.) The usage of antenna spacers leads to a substantial additional effort in terms of leveling and centering of the antenna spacer. Furthermore, from a certain height of the spacer ($\geq$40cm), the whole setup becomes unstable and can introduce additional errors in the coordinate solution.

3.) Combining the statements of conclusions 1.) and 2.), in general the use of antenna spacers $\geq$20cm is not recommended. In particular, this applies to high-precision GNSS applications. Nevertheless, it should be emphasized that, depending on the accuracy requirements of the measurement task at hand, possible accuracy losses of a few millimeters associated with the use of antenna spacers may be acceptable.

4.) Even in case of an identical antenna setup, individual antenna calibrations cannot be neglected. Since the calibration parameters for the same antenna type can differ by several millimeters, their influence on the positioning accuracy cannot be reduced by forming double-differences of the GNSS observations and consequently, using type-mean calibration parameters is not sufficient to reach highest accuracies. Furthermore, the calibration parameters are actually only valid for the near-field situation present during the calibration procedure (cf. Section 3.2.4). Thus, using calibration parameters from different calibration facilities can also affect the accuracy of the coordinate solution. This aspect is further discussed in Section 6.4.

5.2 Analysis of the influence of the satellite geometry and its consideration in kinematic applications

Objects in the antenna environment, such as buildings or vegetation, or the terrain structure itself can obstruct satellite signals. This leads inevitably to a reduction of the number of satellite signals available for the position determination and possibly to a deteriorated satellite geometry. However, it is difficult to analyze this influence at such locations, since obstructions are usually accompanied by other site-dependent effects, such as signal diffraction or far-field multipath, and the individual impact of the different effects on the positional accuracy is hard to separate. Therefore, a simulation-based approach is used to isolate and analyze the effect of a deteriorated satellite geometry (Publication A, Zimmermann et al. [2016]).
One of the main objectives of this dissertation is the development and analysis of methods to minimize site-dependent effects by selecting unaffected satellite signals. This selection process deliberately reduces the number of satellite signals, which automatically leads to a negative impact on the satellite geometry. Hence, the results from the investigations in Publication A [Zimmermann et al., 2016] help to assess the extend of this influence.
A second aspect related to the satellite geometry that is considered within this dissertation is an optimized waypoint planning for automated UAV flights. For this purpose, the data of a real UAV trajectory is used to derive geometry maps that consist of realistic measures for the quality of the satellite geometry and enable the UAV to adapt the original flight plan (Publication C, Zimmermann et al. [2017b]).

In the following sections, the main aspects of both investigations are described.

5.2.1 Influence of satellite obstructions on the positional accuracy

The basic idea in the empirical analysis of the influence of the satellite geometry on the accuracy of the position determination is similar to the investigations on antenna near-field effects, described in Section 3.2.4. By eliminating, or at least minimizing all other systematic errors, the influence of the satellite geometry can be considered in isolation. Consequently, the observation material from the near-field investigations represents an ideal data basis. Furthermore, due to the findings from the near-field investigations, only the observations from identical antenna setups are used.

In advance to the simulation-based analysis of satellite obstructions, four generic obstruction scenarios called *Tree*, *Wall*, *Canyon* and *Mining*, are defined, which are shown in Figure 5.4. In each of the scenarios, either man made objects, vegetation, or the terrain structure lead to obstructed areas that limit the satellite visibility to a different extend. While scenario *Tree* (cf. a) in Figure 5.4) simulates the obstruction induced by a tree on a single antenna, in scenarios *Wall* and *Canyon*, the satellite visibility of both antennas is affected (cf. b) and c) in Figure 5.4). The obstruction induced by locations like an opencast coal mine is simulated in scenario *Mining*, whereby in this case, the satellite visibility of each antenna is limited differently (cf. d) and e) in Figure 5.4).

The obstruction simulation consists of three steps: 1.) determination of azimuth and elevation angles of the visible satellites from a stand alone single point positioning solution (cf. Section 3.1.2), 2.) identification of obstructed satellites by comparison to the scenario specific obstruction boundaries and 3.) manipulation of observation files by excluding the signals of the obstructed satellite. Afterwards, a baseline solution is carried out, using the same parameter settings as for the original data set.
In Figure 5.5, the number of satellites and the PDOP values before and after the simulation of the scenario *Canyon* are shown for one observation session at one pillar exemplarily.

After the simulation, the average number of visible satellite drops from 11 (original data set) to a value of 6, with a minimum of 4 and a maximum of 8 visible satellites, respectively. The PDOP values, used here as a measure of the quality of satellite geometry (cf. Section 3.2.1), show a small variation in the case

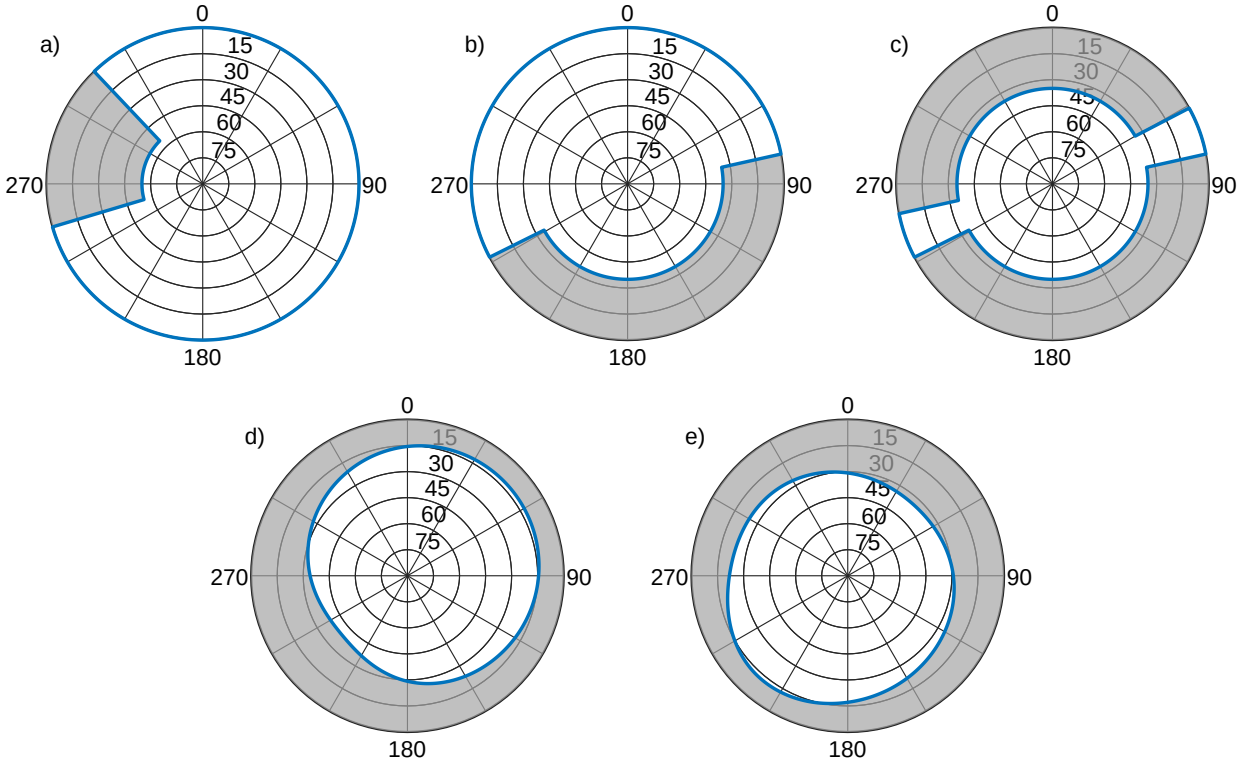


Figure 5.4: Generic satellite obstruction scenarios: a) Scenario *'Tree'*, b) Scenario *'Wall'*, c) Scenario *'Canyon'*, d)/e) Scenario *'Mining'*. The grey shaded area represents the obstruction zone and the blue line bounds the unobstructed area with free satellite visibility.

of the original observational data and, with an average value of 2, are constantly below 3, which is often referred to as the limit for a good geometry [Hofmann-Wellenhof et al., 2008]. In comparison, the average PDOP of the manipulated data set is 4.2, and thus, exceeds the limit of 3 less than it was expected for this scenario, due to the considerable limitation of the satellite visibility. Nevertheless, considering the curve of the DOP values shown in Figure 5.5, about 74% of the PDOP values exceed the limit of 3 and large variations between values of 1.8 and 14.4 occur over the entire observation period. On the one hand, this indicates that the influence of a poor satellite geometry can be compensated by a longer observation time. On the other hand, it becomes clear that different observation durations have to be considered for a reliable analysis of the influence.
For this reason, the obstruction simulation is additionally carried out for reduced observation times of 1 and 2 hours and afterwards the entire manipulated data material is used for the relative position determination. In Tables 5.2 and 5.3, the resulting mean distance and height differences and their respective standard deviations are listed for the different obstruction scenarios and observation durations.

It becomes clear that, compared to the original data set, none of the scenarios, even with a reduced observation duration, leads to a significant deterioration of the accuracy. Although there is a slight increase in the standard deviation of the height differences visible, all values remain below one millimeter. Hence, it can be concluded that the mere deterioration of the satellite geometry, induced by the four generic obstruction scenarios, does not significantly influence the positional accuracy. In each of the scenarios, an observation duration of 1 hour is sufficient to achieve an accuracy better than one millimeter.

The investigations described here are considered as a possibility to assess the influence of the deterioration of the satellite geometry, deliberately caused by the detection and exclusion of satellite signals, affected by NLOS reception, signal diffraction or far-field multipath (Publications B-E, Zimmermann et al. [2017a,b,

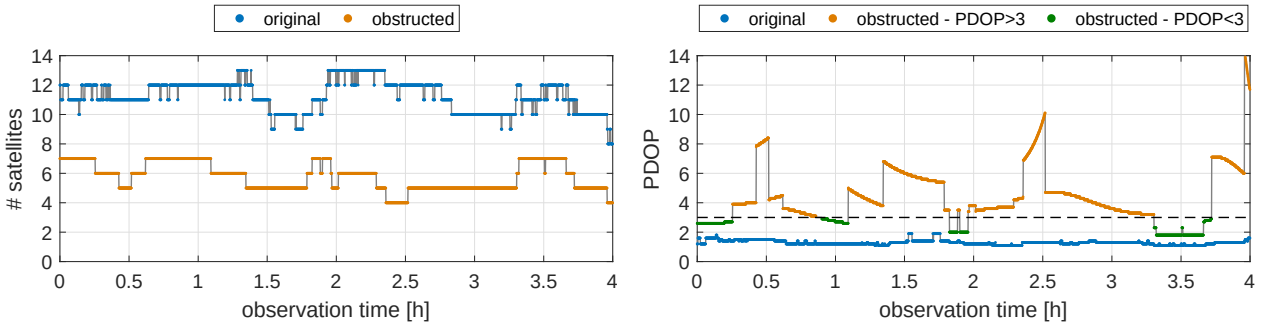


Figure 5.5: Number of satellites (left) and PDOP values (right) before and after the simulation of scenario *Canyon* for one observation session at one pillar. In the right panel, the ocher dots denote PDOP values higher, and the green dots denote PDOP values lower than 3 (black dashed line).

Distance differences $\Delta d\,[mm]$

	Observation duration					
	4h		2h		1h	
Scenario	$\overline{x}$	$\sigma_{\overline{x}}$	$\overline{x}$	$\sigma_{\overline{x}}$	$\overline{x}$	$\sigma_{\overline{x}}$
Original	0.14	0.31	0.16	0.41	0.15	0.38
Tree	0.07	0.38	0.04	0.42	0.01	0.44
Wall	0.23	0.41	0.18	0.42	0.16	0.41
Mining	0.15	0.38	0.12	0.43	0.14	0.43
Canyon	0.21	0.40	0.14	0.43	0.09	0.41

Table 5.2: Mean distance differences $\overline{x}$ and respective standard deviations $\sigma_{\overline{x}}$ before and after the simulation of the different obstruction scenarios for observation durations of 1, 2 and 4 hours.

Height differences $\Delta h\,[mm]$

	Observation duration					
	4h		2h		1h	
Scenario	$\overline{x}$	$\sigma_{\overline{x}}$	$\overline{x}$	$\sigma_{\overline{x}}$	$\overline{x}$	$\sigma_{\overline{x}}$
Original	0.02	0.46	0.16	0.65	0.22	0.74
Tree	0.07	0.46	0.15	0.62	0.26	0.74
Wall	0.09	0.46	0.17	0.62	0.08	0.74
Mining	0.32	0.87	0.37	0.88	0.37	0.67
Canyon	0.13	0.60	0.37	0.67	0.37	0.71

Table 5.3: Mean height differences $\overline{x}$ and respective standard deviations $\sigma_{\overline{x}}$ before and after the simulation of the different obstruction scenarios for observation durations of 1, 2 and 4 hours.

2018, 2019]). Based on the results it can be concluded that the quality of the satellite geometry plays a subordinate role in this context and its influence can be denoted as being marginal in comparison to the other site-dependent effects (cf. in particular Sections 3.2.2 and 3.2.3). The expected gain in accuracy, due to the reduction of the other site-dependent effects, should clearly exceed the negative influence of a deteriorated satellite geometry.

Under much more severe conditions than the scenarios simulated here, the satellite visibility can be restricted to such an extent that extremely unfavorable satellite constellations occur, or even the number of available satellites drops below the minimum required number of 4. Considering the number of available satellites shown in Figure 5.5, it becomes obvious that even in the scenarios that have been simulated during the investigations presented in this section, only this minimum number is reached at various points in time. Hence, under more severe conditions, the inclusion of further GNSS, such as GLONASS or Galileo, could be a possible solution. This point is taken up again in Section 6.1.

5.2.2 Optimized waypoint planning of UAVs

Since the absolute positional accuracy and the direct georeferencing of the related mapping products are partially also dependent on the respective 3D environment of the UAV, it is straightforward to include information about the expected GPS measurement conditions in the flight planning. In this context, a distinction should be made between two types of flight planning. Probably the most common form of flight planning is that which is carried out prior to the actual flight. Taking into account aspects such as safety, economy,

ground-sampling distance or image overlapping, coordinates of waypoints are predefined, which the UAV should autonomously navigate to [Gandor et al., 2015]. The flight manoeuvres performed by the UAV therefore serve only the purpose of not leaving the predefined flight route. Another type of flight planning describes the process in which the UAV determines the flight route and adapts it to the given conditions. Therefore decisions have to be made, based on the given environment, the implemented exploration algorithms and the actual mission, for example pure navigation, or mapping of the environment or a specific object. In this case, the UAV decides independently which flight route best contributes to the accomplishment of the given task [Nieuwenhuisen & Behnke, 2015].
The expected GPS measurement conditions, which can be assessed using DOP values (cf. Section 3.2.1), are a criterion that can support the decision making process in both types of flight planning. Although it was shown in the previous section that a poor satellite geometry does not necessarily lead to an inaccurate position determination, it is advisable to preventively avoid such waypoints in the planning phase. This is due to the fact that it is difficult to predict the magnitude of the other site-dependent effects, which are often linked to a deteriorated satellite geometry due to buildings or vegetation in the antenna environment. Nevertheless, forecasting realistic DOP values, either using the broadcast ephemeries, or using data of an almanac, requires an integration of the antenna environment to account for possible signal blockages induced by buildings or vegetation. Under the assumption that the UAV environment is a-priori known or reconstructed during the flight by the onboard mapping sensors, a visibility analysis must be performed to identify the satellites actually visible at potential waypoints and to evaluate the quality of the available satellite constellation. Therefore, a set of candidate positions for possible waypoints is predefined and the visibility analysis is carried out in the following steps:

1.) Generalization of the 3D model with plane segments.
2.) Determination of line-of-sight (LOS) vectors from all different candidate positions to all available satellite positions given by the ephemeris data.
3.) Calculating a vector-plane intersection for all LOS vectors and planes of the 3D model.
4.) Testing the intersection points, whether they are inside the restricting polygon for each plane, and whether they are between the candidate position and the satellite.
5.) Identification of obstructed satellites. If both tests in step 4 are positive, the respective satellite signal will be blocked at this candidate position.

After the visibility analysis, the positions of the visible satellites can now be used to determine realistic PDOP values for all candidate positions, following Equations (3.8) and (3.10) in Section 3.2.1.
This procedure results in a grid of PDOP values representing a geometry map that can contribute to the decision making process in both of the aforementioned types of waypoint planning.

In Figure 5.6, the PDOP values determined for a trajectory of a remotely controlled UAV flight are shown. The gray shaded planes represent objects in the UAV environment, i.e. a building, a tree and a simplified representation of the vegetation on the left side of the trajectory. This emphasizes, how the quality of the satellite geometry can vary during a flight. In the case of a fully autonomous UAV flight, the red waypoints, indicating a poor satellite geometry, should ideally be prevented as far as possible, to avoid long-term GPS losses of lock and to provide high positioning accuracies in the direct georeferencing. In Figure 5.7, the geometry map for one of these waypoints is shown exemplarily, whereby the distance between the candidate positions is set to 50 centimeters. For reasons of clarity only one 2D segment of the geometry map is shown. Assuming that the trajectory shown in Figure 5.6 corresponds to a planned flight route, the trajectory could be adapted by including the geometry map in such a way that the areas with poor satellite geometry (red dots in Figure 5.6) can be avoided. In the case of a completely autonomous flight, the aim is to navigate to the green areas of the geometry map (cf. Figure 5.7) at regular intervals in order to keep possible GPS failures as short as possible.

5.2.3 Summary

In the previous sections, the quality of the satellite geometry was considered from two different points of view. In Section 5.2.1, the influence of a deteriorated satellite geometry was investigated isolated from other

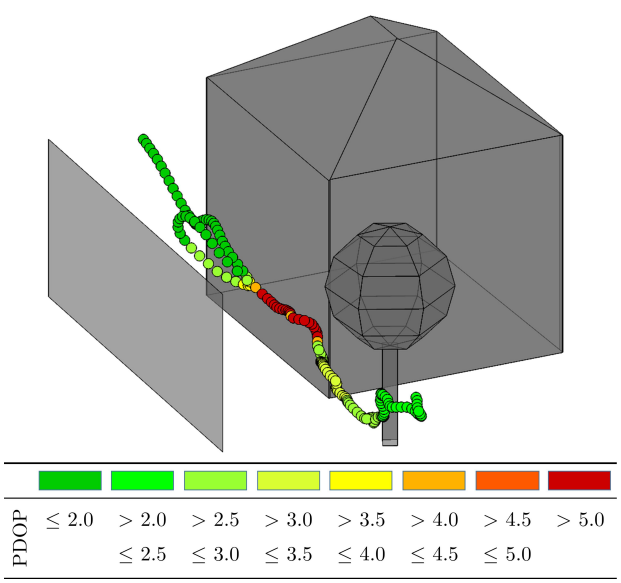


Figure 5.6: Site-dependent PDOP values (colored dots) for a trajectory of a remotely controlled UAV flight along a building (right) and a simplified representation of vegetation (left wall).

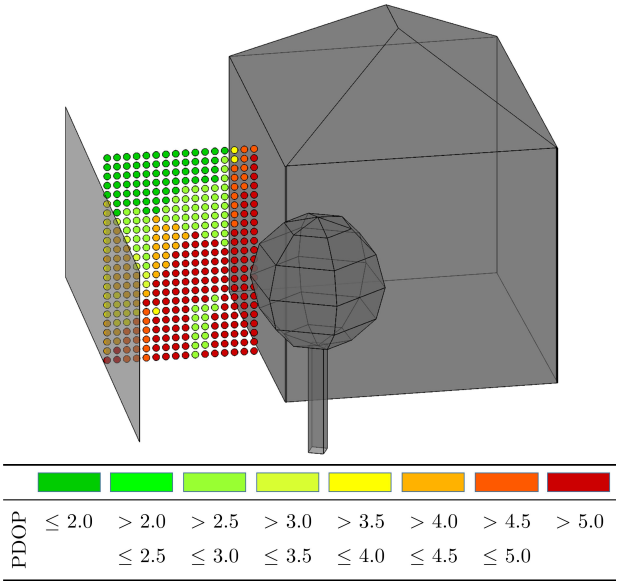


Figure 5.7: Site-dependent geometry map (colored dots) for a 2D area between a building (right) and a simplified representation of vegetation (left wall).

effects and its magnitude was determined on the basis of simulated obstruction scenarios. In Section 5.2.2, quality measures of the satellite geometry were used to optimize the waypoint planning of UAVs. From these investigations, the following conclusions can be drawn:

1.) The mere influence of a poor satellite geometry can be denoted as being marginal compared to the influence of other site-dependent effects. Hence, a detection and elimination algorithm for NLOS reception, signal diffraction and far-field multipath will automatically weaken the satellite geometry, but the associated negative impact will be compensated by the reduction of these effects and can therefore be considered as uncritical. Nevertheless, under extremely unfavorable GPS conditions and an already strongly limited number of visible satellites, the detection and elimination algorithm could weaken the geometry to such an extend that an integration of satellite signals from other GNSS could become necessary (cf. Section 6.1).

2.) The developed method for the determination of geometry maps uses environment models to realistically assess possible waypoint candidates. Hence, unexpected signal blockages and long GPS failures can be prevented in the planning phase, as well as during the UAV flight. Furthermore, in situations, where the other site-dependent effects cannot be sufficiently be reduced, the geometry maps can help to navigate back to waypoints with less severe GPS measurement conditions.

5.3 Mitigation of NLOS reception and signal diffraction in static and kinematic applications

Non-line-of-sight (NLOS) reception and signal diffraction are site-dependent effects that occur when the direct signal path is obstructed by objects in the vicinity of the antenna and the antenna only receives a reflected or diffracted satellite signal (cf. Section 3.2.3). Since the antenna has no high-level logic implemented to separate these signals from signals received on the direct signal path, the magnitudes of these effects are theoretically unbounded and therefore their mitigation is of particular importance for an accurate satellite-based position determination.
The investigations regarding the mitigation of NLOS reception and signal diffraction are one of the main aspects of this dissertation. The principal idea is to use georeferenced TLS point clouds of the antenna environment to identify affected satellite signals by a geometrical visibility analysis and to exclude them from the subsequent position determination. For this purpose, the boundary of the unobstructed part of the sky is extracted from the view of an a-priori known approximate antenna position solution. Therefore, the azimuth and elevation angles of all points of the point cloud are determined in relation to the antenna position and afterwards the physical horizon is derived from these values. For the detection and elimination of affected satellite signals, this horizon is subsequently used as an elevation mask that adaptively reflects the site-dependent obstruction situation. In the following, these elevation masks are referred to as obstruction adaptive elevation masks (OAEM).
To illustrate the described procedure above, Figure 5.8 shows the resulting OAEM for an antenna position in an urban environment, including the GPS satellite tracks for an 8 hour observation period in a skyplot. Additionally, an aerial image and the TLS point cloud of the antenna environment on which the elevation mask is based are depicted.

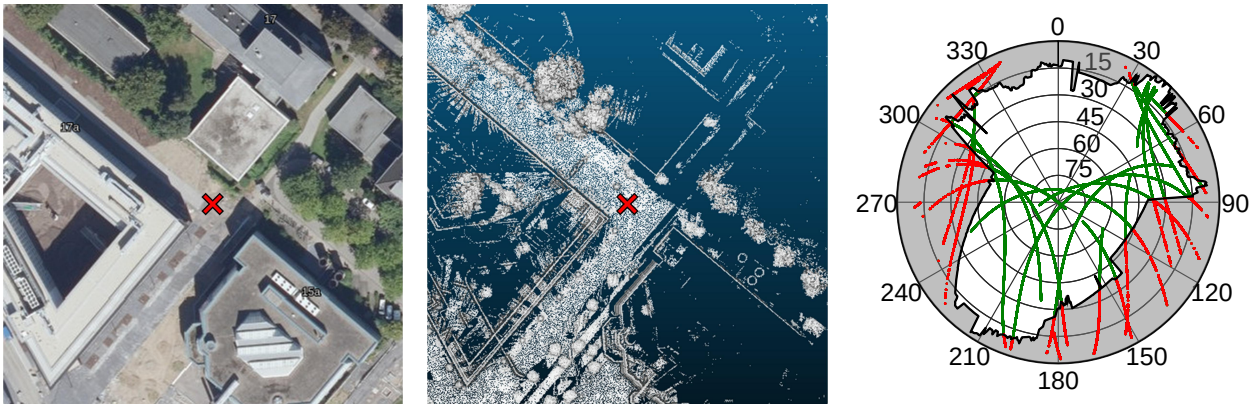


Figure 5.8: Aerial image[1](left), TLS point cloud (middle) and obstruction adaptive elevation mask (right) including satellite tracks. The green dots in the right panel indicate an unobstructed view, the red dots denote satellite signals that are actually blocked by the surrounding objects. The red cross in the left and middle denotes the antenna position.

The black line denotes the OAEM and represents the physical horizon of the antenna environment. The red points of the satellite tracks denote satellite signals that are blocked by the surrounding obstacles (grey shaded area in right panel of Figure 5.8), and thus, are either received after diffraction at the obstacles, or via NLOS reception (cf. Section 3.2.3). After the detection of these signals by the OAEM, the remaining unaffected signals can be selected and used for the position determination.

As already mentioned in Section 3.2.3, it can be assumed that the probability for diffraction effects might be higher than for NLOS reception. In this context, the reflection points for all satellite signals detected by the OAEM were exemplarily computed for the scenario shown in the left panel of Figure 5.13 on page 51, under the assumption of a pointwise and single reflection. Since none of the reflection points is located on

[1] ©https://www.tim-online.nrw.de/tim-online2/, last accessed: 06.02.2019

one of the vertical reflecting surfaces, it turns out that actually none of the satellite signals is subject to NLOS reception, at least under the made assumption. Nevertheless, since the underlying cause is identical for both effects and multiple reflections or a mixture of both effects cannot be excluded, it is not explicitly distinguished between signal diffraction and NLOS reception in the further investigations. However, since the OAEM is designed to detect affected signals based on the origin of the effects, this does not affect the effectiveness of the mitigation technique.

In the context of the development and analysis of the concept of obstruction adaptive elevation masks, the following questions arise that are of particular relevance:

- OAEMs are derived from TLS point clouds. Are there any requirements or limitations regarding the point cloud density?
- The determination of OAEMs requires an initial estimate of the antenna position. How can the uncertainty of this approximate solution be taken into account?
- Is it sufficient to perform a mere geometrical visibility check of the line-of-sight vector, or should also the theory on wave propagation be considered?
- Are there any differences in performance of the OAEMs in the case of static or kinematic GNSS applications[2]?
- How can the dependency on an a-priori known georeferenced point cloud be avoided?

All of these questions were addressed in this dissertation (Publications B-E, Zimmermann et al. [2017a,b, 2018, 2019]) and the main aspects are described in the following sections. Section 5.3.1 presents the concept of obstruction adaptive elevation masks in more detail and analyzes the influences of the point cloud density and the initial antenna position, as well as the integration of Fresnel zones. Sections 5.3.2 and 5.3.3 assess the performance of OAEMs in static and kinematic GNSS applications and Section 5.3.4 describes the derivation of OAEMs without the prior availability of a georeferenced point cloud.

5.3.1 The concept of Obstruction Adaptive Elevation Masks

The determination of an OAEM is based on the coordinates of a TLS point cloud of the antenna environment and an approximate position of the antenna phase center, both given in the global coordinate frame. In a first step, the LOS vectors from the initial antenna position $\mathbf{X}^R$ to every point of the point cloud $\mathbf{X}_i^P$ is determined and after transforming the LOS vector to a local topocentric coordinate system, the respective azimuth and elevation angles ψ_i and θ_i can be computed by

$$\psi_i = \arctan\left(\frac{e_i}{n_i}\right) \tag{5.1}$$

$$\theta_i = \arctan\left(\frac{u_i}{\sqrt{e_i^2 + n_i^2}}\right), \tag{5.2}$$

where e_i, n_i and u_i are the east-, north- and up-component of the LOS vector in the topocentric coordinate system. To relate the computed elevation angles to the obstacles in the antenna surrounding, the elevation angles are allocated to an azimuthal grid with a predefined cell width (e.g. 0.5°). Finally, the highest elevation angle $\overline{\theta}$ is identified in every cell c following

$$\overline{\theta}_c = \begin{cases} max\left\{\theta_i \in c\right\}, & \text{cell } c \neq [\,] \\ 0°, & \text{cell } c = [\,], \end{cases} \tag{5.3}$$

whereby in the case that a cell is not filled, i.e. no obstructions are present in this azimuth area, the elevation angle is set to 0°. Now the OAEM is represented by a fully populated 360° index vector that can be used as a

[2]In this dissertation, the position determination is referred to as a kinematic application when the antenna is deliberately moved and the position is determined at different locations (e.g. trajectory estimation of vehicles). In contrast, applications, in which the antenna remains at one location but the observation data is evaluated kinematically, i.e. on an epoch by epoch basis, are counted as static applications (e.g. monitoring tasks).

Look-Up-Table to identify satellite signals that are subject to NLOS reception or signal diffraction. Therefore, the azimuth and elevation angles of the satellites are determined and compared to the OAEM value that corresponds to the respective azimuthal direction. If the OAEM value is higher than the satellite elevation angle, the satellite signal is actually blocked, and thus, it is subject to at least one of the aforementioned effects (cf. red dots in right panel of Figure 5.8).

However, the success rate of this detection process depends on several factors. On the one hand, the congruence between OAEM and reality, and thus, in turn the success rate, depends on the density of the point cloud. On the other hand, the uncertainty of the initial antenna position influences the accuracy of the OAEM values. In the following, both aspects are discussed. Furthermore, the integration of Fresnel zones into the concept of OAEMs as an option to extend the geometrical visibility check of the LOS vector by the wave propagation theory is described.

Influence of the point cloud density

The point cloud density can be defined as the minimal point-to-point distance in a point cloud. Increasing the point-to-point distance effectively reduces the number of points of the point cloud and leads to an acceleration of the OAEM determination. Hence, especially for huge data sets or iterative applications (cf. Section 5.3.4) this can be necessary. On the other hand, this can be accompanied by a reduction of the level of detail in the determined OAEM and increases the risk that parts of the obstructing objects are no longer covered by the OAEM. This holds especially true for thin objects, such as lightning conductors or other kinds of masts in the antenna surrounding. For the scenario shown in Figure 5.8, the congruence of OAEMs determined from an accurately known antenna position and point clouds with different point-to-point distances is compared. Therefore, the OAEM derived from a point-to-point distance of 5cm is used as reference and the differences of the OAEM values for point-to-point distances of 10cm, 20cm and 50cm are computed. The results, including the number of satellite signals that erroneously pass the different OAEMs are shown in Figure 5.9.

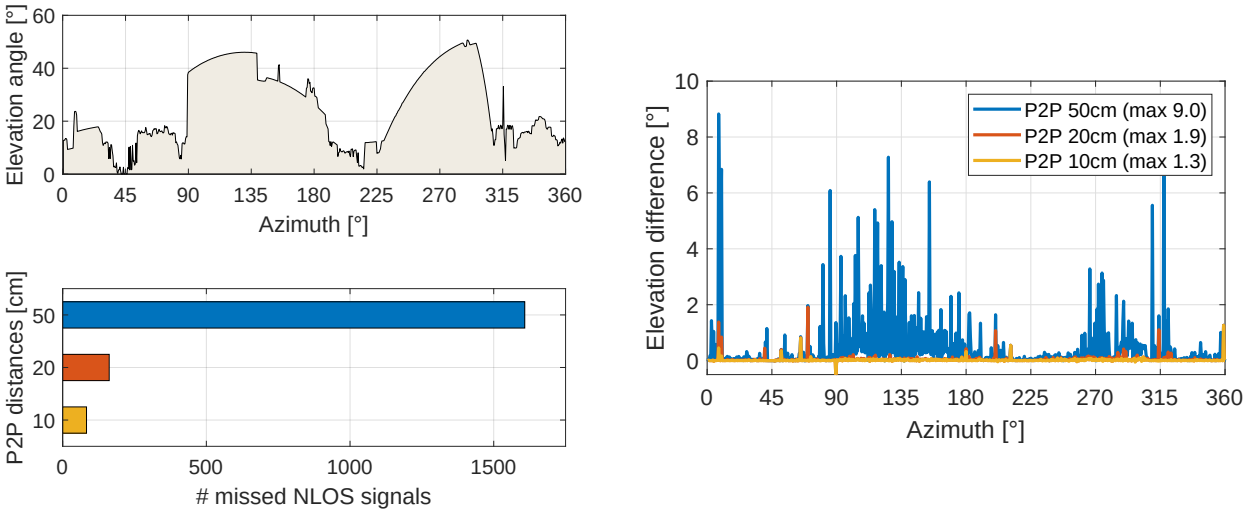


Figure 5.9: Panoramic view of reference OAEM derived from point-to-point distance of 5 centimeters (top left), number of missed NLOS signals for different point-to-point distances (bottom left) and differences of OAEM values for different point-to-point distances (right).

As was the expectation, the largest differences of the OAEM values occur for a minimum point-to-point distance of 50cm. Particularly in the areas of the surrounding buildings, the deviations reach values of up to 9°, which indicates that the finer details of the roof structures can no longer be resolved. This also results in a much larger number of satellite signals passing the OAEM, although they are affected by NLOS reception or signal diffraction. On the other hand, it is noticeable that the discrepancies of both, the differences of the

OAEM values and the number of missed signals between the two OAEMs, based on 10cm and 20cm point-to-point distance respectively, are significantly smaller. Nevertheless, by increasing the minimum point-to-point distance from 10cm to 20cm, the reduction of the total number of points increases significantly from about 70% to nearly 90%. Consequently, for this scenario a minimum point-to-point distance of 20cm represents a good compromise between the level of detail of the OAEM and the size of the point cloud. However, depending on the characteristics of the antenna environment, an adjustment may be necessary and should therefore be checked on a case-by-case basis.

Consideration of the initial antenna position uncertainty

This step is of particular importance, since the OAEM values determined from an erroneous antenna position can be too low compared to the true but unknown values. As a result, satellite signals that are actually subject to NLOS reception and signal diffraction may pass the OAEM and deteriorate the position determination. In order to account for the uncertainty of the initial antenna position, a cellwise adjustment is performed. Therefore, the uncertainty of the OAEM value $\sigma_{\overline{\theta}}$ in each cell is determined by propagating the uncertainty of the initial antenna position onto the respective elevation angle, following the law of error propagation [Koch, 1999] by

$$\sigma_{\overline{\theta}_c} = \sqrt{\mathbf{F} \cdot \mathbf{\Sigma}_{\mathbf{X}^R} \cdot \mathbf{F}^T}, \tag{5.4}$$

where $\mathbf{F}$ contains of the partial derivatives of Equation (5.2) in relation to the components of the respective LOS vector and $\mathbf{\Sigma}_{\mathbf{X}^R}$ is the covariance matrix of the initial antenna position in the topocentric coordinate system. Afterwards, $\sigma_{\overline{\theta}_c}$ serves as an adjustment value and is added to the OAEM value of the respective cell to compute the adjusted OAEM value $\hat{\theta}_c = \overline{\theta}_c + \sigma_{\overline{\theta}_c}$.
From numerical simulations and the analyses of several scenarios (Publications B-C, Zimmermann et al. [2017a,b]) follows that the uncertainty of the initial antenna position should not exceed 20 centimeters, in order to avoid values of $\sigma_{\overline{\theta}}$ higher than 5°. However, the magnitude of $\sigma_{\overline{\theta}}$ also depends on the height and distance of the obstructing object, and thus, a general statement regarding the permissible uncertainty of the initial antenna position is difficult and this aspect should be considered individually in each case.

The combination of the adjustment of the OAEM values and the procedure described at the beginning of this section leads to the development stage 1 of the OAEM concept, schematically illustrated in Figure 5.10.

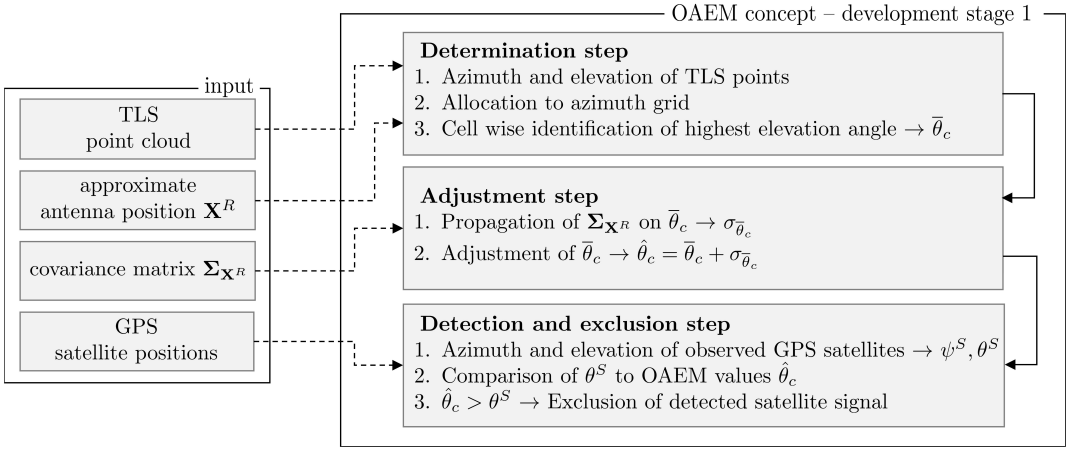


Figure 5.10: Schematic illustration of OAEM concept – development stage 1, consisting of a determination, an adjustment and a detection and exclusion step, respectively.

Obstruction adaptive elevation masks in this development stage were tested in both, static and kinematic scenarios and their performance with respect to minimizing the influence of NLOS reception and signal diffraction was analyzed and evaluated (Publications B-C, Zimmermann et al. [2017a,b]). The results of these investigations are described in detail in Sections 5.3.2 and 5.3.3.

Integration of Fresnel zones

A further possibility to optimize the detection and exclusion process for mitigating NLOS reception and signal diffraction is the consideration of the theory of electromagnetic wave propagation (Publication E, Zimmermann et al. [2019]). Up to this point, a linear satellite signal was considered and the visibility analysis is based on the comparison of elevation angles determined from the LOS vectors. However, as already described in Section 3.3, most of the signal energy is transmitted within an ellipsoid of revolution, instead of on a straight line. As a result, signal distortions can already occur while the direct line of sight (assumed to be linear) is not blocked by objects in the antenna environment, but the satellite signals propagate close enough to the objects, so that the ellipsoid is penetrated (cf. Figure 3.9).
Since the OAEM determination is based on the 3D coordinates of the obstructing objects in the antenna environment, the distance between the object and the antenna is known. Based on this information, the radius of the ellipsoid, i.e. the radius of the first Fresnel zone, can be determined for this distance on the LOS vector of each satellite following Equation (3.24). Now it is possible to check whether a part of the Fresnel zone intersects with the OAEM, and thus, possible signal distortions can already be detected before a complete blocking of the satellite signal occurs. Figure 5.11 graphically illustrates the procedure described above.

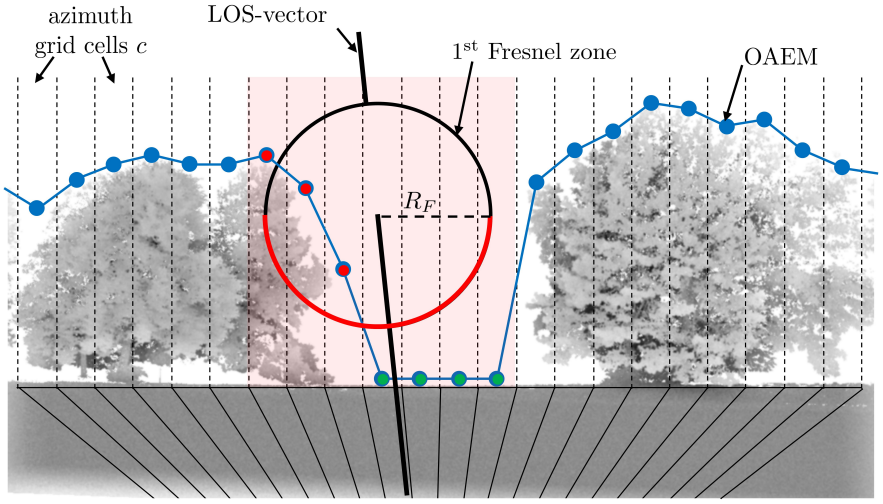


Figure 5.11: Diffraction identification using the Fresnel zones concept. The OAEM is represented by the elevation angles (blue dotted line) and the respective azimuth grid cells c. The half red and half black circle represent the first Fresnel zone with radius R_F on the direct signal path along the LOS-vector to the respective satellite. The red shaded cells indicate an overlap with the Fresnel zone, and the red and green dots denote whether the elevation angles of points on the red semicircle are lower than the OAEM or not.

For the identification of obstructed areas of the Fresnel zone it is sufficient to test if any part of the lower semicircle of the Fresnel boundary (red part in Figure 5.11) is lower than the elevation angles in the related OAEM grid cells. Moreover, it becomes obvious that in each cell only the lowest point of the Fresnel zone boundary, which equals the intersection point of the Fresnel zone boundary and the respective grid border, needs to be considered. Hence, for these intersection points the elevation angle is determined and compared to the respective OAEM value. If the OAEM value is higher, the Fresnel zone of this satellite signal is obstructed in this grid cell and the risk of potential signal distortions increases.

The inclusion of the Fresnel zone concept extends the detection and exclusion process of the OAEM to development stage 2, which now also enables the minimization of signal distortions that would not be detected by a mere geometrical consideration of the signal propagation (cf. Figure 3.4). The development stage 2 of the OAEM concept is schematically illustrated in Figure 5.12.

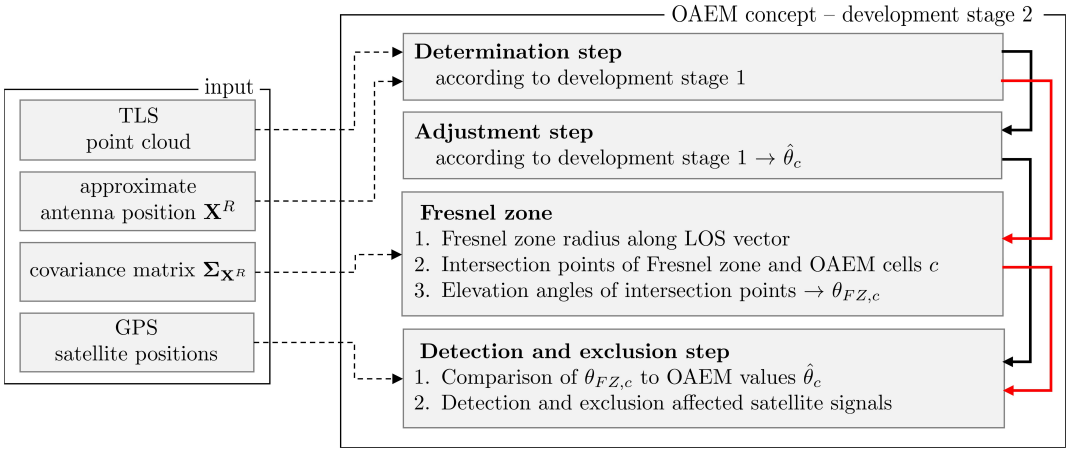


Figure 5.12: Schematic illustration of OAEM concept – development stage 2, consisting of a determination, an adjustment and a modified detection and exclusion step, considering Fresnel zones for the LOS transmission.

The performance of both development stages of the OAEM concept was compared and assessed in a static scenario (Publication E, Zimmermann et al. [2019]). The results of this comparison are described in the following Section 5.3.2.

5.3.2 OAEM performance in static applications

The performance of obstruction adaptive elevation masks in minimizing NLOS reception and signal diffraction is demonstrated by two static scenarios. In Scenario 1 (Publication B, Zimmermann et al. [2017a]) the antenna is placed between two buildings and the OAEM concept in development stage 1, i.e. without considering the Fresnel zone concept, is applied to the observation data. In scenario 2 (Publication E, Zimmermann et al. [2019]), the antenna is located on a sports field, partly surrounded by dense vegetation. In this case, the Fresnel zone concept is integrated into the selection process, and thus, both development stages of the OAEM concept are used for the mitigation of signal diffraction. In Figure 5.13, an aerial image and the obstruction adaptive elevation mask, determined following the scheme described in Section 5.3.1 (development stage 1), is shown for both scenarios.

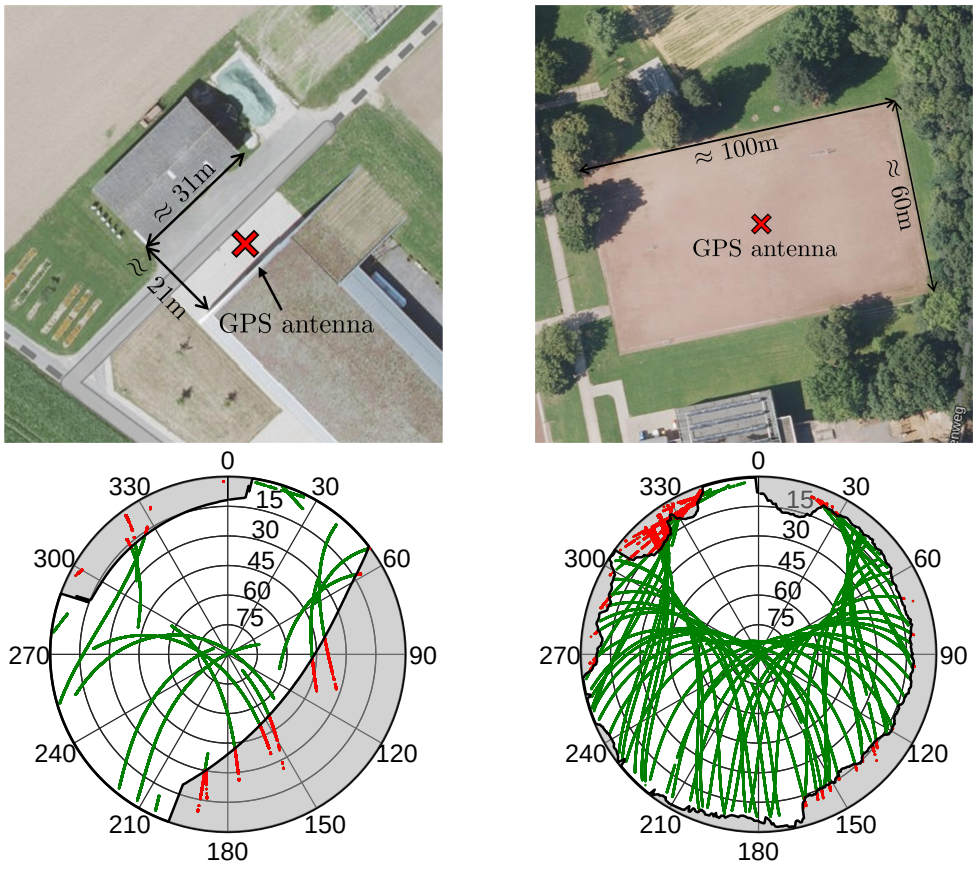


Figure 5.13: Aerial images[3](top) and obstruction adaptive elevation masks (bottom) including satellite tracks for static scenarios 1 (left) and scenario 2 (right). The green dots in the bottom panel indicate an unobstructed view, the red dots denote satellite signals that are actually blocked by the surrounding objects. The red cross in the top panels denote the antenna positions in each scenario.

In both scenarios a reference solution for the antenna position is available, either from terrestrial measurements (scenario 1) or from GNSS long-term observations (scenario 2). Furthermore, the antenna environment was captured with a terrestrial laser scanner in advance of the measurements and the resulting point cloud was georeferenced using targets with beforehand determined GNSS-RTK positions.

In the following, the results of both scenarios are separately discussed.

[3] ©https://www.tim-online.nrw.de/tim-online2/, last accessed: 07.02.2019

Scenario 1 – Buildings

After the original data set is modified by excluding satellite signals that were detected by the OAEM as being subject to NLOS reception or signal diffraction (cf. red dots in left bottom panel of Figure 5.13), for both data sets a baseline solution is carried out, where the observations are processed in a static batch solution and kinematically, on an epochwise basis. Afterwards, the differences to a reference solution from terrestrial measurements are determined. Table 5.4 lists the coordinate differences resulting from the batch solution for the original and modified data set in a topocentric coordinate system. In Figure 5.14, the respective differences in the up component of the kinematic solution are shown exemplarily. Furthermore, Table 5.5, shows the percentage of epochs, where the carrier phase ambiguities could successfully be fixed to integer values.

OAEM applied	North [mm]	East [mm]	Up [mm]
No	-12.0	5.7	-12.6
Yes	0.6	-1.8	-0.8

Table 5.4: Coordinate differences for static scenario 1 before and after the OAEM is applied to the observation data.

OAEM applied	Fixed ambiguities	
	Yes	No
No	56%	44%
Yes	100%	0%

Table 5.5: Percentage of epochs with fixed ambiguities before and after the OAEM is applied to the observation data set for the kinematic baseline solution.

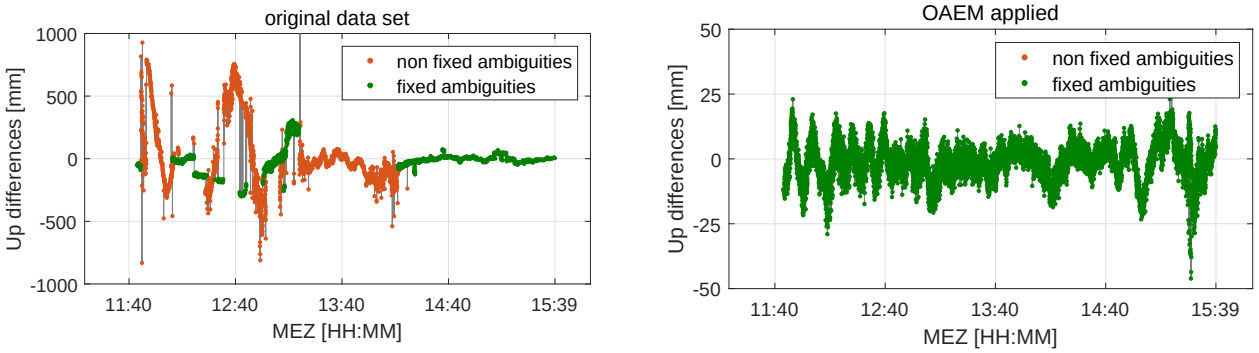


Figure 5.14: Coordinate differences of epochwise baseline solution before (left) and after (right) the OAEM is applied to the observation data. The red dots denote epochs with float ambiguities and the green dots denote fixed ambiguities, respectively.

The results of both, the static and the epochwise solution demonstrate the effectiveness of obstruction adaptive elevation masks in reducing NLOS reception and signal diffraction. After the static baseline solution is carried out, all coordinate components show a significant improvement. While the differences of the north and up component resulting from the original data exceed an absolute value of one centimeter, the coordinate differences after the application of the OAEM only vary between 0.6mm and -1.8mm, respectively. The results of the kinematic evaluation particularly show the positive effect of the OAEM on the carrier-phase ambiguity solution. While in the original data set with 56%, a successful ambiguity solution was only possible in almost half of the epochs, the percentage increases to 100% after the selection of the unaffected satellite signals by the OAEM. The different orders of magnitude of the differences in the up component emphasize the improvement by the OAEM. In the case of non-fixed ambiguities, differences of up to one meter can occur, whereas after the selection process the differences almost never exceed absolute values of 25mm during the whole observation period.
Nevertheless, the time series depicted in the right panel of Figure 5.14 in particular shows that the concept

of obstruction adaptive elevation masks should not be considered as an overall remedy for minimizing site-dependent effects. The systematic behavior of the time series indicates influences of far-field effects which are not captured by the selection process of the OAEM. While the long observation duration in the static case allows for a reduction of the influence by averaging, in the kinematic case a different minimization strategy is necessary. This aspect is taken up again in Section 5.4.

Scenario 2 – Sports field

The aim of this scenario is to evaluate whether the concept of obstruction adaptive elevation masks can be improved by integrating Fresnel zones into the detection and exclusion process. Therefore, both development stages of the satellite selection strategy are applied to the original observation data. First, all satellite signals that are identified by the OAEM approach without considering Fresnel zones (hereafter denoted as *stage 1*) are excluded. Additionally, for each satellite signal the Fresnel zones along the LOS vector are determined and compared to the classical OAEM, following the procedure described in Section 5.3.1 (hereafter denoted as *stage 2*). Afterwards, for both data sets an epochwise baseline solution is carried out and the differences to a static batch solution are computed and analyzed. Figure 5.15 shows the time series of the differences in the up-component for the two variants including a 3σ boundary, determined for each time series. For reasons of clarity, the curves are shown with an offset of +5 and -5cm respectively. In addition, Table 5.6 lists the minimal and maximal difference values and the root-mean-squared error (RMSE) of each time series. Furthermore, the percentage of outliers with respect to the 3σ boundary, as well as the percentage of epochs with fixed carrier-phase ambiguities are included in Table 5.6.

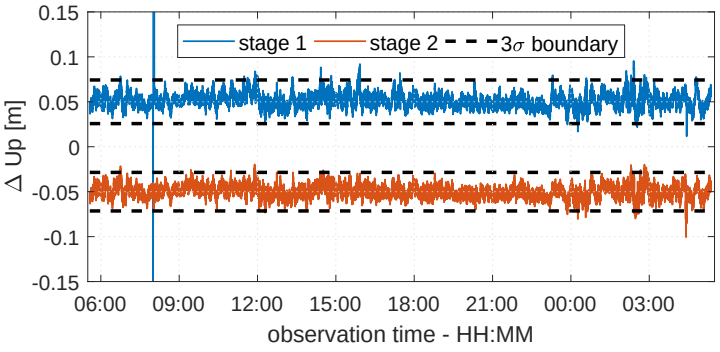


Figure 5.15: Differences of up-component to reference solution for data set modified by OAEM with (red, *stage 2*) and without (blue, *stage 1*) consideration of Fresnel zones. The black dashed line represents the 3σ boundary of each time series. For reasons of clarity, the time series are shown with an offset of +5 and -5cm respectively.

		OAEM approach	
		stage 1	*stage 2*
ΔUp [m]	min	-0.255	-0.050
	max	0.471	0.030
	RMSE	0.008	0.007
outlier		1.0%	0.5%
fixed ambiguities		97.2%	99.9%

Table 5.6: Comparison of minimal and maximal up-differences, RMSE values, percentage of outliers and epochs with fixed carrier-phase ambiguities resulting from different development stages of OAEM concept.

Compared to the results from scenario 1, it becomes obvious that the improvement, which is achieved by integrating the Fresnel zones, compared to the classical OAEM approach is smaller than the improvement that can be achieved by the use of OAEMs in general. The biggest improvement can be found in the percentage of epochs with fixed ambiguities, increasing from 97.2% to 99.9%, which in turn leads to a lower number of outliers and a reduction of the minimal and maximal difference values from -0.255m to -0.050m and from 0.471m to 0.030m, respectively. However, the RMSE values of both time series are similar, which indicates that possible signal distortions caused by a partial shadowing of the Fresnel zones do not necessarily have a significant impact on the accuracy of the position determination and can be compensated over a longer observation period. Although the improvement of this approach over the whole observation period is small, the reduced number of outliers and the increase of fixed ambiguities show that especially GNSS applications, where a precise positioning solution is needed in every observation epoch, like e.g. monitoring tasks, can benefit from the consideration of the theory on the propagation of electromagnetic waves.

5.3.3 OAEM performance in kinematic applications

In this dissertation the position determination of UAVs is used as an example for kinematic GNSS applications. For this reason, the quality of the satellite geometry in the context of waypoint planning of UAVs has already been addressed in Section 5.2.2. Consequently, the methods described here for minimizing NLOS reception and signal diffraction are also analyzed and evaluated with regard to UAV applications, whereby a transfer to other moving platforms, such as vehicle- and rail-bound systems or surveys vessels [Gräfe, 2008; Abdallah & Schwieger, 2015], is also possible. The main purpose of the investigations is to test the efficiency of the OAEM under a rapidly changing antenna environment and short observation durations on the one hand and a comparatively very slowly changing satellite constellation on the other hand.

Instead of the data from a real UAV flight, measurements from a test setup, consisting of a GPS antenna on a prism pole and a 360° prism mounted under the antenna, are used to assess the OAEM performance. This is due to the fact that this procedure enables controlled terrestrial reference measurements with a total station in stop&go mode. Since the total station measurements are only triggered during the stop phase, latency times between angle and distance measurements during the movement of the UAV do not have to be considered and the reference values can be clearly related to the actual antenna positions.
Obviously, this measurement procedure does not simulate a UAV flight fully realistic, since effects such as vibrations, electromagnetic disturbances or highly dynamic movements, which normally influence the observation data during a UAV flight, are not present here. Nevertheless, if appropriate countermeasures are applied, accuracies in the lower centimeter range can also be achieved during a flight under good GNSS conditions [Eling et al., 2015]. Consequently, the analysis of the positioning solutions obtained with this measurement procedure is well suited to assess the concept of obstruction adaptive elevation masks in kinematic applications and should therefore be considered as a preliminary investigation for the optimization of observation data from UAVs, or rather mobile mapping systems in general. This point is further discussed in Section 6.2.

A trajectory, consisting of 60 test points with different GPS measurement conditions that were occupied with the aforementioned setup is shown in Figure 5.16. The test environment is similar to the location used for the first scenario of the static tests described in Section 5.3.2.
Essentially, the procedure of determining the OAEM at each of the test points corresponds to the procedure described in Section 5.3.1. The difference to static applications mainly consists in the greater difficulty to guarantee the required accuracy of the initial position solution of about 20 centimeters also in the kinematic mode. For ambiguity fixed RTK positions, this can easily be achieved. Nevertheless, if the carrier-phase ambiguities cannot be fixed to integer values and only a float, or in the worst case only a code solution, is available, this can be different. If the GPS observations are provided by a multi sensor system, such as the UAVs addressed here, in these cases the initial antenna position should be determined by using the data of additional sensors of the mobile mapping platform, such as inertial sensors or visual odometry [Scaramuzza & Fraundorfer, 2011]. In the absence of additional sensors, an iterative approach for the determination of the OAEM, as explained in the following Section 5.3.4, could be an alternative.
For the test data set analyzed here, the accuracy of the initial baseline solution varies between 3cm and 13cm, and therefore, the OAEM procedure can be applied to the observation data at each test point without any restrictions. Afterwards, the modified data set is reprocessed and the coordinates are compared to the terrestrial reference coordinates. In Figure 5.17, the differences of the up component are shown exemplarily. Furthermore, the test points, where the determined OAEM detected and excluded satellite signals that are subject to NLOS reception or signal diffraction, are highlighted. Table 5.7 lists the RMS values of the coordinate differences and the percentage of epochs with fixed carrier-phase ambiguities.

At 21 of the 60 test points, satellite signals are identified as being subject to NLOS reception or signal diffraction by the determined OAEM. After the exclusion of the respective observations, the coordinate differences to the reference solution decrease significantly. As already demonstrated in the previous section, the selection process of the OAEM leads to an increase in the number of fixed ambiguities, in this case from 55% to 88%. Furthermore, the RMS of the differences in all three coordinate components decreases to values

[4] ©https://www.tim-online.nrw.de/tim-online2/, last accessed: 07.02.2019

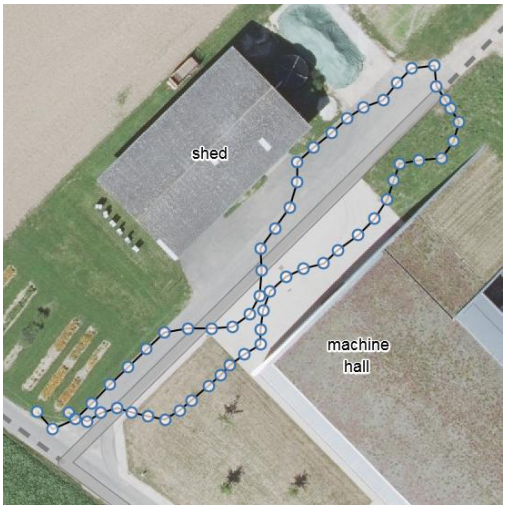


Figure 5.16: Aerial image[4](left) of the trajectory between a shed (left) a machine hall (right) for the kinematic OAEM test. The blue circles denote the test points on the trajectory.

		OAEM applied	
		Yes	*No*
RMS [m]	North	0.007	0.036
	East	0.008	0.025
	Up	0.008	0.045
fixed ambiguities		88%	55%

Table 5.7: RMS values of coordinate differences and percentage of epochs with fixed carrier-phase ambiguities before and after application of OAEM.

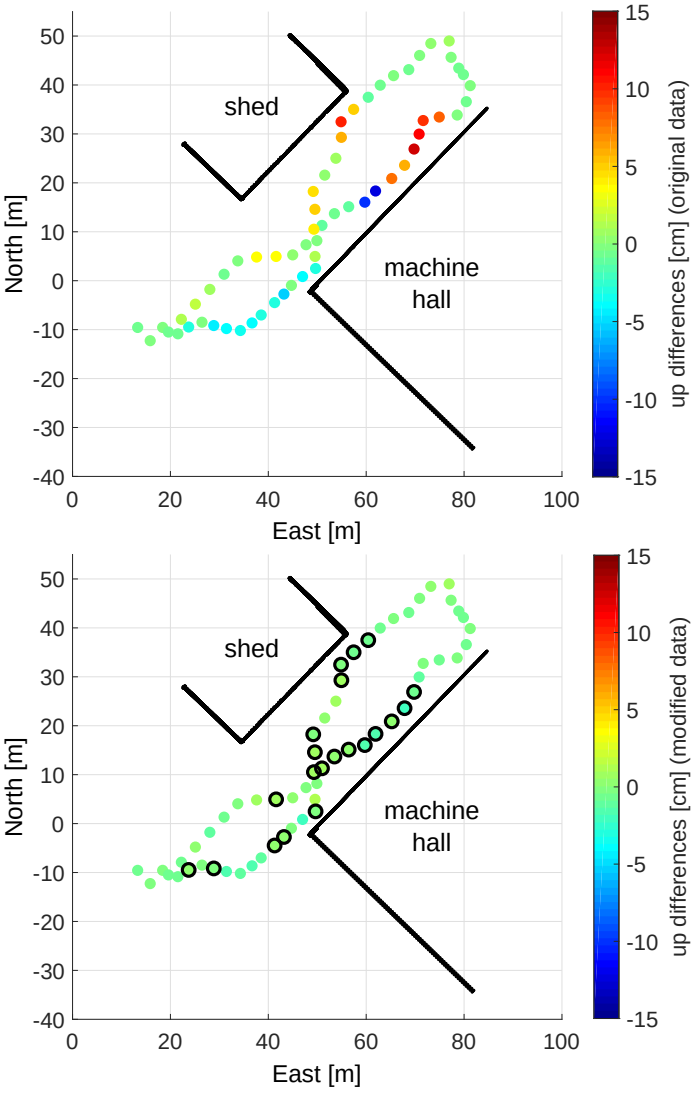


Figure 5.17: Differences of the up component to the terrestrial reference solution before (top) and after (bottom) the OAEM is applied at each test point. The black circles in the bottom panel highlight the test points, where satellite signals are excluded by the respective OAEM.

between 7 and 8 millimeters, whereas with the original observation data only values between 2.5 and 4.5 centimeters are obtained. For the up component shown in Figure 5.17, this corresponds to an improvement of about 82%. Considering the individual test points, the greatest improvements are achieved between the buildings. After selecting the unaffected satellite signals, the differences vary only between ±2.5cm, while after processing all available observations, maximum values of -18.5cm and 14.3cm occur.
It can be concluded that a careful signal selection based on the OAEM concept enables an efficient mitigation of NLOS reception and signal diffraction, also in the case of a moving antenna and the results indicate that applications, where an accurate kinematic positioning solution is essential, can profit from this mitigation technique. Nevertheless, the determination of an OAEM in the kinematic application case raises additional challenges which have not been fully addressed in the investigations described here. Especially the accuracy requirements for the initial position solution or the generation of the environment model with the onboard mapping sensors are particularly relevant aspects. These challenges are described and discussed again in Section 6.2.

5.3.4 OAEM determination without availabilty of georeferenced point clouds

In the previous investigations on obstruction adaptive elevation masks, the availability of a precisely georeferenced point cloud and a reasonably accurate initial position solution were assumed in both, static and kinematic applications. Under these conditions an effective minimization of the influences of NLOS reception and signal diffraction could be demonstrated in Publications B, C and E [Zimmermann et al., 2017a,b, 2019]. In order to utilize the concept of OAEMs even if neither a precise approximate solution of the antenna position nor a georeferenced environment model is available, an iterative approach is developed in Publication D [Zimmermann et al., 2018] in the context of the indirect georeferencing[5] of TLS-based point clouds.
The basic idea is to determine a first instance of the OAEM from a point cloud, georeferenced with transformation parameters that are derived from single point positioning (SPP) solutions of the ground control points (GCP). Afterwards, both, the georeferencing and the OAEM determination, are iteratively refined, based on selected carrier-phase observations and a relative positioning approach.

First, the application scenario and the corresponding data set are described, which serve as the bases for the development of the iterative algorithm. Subsequently, the algorithm is explained in detail and the main aspects of the analysis and evaluation of the iterative approach are highlighted. In particular, this includes the first iteration of the OAEM determination, as well as the influence of the algorithm on the accuracy of the GCP coordinates and the accuracy of the resulting point cloud.

Application scenario

A dense TLS-based point cloud and the GPS observations of six GCPs with different observation conditions in an urban scenario are the data bases for the development and the evaluation of the performance of the iterative algorithm. An aerial image including the distribution of GCPs in the test area is shown in Figure 5.18.



Figure 5.18: Aerial image[6] of test site for iterative georeferencing and OAEM determination algorithm. The triangles denote the position of the GCPs.

[5] In this context, indirect georeferencing describes the transformation of the point cloud from the local scanner frame to a global coordinate frame (WGS84/ITRF) by a 3D-Helmert transformation. The seven transformation parameters (three translations, three rotations and a scale parameter) are determined from ground control points (GCP) with known coordinates in both coordinate frames.

[6] ©https://maps.google.com/, last accessed: 18.02.2019

GPS observations were recorded at the six GCPs for several hours and afterwards the GCP coordinates were determined in a static baseline solution. Based on these coordinates, the transformation parameters between the local scanner system and the global coordinate system were determined and the point cloud was georeferenced. In the following, the results of this 'classical' approach for georeferencing a TLS point cloud are used as reference solution for the GCP coordinates as well as for the point cloud coordinates.
In the previous investigations to minimize NLOS reception and signal diffraction by means of OAEMs in static applications (Publication B, Zimmermann et al. [2017a]), long-term observations were processed and analyzed. In this case, also the influence of short observation durations shall be integrated into the analysis. Therefore, the long-term observations at the six GCPs are divided into 5 sessions (hereinafter referred to as S1 – S5) with an observation duration of 5 minutes. Furthermore, based on the preliminary investigation regarding the point cloud density (cf. Section 5.3.1), the point cloud is sampled down to a minimum point-to-point distance of 20cm. In particular for the iterative georeferencing and OAEM determination described below, this is expedient to keep the computational effort preferably low.

Iterative georeferencing and OAEM determination algorithm

As mentioned above, the algorithm obtains a first estimate of the OAEM from a coarsely georeferenced point cloud, which acts as a starting value for the iterative improvement of both components, i.e. the georeferencing and the OAEM determination. The determination of the first instance of the OAEM is one of the critical steps in this approach. Since only code observations are used for the determination of the GCP coordinates, large blunders in the observation data, as they can result from site-dependent effects, can also lead to large errors in the positioning solutions. Since these in turn are used to determine the transformation parameters between both frames, consequently, the blunders also directly influence the quality of the transformation parameters and thus also the accuracy of the OAEM. In the worst case, the corrupted transformation parameters can lead to a point cloud that is located above one or more GCP, after it is translated and rotated from the local to the global coordinate frame. As a result, the OAEM derived from this point cloud would identify all satellite observations as blocked and a coordinate estimation for these GCP is not possible anymore. Therefore, a strategy must be implemented that is designed to reduce the susceptibility or to increase the robustness of the navigation solution to faulty measurements.

Receiver Autonomous Integrity Monitoring (RAIM) methods provide this capability. The concept of RAIM was originally developed for increasing safety in aviation and has gained much attention especially in the field of urban positioning and navigation. In principle, RAIM techniques are based on a consistency check of redundant observations in order to test the reliability of the position determination and a variety of different RAIM techniques exist [Zhu et al., 2018]. In this thesis, a fault detection and exclusion (FDE) approach is used [Parkinson & Spilker, 1996]. Herein, after the SPP solution, the sum of squared observation residuals is compared to the respective quantile of the chi-square distribution in a global test. If the global test is rejected, an inconsistency of the measurements is detected and an outlier among the observations is assumed (fault detection). Afterwards, an observation subset testing is performed, by reducing the set of observations by one in all possible combinations and testing the SPP solution from each subset again. If one subset passes the global test, the outlier is detected and can be eliminated from the observation set (exclusion). If no subset passes the global test, the subset with the lowest test statistic is reduced by one observation in all combinations and tested again. This procedure is iterated until either a subset passes the global test or there are not enough observations available for another iteration. In this case, the SPP solution would be declared as unreliable.

The iterative algorithm outlined above is shown schematically in Figure 5.19, where $\mathbf{X}_s$ and $\hat{\mathbf{X}}^e$ denote the GCP coordinates in the respective coordinate frames[7], $\mathbf{t}_s^e$ and $\mathbf{R}_s^e$ are the transformation parameters under the assumption of equal scale in both coordinate frames and T is a threshold for checking the convergence of the algorithm, respectively.

[7]For reasons of clarity, the abbreviations s-frame and e-frame are occasionally used to denote the locale scanner frame (s-frame) and the global earth-centered-earth-fixed coordinate frame (e-frame).

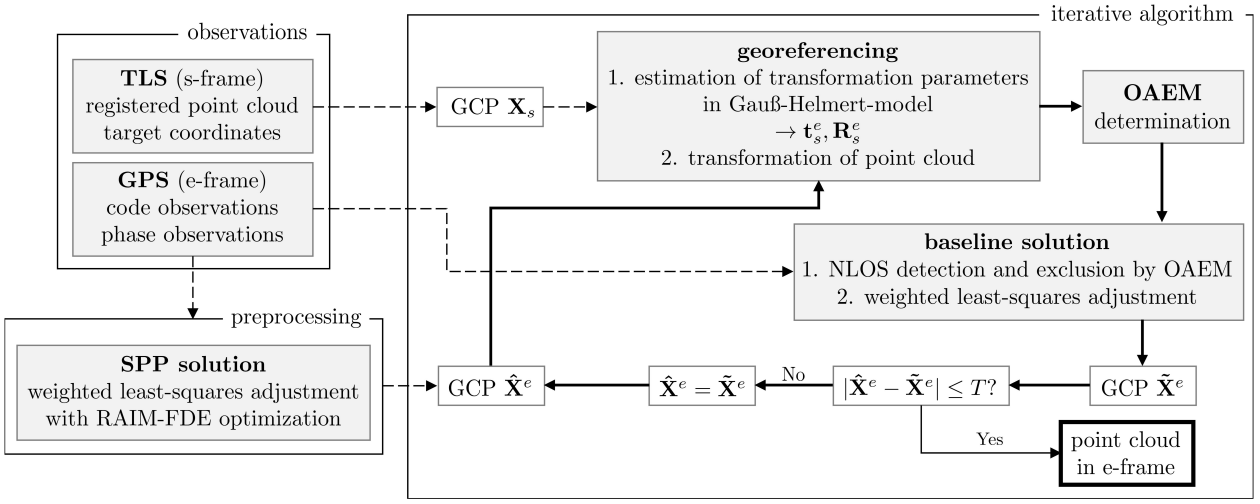


Figure 5.19: Schematic illustration of iterative georeferencing and OAEM determination algorithm.

The input of the algorithm are the GPS code and phase observations, as well as the TLS-based point cloud and the target coordinates in the scanner frame. The SPP solutions with the RAIM-FDE approach forms the preprocessing step of the algorithm and provides the approximate GCP coordinates in the global coordinate frame. In the georeferencing step, the transformation parameters are estimated in a Gauß-Helmert Model (GHM) and afterwards the point cloud is transformed from the s-frame to the e-frame. Based on this point cloud and the GCP coordinates, the OAEM is determined following the procedure described in Section 5.3.1. In the first iteration, i.e. the GCP coordinates originate from the preprocessing step, due to the high uncertainty of this solution, the adjustment step during the OAEM determination is omitted. Afterwards, the OAEM is used to select all satellite signals that are not identified as being subject to NLOS reception or signal diffraction. In the last step, the GCP coordinates are estimated in a baseline solution. If the difference to the values of the previous iteration exceeds a certain threshold, the GCP coordinates are used as new start values for the algorithm. Otherwise, the algorithm converged and the output provided are an accurately georeferenced point cloud and precise GCP coordinates.

Evaluation of RAIM-FDE approach in first iteration

Before the actual analysis of the iterative algorithm, the RAIM-FDE approach is evaluated first. Table 5.8 lists the horizontal (HPE) and vertical positioning errors (VPE) of GCP P6 for each of the 5 observation sessions exemplarily, whereby the HPE and VPE are computed as

$$\begin{aligned} HPE &= \sqrt{\Delta E^2 + \Delta N^2} \\ VPE &= \Delta U, \end{aligned} \tag{5.5}$$

where ΔE, ΔN and ΔU denote the respective coordinate differences after transformation into a local topocentric system. The results of the original data set are denoted as »Orig« and the results, after the RAIM-FDE approach is applied are denoted as »RAIM«.

It becomes obvious that the influence of blunders in the GPS code observations can largely be reduced by the RAIM-FDE approach. Especially the height component profits from the detection and exclusion of faulty measurements. The biggest improvements can be found in sessions S2 and S5, where the VPE is reduced by approximately 13 and 19 meters, and the HPE is reduced by 6.4m and 2.9m, respectively. Since the GCPs P4 and P5 provide comparable severe measurement conditions to those at P6 (cf. Figure 5.18), similar results are achieved at these GCPs (not shown here). In contrast, due to the medium to good observation conditions, no large errors occur in the observation data of the GCPs P1 to P3, and therefore the HPEs and VPEs are not

GCP-P6		observation session				
		S1	S2	S3	S4	S5
HPE [m]	Orig	1.5	6.8	2.0	3.0	3.6
	RAIM	1.2	0.4	2.9	0.8	0.7
VPE [m]	Orig	-3.7	-14.1	-5.5	-7.7	-22.2
	RAIM	-3.8	-1.0	-4.0	-1.7	-3.2

Table 5.8: Horizontal and vertical positioning errors of GCP P6 after processing the GPS observations with (RAIM) and without (Orig) RAIM-FDE approach. S1 – S5 denote the respective observation sessions of 5 minute duration.

influenced by the RAIM-FDE approach. Since the GCPs P4 to P6, which have considerably worse observation conditions than P1 to P3, are all located in the northern part of the test area, large errors in the coordinates can lead to a falsification of the transformation parameters and thus to the already described tilting of the point cloud. Consequently, by applying the RAIM-FDE approach, comparable coordinate accuracies can now be achieved at all GCPs, independent of the available observation conditions, and thus, a first reasonable approximation of the OAEM can be determined.

Assessment of influence on ground control point coordinates

Two criteria are used to assess the performance of the iterative algorithm: 1) the accuracy of the GCP coordinates with respect to long-term static baseline solution and 2) the point-to-point differences of the georeferenced point clouds. Similar to the evaluation of the RAIM-FDE approach, Table 5.9 lists the horizontal and vertical positioning errors of GCPs P4 and P6 exemplarily for all 5 observation sessions. The colored frames indicate if the carrier-phase ambiguities could be fixed to integer values (green) or if it is a float solution (orange). Furthermore, the processing results of the original data are labeled as »orig«, and »mod« denotes the results, where during the iterative processing a selection of signals affected by NLOS reception and signal diffraction was performed.

GCP			observation session				
			S1	S2	S3	S4	S5
P4	HPE [m]	orig	0.003	0.009	0.044	0.014	0.567
		mod	0.004	0.011	0.003	0.012	0.047
	VPE [m]	orig	0.020	0.000	0.476	0.036	0.066
		mod	0.018	0.015	-0.005	0.033	-0.075
P6	HPE [m]	orig	0.007	3.692	0.768	0.820	8.582
		mod	0.002	0.006	0.010	0.007	0.019
	VPE [m]	orig	-0.007	-8.508	-0.842	-3.114	-20.757
		mod	-0.007	0.006	0.004	0.016	0.012

Table 5.9: Horizontal and vertical positioning errors of GCPs P4 and P6 before (orig) and after (mod) iterative georeferencing and OAEM determination algorithm. S1 – S5 denote the respective observation sessions of 5 minute duration. The colored frames denote the type of ambiguity solution (float→orange, fixed→green).

The results shown in Table 5.9 demonstrate that the iterative approach enables the selection of uninfluenced satellite signals even without a precise approximate solution of the antenna position and without the availability of a georeferenced point cloud, and therefore, the accuracy of the position determination can be

significantly improved. Using the original observation data, in 2 of the 5 sessions in the case of P4, and in 4 of the 5 sessions in case of P6, the carrier-phase ambiguities could not successfully be fixed, and thus, in parts extremely high positioning errors occur. Contrarily, after three iterations of the algorithm, all ambiguities can be fixed and the HPE and VPE values seldom exceed a value of 2cm in all observation sessions. Solely in session S5, the differences reach higher values of 4.7 and -7.5 centimeters respectively, which can be explained by remaining far-field multipath effects, induced by the close-by glass facade in the surrounding of P4, that cannot be eliminated by the OAEM concept. Nevertheless, the significant improvement of the positional accuracy demonstrates that for this application case, the current prerequisites for a successful use of the OAEM concept (cf. Section 5.3.1) could be circumvented by the iterative approach and the potential of the OAEMs could be fully exploited.
In addition to the contribution to the goal of this dissertation, the development of methods to minimize site-dependent effects, these results also have a further economic relevance. Often, long-term observations are used to minimize site-dependent effects. This implies that for a simultaneous occupation of GCPs with GPS, the same number of receivers and antennas are required. If the GCPs are occupied consecutively, the required time increases accordingly. The developed approach can lead to an improvement in this aspect. Since it has been demonstrated that even with short observation durations, accuracies in the lower centimeter range can be achieved, the number of GCPs determined with GPS can be significantly increased, which results in both, time and cost reductions. Nevertheless, the short observation times have the consequence that far-field multipath cannot be reduced by averaging, which has already been discussed for the kinematically processed long-term observations in Section 5.3.2, or for the kinematic applications in Section 5.3.3. Thus, these effects remain as the dominant error source in the observation data and an alternative minimization strategy must be developed. This point will be addressed and discussed in the following Section 5.4.

Assessment of influence on TLS point cloud

For the analysis of the second assessment criterion, i.e. the accuracy of the point cloud coordinates, Figure 5.20 shows a top view of the point clouds resulting from sessions S3 and S5 exemplarily, where the points are colored according to the norm of the point-to-point differences.

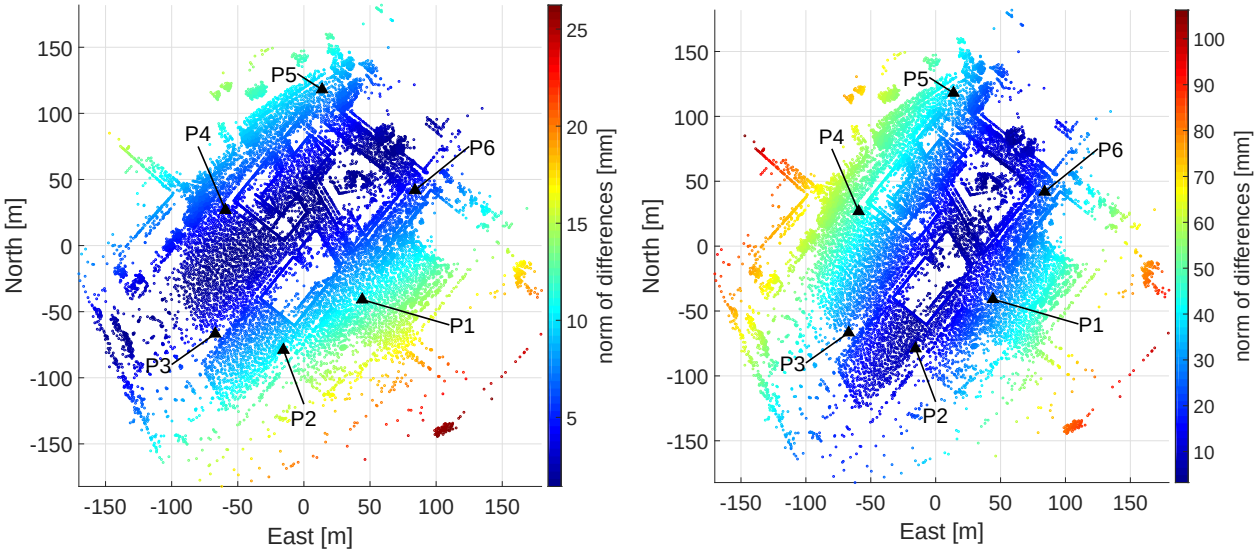


Figure 5.20: Top view on point cloud resulting from iterative georeferencing and OAEM determination algorithm, after processing the GPS observations from session S3 (left) and session S5 (right). The points are colored according to the norm of their point-to-point differences. The black triangles denote the position of the GCPs.

In the main area of interest, i.e. inside the polygon defined by the GCPs P1 – P6, the norm of the differences of the point cloud resulting from session S3 is constantly below 15 millimeters. Higher differences can mainly

be found in the north-western and south-eastern direction, increasing with the distance to the center of the GCPs. Hence, this can be related to the distribution of the ground control points and if additional GCPs would have been established at the upper left and lower right corner of the test area, it is very likely that the differences in these directions decrease to a similar level as in the inner part of the point cloud. Nevertheless, if the point cloud from session S5 is considered, the point-to-point differences in the same area of the point cloud reach values up to 4 to 5 centimeters, especially in the north-western direction. This results from the higher positioning errors of GCP P4 in this session (cf. Table 5.9) and emphasizes the aforementioned susceptibility of the position determination, and in turn, of the georeferencing to the remaining far-field multipath effects.

5.3.5 Summary

The mitigation of NLOS reception and signal diffraction is one of the core topics of this dissertation. The fundamental idea of the investigations and methodological developments described in the previous sections is the generation of elevation masks (OAEMs) that are adaptive to the obstructing objects in the respective antenna environment, and thus, enable a reliable detection of the satellite signals influenced by the effects. In particular, this is facilitated by exploiting the efficient and detailed acquisition of the antenna environment with terrestrial laser scanners. In contrast to many other mitigation strategies and based on the results of the investigations described in Section 5.2, the detected satellite signals are then directly excluded from the further position determination process.
The following 5 points summarize the main aspects of the methodological developments and empirical investigations on the topic of mitigating NLOS reception and signal diffraction using OAEMs.

1.) Accurately georeferenced TLS point clouds and an approximate antenna position solution were used to determine the obstruction adaptive elevation masks. After an adjustment step, taking into account the uncertainty of the antenna position by means of error propagation, the OAEMs were used to detect and exclude signals affected by NLOS reception and signal diffraction on the basis of a geometrical visible check of the LOS vector.

2.) The TLS point cloud density, necessary for a complete representation of the antenna environment, depends on the complexity of the obstruction situation and might need to be adapted individually. In this thesis, the empirical investigations using a point cloud of an urban scenario identified a minimal point-to-point distance of 20cm as a good compromise between accuracy and computational effort. Nevertheless, this value could be further decreased in the case of simple building structures, or, on the other hand, a higher point cloud density could be necessary, if finer details of the antenna environment should be represented by the respective OAEM. Since the number of points directly influences the computational effort, the type of OAEM determination, i.e. if a one-time determination, or a multiple or iterative determination is necessary, needs to be taken into account in this context.

3.) The visibility check of the LOS vector was extended by the concept of Fresnel zones. This enables the detection of signal distortions that can occur if the area where most of the signal energy is transferred is obstructed by objects in the antenna environment. Since especially the percentage of epochs, where the carrier-phase ambiguities could be fixed to integers, is improved to nearly 100%, in particular GNSS applications, where accurate coordinate solutions are needed in every observation epoch, and thus, outliers cannot be compensated by longer observation durations, could profit from this approach.

4.) The efficiency of the OAEM concept was tested in static and kinematic applications. In both cases, the positional accuracy could significantly be improved from the centimeter/decimeter to the millimeter level, even under severe GPS measurement conditions. One of the main reasons for the accuracy improvements is given by the substantial increase of the percentage of observation epochs with fixed carrier-phase ambiguities, e.g. from 56% to 100% in a static (cf. Table 5.5, page 52) and from 55% to 88% in a kinematic test (cf. Section 5.3.3).

5.) An iterative georeferencing and OAEM determination algorithm was developed that allows to exploit the concept of OAEMs without the availability of a beforehand accurately georeferenced point cloud and a reasonable approximate position solution. For this purpose, an initial instance of the OAEM is determined from a point cloud that has been georeferenced using code-solutions, optimized by RAIM techniques. Afterwards, obstructed satellites are identified and the respective carrier-phase observations are excluded from the subsequent baseline solution, providing improved antenna and GCP coordinates for the next iteration of the point cloud georeferencing and OAEM determination.

An important aspect that has not been fully considered in this dissertation is the determination of OAEMs on mobile mapping platforms. This point is taken up again in Section 6.2, where particularly the challenges arising from the use of onboard sensors are described and discussed.
Furthermore, it should be noted that, also it is not explicitly distinguished between NLOS reception on the one hand and signal reflection on the other hand, it can be assumed that the probability for signal diffraction is higher than for NLOS reception.

5.4 Analysis of far-field multipath under consideration of Fresnel zones

While satellite signals that are subject to NLOS reception and signal diffraction can effectively detected and excluded by means of OAEMs (cf. Section 5.3), an identification of signals influenced by multipath[8] is much more difficult to achieve. Since in this case the direct signal path is not blocked and therefore the direct and indirect signal are superimposed, a mere check of the satellite visibility is not sufficient. Although the effect on the observations is limited to a quarter of the respective signal wavelength, the investigations in Publications B – D [Zimmermann et al., 2017a,b, 2018] have shown that an adequate minimization strategy is necessary to achieve an accuracy in the millimeter to centimeter range, especially in kinematic applications or under short observation durations. With the aim of detecting affected satellite signals using a model of the antenna environment, it is therefore advisable to first identify the reflector surfaces that can effectively contribute to the reflection process on the basis of theoretical considerations. These regions are represented by the first Fresnel zones of the respective satellite signals, introduced in Section 3.3 and shown for a horizontal and an arbitrarily oriented reflector in Figure 3.7. In combination with the concept of OAEMs, this could enable the detection and exclusion of all satellite signals influenced by reflection or diffraction effects, whether with or without direct line of sight.

From a theoretical point of view, the occurrence of multipath is only possible under the two following prerequisites, which refer (i) to the smoothness and (ii) to the size and orientation of the reflecting surface:

(i) The reflecting surface needs to be smooth compared to the signal wavelength to cause specular reflection. This aspect can be assessed using the Rayleigh criterion (Equation (3.23), Section 3.3), which can easily be derived from a TLS point cloud of the antenna environment.
Although the Rayleigh criterion is often mentioned as a prerequisite for the occurrence of multipath effects, it is also emphasized that this criterion must not be interpreted as a sharp boundary [Hannah, 2001; Irsigler, 2008]. Rather, it should be taken into account that the probability of diffuse reflection increases if the Rayleigh criterion is exceeded. In the case of a horizontal reflector and the GPS-L1 frequency ($\lambda = 0.19$m), this already applies if the surface roughness exceeds 2 to 5cm for elevation angles between 40° and 90° (cf. Table 3.3, page 26). Since this is usually only found on surfaces such as asphalt roads or smooth concrete, it generally can be stated that, in the case of horizontal reflectors, satellite signals with lower elevation angles are mostly more susceptible to multipath effects.

(ii) The reflecting surface needs to be larger than the first Fresnel zone (cf. Section 3.3), so that a sufficient amount of energy is reflected, and the Fresnel zone needs to be completely located on the reflecting surface. Furthermore, from the geometrical optics follows that the reflecting surface needs to have a certain orientation with respect to the satellite and the antenna to enable the reflected signal to reach the antenna (cf. Figure 3.7).

Consequently, a detection and exclusion algorithm for mitigating multipath effects, similar to the OAEM concept (Publication B, Zimmermann et al. [2017a]), that strictly follows the two aforementioned aspects would only declare a satellite signal as being affected, if the respective Fresnel zone is fully located on any reflector in the antenna environment. However, if this prerequisite is rather a soft condition, as it is the case with the Rayleigh criterion, this has considerable consequences. Signals, whose Fresnel zones only partially overlap the reflecting surface, would be identified as non-critical, although they can also be affected by multipath effects. Hence, in particular this aspect, i.e. the relationship between size and location of the Fresnel zone and the occurrence of multipath, is empirically investigated in this section, since it has a decisive role in the identification of affected satellites.

[8] In this section, for the sake of simplicity, far-field multipath is only referred to as multipath. In this context, this term always refers explicitly to the superposition of the direct and reflected signal and is not understood as a collective term for multipath effects from the far- and near-field, as well as NLOS reception and signal diffraction, as it is often found in the related literature.

Design of field test

A suitable test environment is crucial for an empirical investigation and a sound analysis of the aforementioned aspect. Therefore, test measurements were carried out on a building roof, offering the following advantages. On the one hand, due to its exposed position, the roof is the only dominant reflector in the antenna environment and effects, such as NLOS reception or signal diffraction can be excluded. On the other hand, the roof is spatially limited by the roof edges, and thus, the question, whether multipath effects occur even though the Fresnel zones are not fully located on the reflector can explicitly be addressed for a horizontal reflector. In Figure 5.21, an aerial image and a colored point cloud of the building roof, as well as the Fresnel zones and reflection points of every hundredth observation epoch for one satellite and one antenna are shown.

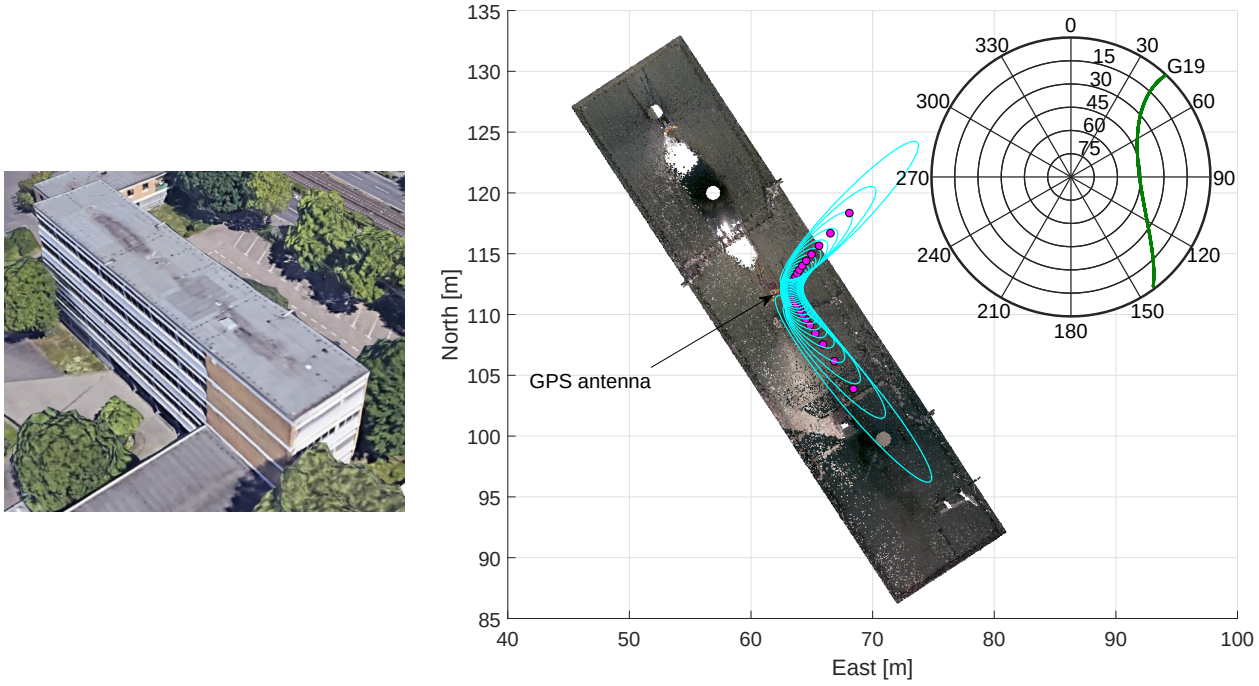


Figure 5.21: (Left) Aerial image of building roof[9]. (Right) Fresnel zones and reflection points (cyan ellipses and magenta dots) for the whole track of one satellite and one antenna on building roof in a topocentric coordinate system. The Fresnel zones are shown for every hundredth observation epoch. (Top right) Skyplot with satellite track, where the PRN number is located at the end of the track.

Figure 5.21 illustrates the basic idea of the empirical investigation. The satellite rises at an azimuth angle of 145° and passes the antenna in eastern direction before it sets at an azimuth of 45°. Due to the spatially limited and rectangular shape of the roof, the Fresnel zones are only completely located on the roof for certain directions and elevation angles. Thus, from a theoretical point of view, during these phases, i.e. a percentage of overlap of $P_{FZ} = 100\%$, the GPS observations should be affected by multipath. On the other hand, the negative influence on the observations should drop abruptly as soon as the overlap decreases, since from this point on, the theoretical prerequisites for the occurrence of multipath effects are no longer met.

Comparison of simulated and observed SNR time series for partially overlapping Fresnel zones

For an empirical analysis of the aforementioned aspect it is straightforward to compare the occurring effect with simulations, based on the theory of multipath, described in Section 3.2.2. From Equation (3.13), the amplitude of the compound multipath signal can be determined, if the satellite-antenna-reflector geometry,

[9] ©https://maps.google.com/, last accessed: 26.04.2019

the attenuation factor α of the reflection process and the amplitudes of the direct (A_D) and reflected signal (A_M) are known. Since both, A_M and A_D cannot directly be measured by the receiver, instead, the provided signal-to-noise ratio (SNR) can be used to derive the required quantities [Bilich, 2006]. Considering a SNR time series as shown in the left panel of Figure 5.22, in the case of ground reflections, the dominant trend of the time series (black line) refers to the amplitude of the direct signal component A_D, and the multipath signals are modulated on top of this trend. This is mainly due to the gain pattern of the antenna, which is usually designed in such a way that signals received at low or negative elevation angles are attenuated. Hence, it can be assumed that the amplitude of the reflected signal A_M is significantly smaller than A_D.

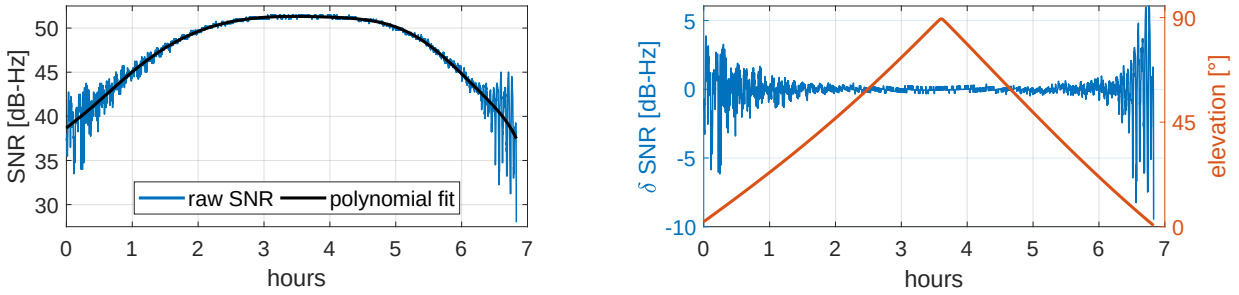


Figure 5.22: (Left) Original SNR time series (blue) and polynomial fit (black), representing the direct signal component. (Right) δSNR time series, representing the the amplitude of the reflected signal, after subtraction of the polynomial fit from the raw SNR time series. The red line denotes the respective satellite elevation.

After subtracting the trend (A_D) from the raw SNR time series, the δSNR time series (cf. right panel of Figure 5.22) represents the reflected signal component A_M and afterwards, the attenuation factor α of the reflection process, which represents the ratio between the direct and reflected amplitude [Bilich, 2006], can be determined by

$$\alpha = \frac{A_M}{A_D} = \frac{\delta SNR}{A_D}. \tag{5.6}$$

In Smyrnaios et al. [2013], an alternative approach for the determination of α is presented, where directly the antenna gain pattern and the reflection coefficients of the reflecting materials are used. However, since the gain patterns were not available for the antennas used in the following investigations, this approach was not pursued further and instead the values were derived directly from the SNR values as described above.

In Figure 5.23, the results of the comparison of the observed and simulated SNR time series are shown for the satellite track depicted in Figure 5.21.

The top panel of Figure 5.23 visually compares the observed and simulated δSNR time series. Furthermore, the percentage of overlap of Fresnel zone and reflector is shown. Between the solid red lines, both, the Fresnel zones and the reflection points are completely located on the roof ($P_{FZ} = 100\%$). The pink shaded areas bounded by the solid and dashed red lines represent the transition phases, where the reflection points and only parts of the Fresnel zones are located on the roof ($50\% \leq P_{FZ} < 100\%$). In the red shaded areas (left and right of the dashed red lines), the reflection point is not located on the roof and $P_{FZ} < 50\%$. For a numerical comparison of the observed and simulated values, in the lower panel of Figure 5.23, the correlation of both δSNR time series, determined for a sliding window of 15 minutes length, is shown. Furthermore, the observation periods where the Rayleigh criterion, is fulfilled are highlighted in grey and the borders of the three phases of P_{FZ} are denoted by the dashed and solid red lines. For the determination of the Rayleigh criterion, a plane is fitted to a TLS point cloud of the roof and the standard deviation of the residuals ($\sigma_{\Delta H} = 0.055$m) is used to compute the corresponding elevation angle following Equation (3.23), leading to 26° for the GPS-L1 carrier phase wavelength.

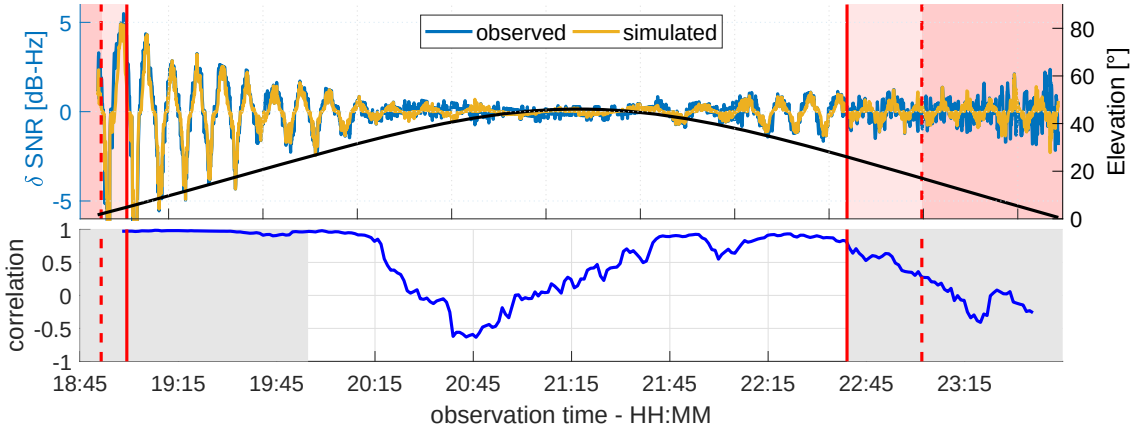


Figure 5.23: (Top) Observed (blue) and simulated (ocher) δSNR time series and respective satellite elevation (black line). (Bottom) Correlation between observed and simulated δSNR time series determined from a sliding window of 15 minutes length.

Considering the top panel of Figure 5.23, the simulated and observed δSNR time series show very good agreement for $P_{FZ} = 100\%$. This corresponds to the theoretical assumption that multipath will occur when the first Fresnel zones are completely located on the reflecting surface. The best agreement can be found for elevation angles lower than 30°. In relation to the Rayleigh criterion and the smoothness of the reflecting surface, above 26° the probability of a higher influence of diffuse reflections increases. Hence, the lower agreement between simulation and observation is reasonable. The correlations in this phase, depicted in the lower panel of Figure 5.23, confirm the visual analysis. During the rising phase of the satellite, the correlation is constantly above a value of 0.8, even beyond the period in which the Rayleigh criterion is met. Afterwards the correlation varies strongly until, during the setting phase of the satellite, the correlation rises again to a similar high value from 22.15pm on, i.e. before reaching the phase in which the criterion is fulfilled again. The fact that the correlation does not immediately drop at the borders between the grey and white areas confirms that the Rayleigh criterion cannot be interpreted as a sharp border between diffuse and specular reflection.
On the other hand, the simulated and observed δSNR values differ greatly when the reflection point is not located on the roof and P_{FZ} is smaller than 50%. In these phases, the variation in the observed δSNR time series is of more random nature, which corresponds to the multipath theory described in Section 3.2.2. Although Fresnel zones are not considered here, it is assumed that the reflection point is always on the reflector plane if multipath occurs. However, since the overlap between the Fresnel zones and the roof is always less than 50%, the Fresnel theory from Section 3.3 is also confirmed. Due to the short duration of this phase at the beginning of the observation period, only the correlation at the end of the observation period can be analyzed. Nevertheless, the correlation is very low and fluctuates around zero. Therefore, also in this case the visual analysis is confirmed.
The most interesting period of time is the transition phase ($50\% \leq P_{FZ} < 100\%$) between 18.50pm and 19.00pm, respectively 22.40pm and 23.00pm, represented by the pink shaded region, where the reflection points are still on the roof, but the Fresnel zones are only partially overlapping the reflector. In the rising phase of the satellite, a good agreement between simulation and observation can be found. Nevertheless, the transition phase is very short and due to the length of the sliding window, correlation values cannot provided for this period of time. Contrarily, during the transition phase in the right part of the time series, the correlation decreases slowly and does not drop immediately. This indicates that significant multipath effects can already occur during the transition phase.

It can be concluded that in contrast to the theoretical assumptions, multipath already can occur if the percentage of overlap between a Fresnel zone and a reflecting surface is above 50% and the reflection point of the satellite signal is located on the reflecting surface. Hence, a Fresnel zone that is completely located on the reflecting surface does not necessarily need to be fulfilled as a theoretical prerequisite for multipath

occurrence. In fact, the percentage of overlap between the Fresnel zone and reflector seems to be more important.

The findings from the investigations in Publication E [Zimmermann et al., 2019] represent an important first step towards a comprehensive selection of satellite signals which are influenced by site-dependent effects. The results clearly demonstrate that for a reliable detection of multipath effects a mere consideration of the reflection point is not sufficient and that instead the Fresnel zones in combination with the antenna environment have to be included in the decision making process. Since multipath effects were only analyzed for a single horizontal reflector, the necessary next steps for a more general consideration of the effect are outlined in Section 6.3.

The investigations presented in this section primarily focus on the correlation between observed and simulated SNR time series and are intended to analyze the occurrence of far-field multipath with respect to the size and location of the respective Fresnel zones, without considering the magnitude of the effect. Theoretically, this approach could also be used to simulate double-differenced carrier-phase residuals, similar to the investigations presented in Smyrnaios et al. [2013], and thus, could enable to analyze both, the occurrence and the magnitude of far-field multipath. However, since in this case two antennas are involved in the data processing, the carrier-phase residuals are influenced by multipath effects at both stations and in particular the relation of the multipath effects to the respective Fresnel zones can no longer be considered isolated for one antenna, as it is the case for SNR time series. For this reason, SNR time series were preferred for the investigations presented here. Nevertheless, in view of an advanced multipath detection and exclusion algorithm (cf. Section 6.3), simulating the expectable magnitude of the effect could be a further option to optimize the decision making process.

6. Further considerations

The investigations and developed methods for the analysis and minimization of site-dependent effects described in this dissertation rest on the basic principle of detection and exclusion, to the extent that the characteristics of the respective effects permit. Within the context of the investigations of the different effects, further questions arised due to the achieved results, or due to earlier restrictions and simplifications, which have not been considered in detail so far. This chapter is intended to address some of these questions and outline, based on the contributions made in this thesis, possible further investigations in the respective field.
Section 6.1 describes the integration of further GNSS into the developed methods and discusses their potential. Section 6.2 outlines the direct determination of OAEMs on mobile platforms and the challenges associated with the use of onboard sensors. Section 6.3 identifies the necessary steps towards an advanced selection algorithm based on Fresnel zones and Section 6.4 explains the need for further investigations in the field of antenna calibration parameters.

6.1 Integration of other GNSS

In this dissertation, it is demonstrated that the influence of NLOS reception and signal diffraction on the GNSS-based position determination can effectively be minimized by a solid detection and exclusion algorithm based on an environment model (e.g. cf. Section 5.3.2). Furthermore, the investigations on far-field multipath effects represent first steps in the same direction (cf. Section 5.4). However, so far only signals from the American GPS have been considered, although three further GNSS, the Russian GLONASS, the European Galileo and the Chinese BeiDou, are available and can be used for satellite-based positioning. At locations where a limited satellite visibility already prevails due to the existing antenna environment, the aforementioned strategy can lead to extremely unfavorable satellite constellations characterized by very high DOP values. In such cases, it is very likely that remaining systematics in the observations will have a considerable influence on the accuracy of the position determination. Furthermore, by extending the detection and exclusion strategy to include far-field multipath, the number of remaining satellite signals can decrease below the minimum required number of 4 satellites. Thus, the potential advantages of integrating further GNSS needs to be analyzed in this context. Figure 6.1 provides a first impression of a purely quantitative comparison of the satellite availability between GPS only and multi GNSS at a location with a significantly reduced satellite visibility in many directions. The satellite positions used for this purpose refer to 27 January 2019 at 15 minute intervals from 0:00am to 12:00am, and were obtained from the MGEX product archive[1]. The obstruction scenario corresponds to GCP P6 (cf. Figure 5.18 on page 56), analyzed in Section 5.3.4, and the respective OAEM is used to manipulate the satellite visibility according to the antenna environment.

Compared to the skyplots of the GPS only case (cf. left panel of Figure 6.1), a more dense coverage of the visible area bounded by the black line exists in the multi-GNSS case. In addition, the inclination of 64.8° of the GLONASS satellites, which is nearly 10° degrees higher than the inclination of the other GNSS satellites[2], reduces the area in the northern direction without available satellites.
The comparison of the number of satellites available at 15-minute intervals and the associated PDOP values shown in the right panel of Figure 6.1, further highlights the advantages already mentioned. On average 6 satellites are available when GPS is used only, i. e. only two more than at least are required for the position determination. In some periods (e.g. around 8:00am), the number of satellites is only 4 and near the end of the time series, it even drops below this value. As a result, especially the PDOP values in these areas increase significantly and are on average about 5.5 over the entire period, whereby it should be noted that this value is biased by the two peaks at the times mentioned. Nevertheless, if the other three GNSS are included, the

[1] http://mgex.igs.org/IGS_MGEX_Products.php
[2] In the case of BeiDou, the comparison of the satellite inclination refers to the medium-altitude earth orbit satellites of the BeiDou system [Teunissen & Montenbruck, 2017].

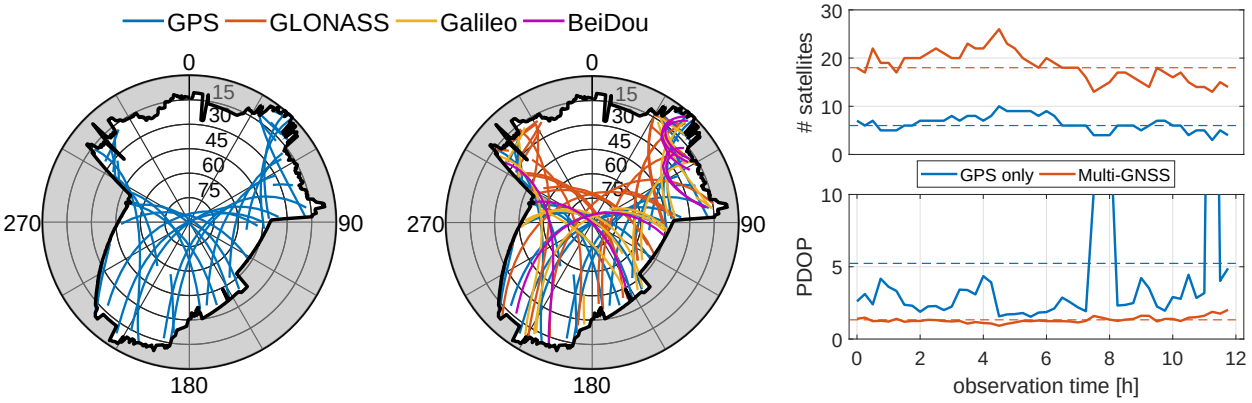


Figure 6.1: Skyplots for GPS only (left) and multi GNSS (middle) in case of an antenna position with limited satellite visibility. The black line in both skyplots represents the OAEM of the respective antenna location. Number of visible satellites (top right) and PDOP values (bottom right) in case of GPS only (blue line) and multi-GNSS (red line). The dashed lines in both panels denote the mean value of each curve. The satellite positions refer to 27 January 2019 at 15 minute intervals from 0:00am to 12:00am.

average number of available satellites increases by a factor of 3 to a value of 18 and the corresponding PDOP values are constantly below 2 with an average value of 1.3.

Since the limited satellite visibility is simulated using the OAEM of the respective antenna location, the remaining satellite signals are potentially only influenced by far-field multipath[3]. The extension of the selection process to include far-field multipath, as will be outlined in Section 6.3, should mainly cover non-horizontal reflectors. Since from a geometrical point of view, far-field multipath effects are only possible under a certain satellite antenna-reflector geometry, it can be assumed that not all satellites will be affected and that after the respective detection and exclusion, a sufficient number of satellites should be available for a precise position determination. However, this aspect needs to be analyzed and verified in further investigations.

6.2 OAEM determination on mobile platforms

Section 5.3.3 demonstrates that the transfer of the OAEM concept from static to kinematic applications, such as mobile mapping, is possible and an effective increase of the positioning accuracy can be achieved. However, certain assumptions and simplifications were made in the context of the described investigations and field tests. On the one hand, it was assumed that an accurately georeferenced point cloud is available at every position. On the other hand, instead of a real mobile mapping platform, a representative measurement setup was chosen to enable precise terrestrial reference measurements for the subsequent assessment of the results. If the OAEM concept should be integrated directly into the position and orientation determination of mobile platforms and the previously made assumptions are not applicable, several further steps are necessary. In this context, two options are conceivable: (i) the integration of 3D LOD models (level-of-detail) [Biljecki et al., 2014], due to the significantly lower requirements on storage capacity compared to 3D point clouds, or (ii) the generation of an environment model with the available onboard sensors.

If a georeferenced LOD model of the environment is available on the platform, a visibility check, as already described for waypoint planning in Zimmermann et al. [2017b], can be used to detect NLOS reception and signal diffraction. However, since vegetation is often not integrated in LOD models, possible resulting signal distortions cannot be detected, leading to a negative influence on the accuracy of the position determination [Zimmermann et al., 2017a]. Furthermore, the level of detail of an LOD model is not comparable to a point cloud. Consequently, similar to Section 5.3.1, further investigations are necessary to evaluate the potential of a comprehensive detection of NLOS reception and signal diffraction by LOD models.

[3]Near-field effects are neglected in this context, since no satellite selection is possible in this case (cf. Section 5.1).

Mobile mapping systems, such as the UAVs addressed in this thesis, are often equipped with a variety of different sensors. In addition to GNSS antennas and inertial measurement units, which are primarily used for the accurate georeferencing, various mapping sensors are usually available to capture the environment or a specific object [Kuhlmann & Klingbeil, 2016; Colomina & Molina, 2014]. These include various camera types, such as RGB cameras [Eling et al., 2015] or fisheye cameras [Schneider et al., 2016b], as well as small and lightweight laser scanners [Droeschel et al., 2014]. If these onboard sensors shall alternatively be used to derive an environment model, a distinction has to be made between an application in real-time and in postprocessing.
In the case of postprocessing, similar to the iterative method described in Zimmermann et al. [2018], a platform trajectory determined from the GNSS raw observations in combination with the image data can be used to compute a first approximation of the environment model in the form of a georeferenced point cloud. Subsequently, the antenna position and the environment model can be improved iteratively by applying the OAEM concept.
In real-time applications the requirements are substantially higher. The fully autonomous creation of a detailed environment model in real time is not a completely solved problem and was for example one of the main research areas of the scientific research project *Mapping on Demand*[4] (MoD). In the context of OAEMs, one of the main challenges is a preferably precise position determination even under difficult GNSS conditions. For this purpose it is indispensable to combine the data of other sensors, such as cameras, with the GNSS observations in an integrated positioning approach. For example in Schneider et al. [2016a], GPS raw observations and the image data of two fisheye stereo camera pairs are combined in an incremental bundle adjustment for a fast and effective position and orientation estimation.
A further challenge poses the creation of a first instance of the OAEM. Particularly the question arises how a sufficiently dense and complete point cloud can be provided in real time from the data of the onboard sensors. Since a reprocessing is necessary after the detection and exclusion of affected satellite signals, especially the real-time capability of such an approach has to be assessed.
As an alternative to images, the point clouds captured with an onboard laser scanner could also be utilized for the OAEM determination. In principle, the challenges here are similar to those described above.

A further option to determine OAEMs on mobile platforms, without the need for a complete 3D reconstruction of the antenna environment, is given by separating the visible and blocked areas of the environment directly in the camera images. Afterwards, the satellite positions, in terms of azimuth and elevation angle, could be projected into the image and classified as being visible or obstructed. Nevertheless, this approach requires a robust identification of the open-sky regions, independent from the weather and lighting conditions. Furthermore, the camera images must be georeferenced in the global coordinate system, which in turn requires a precise position determination using GNSS. Consequently, an iterative approach may also be necessary in this case.

6.3 Advanced satellite selection based on Fresnel zones

The analyses on far-field multipath effects carried out in this dissertation aimed at investigating the theoretically existing prerequisites for the occurrence of the effect. In order to assess the relationship between the size and location of the Fresnel zones with respect to the reflecting surface and the occurrence of far-field multipath, the investigations were restricted to a spatially limited and horizontal reflector. The main reason for this is the possibility of an isolated analysis of the signals reflected from the horizontal surface, i.e. there are no reflections from other surfaces, which mix with the ground-reflected signals. Nevertheless, the key finding, namely that far-field multipath can already occur although only half of the Fresnel zone is located on the reflecting surface, is transferable to vertical or arbitrarily oriented planar reflectors. If one assumes a vertical wall without the surrounding ground, the same situation applies as for a horizontal reflector, just rotated by 90° from the antennas point of view. Consequently, also for non-horizontal reflectors, a complete overlap of Fresnel zone and reflecting surface cannot be interpreted as a prerequisite for far-field multipath occurrence. Since in contrast to the deliberately chosen location in Zimmermann et al. [2019], the ground is

[4] http://www.ipb.uni-bonn.de/projects/MoD/, MoD – Mapping on Demand, DFG Research Unit FOR 1505

usually not spatially limited, a partially overlapping Fresnel zones rarely exist. Therefore, a detection and exclusion of affected signals is not expedient in these cases and instead common techniques to mitigate, or at least reduce far-field multipath induced by ground-reflections, such as antennas with ground planes or appropriate antenna gain patterns, should be preferred. Contrarily, partially overlapping Fresnel zones can frequently occur in the case of vertical reflectors. If the position and orientation of the reflecting surfaces is known, the Fresnel zones and the respective percentage of overlap can be determined analogously to horizontal reflectors. If the percentage exceeds 50%, the respective satellite signal can be excluded from the position estimation. Figure 6.2 schematically illustrates three examples for partially overlapping Fresnel zones on a vertical reflector.

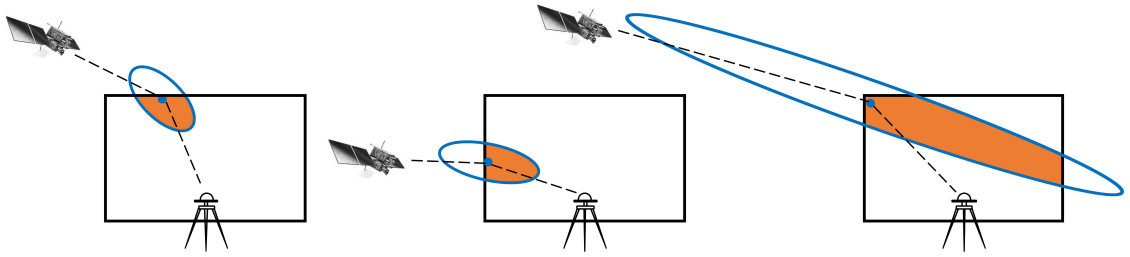


Figure 6.2: Schematic illustration of partially overlapping Fresnel zones (blue ellipses) in case of a vertical reflector (black rectangle). The blue dots denote the reflection point and the brown area represents the overlap between Fresnel zone and reflecting surface.

In the left panel of Figure 6.2, the Fresnel zone overlaps the lateral, and in the middle panel of Figure 6.2 the upper border of the vertical reflector. In both cases the overlap exceeds 50% and the reflection point is also located on the reflector. Thus, the reflected energy is sufficient to induce far-field multipath effects. In the right panel of Figure 6.2, a special case is shown to illustrate that for certain constellations, the overlap between the Fresnel zone and the reflecting surface can be lower than 50%, even though the reflection point is located on the reflector. Based on the results of Section 5.4, far-field multipath should not occur in this case and an exclusion of the respective signal is not necessary.
Especially in view of multi GNSS applications it can be assumed that after this kind of advanced satellite selection, the number of remaining signals will be sufficient for an accurate position determination. If NLOS reception or signal diffraction additionally are eliminated by the OAEM concept, the remaining signals can be considered as unaffected by site-dependent effects, apart from influences from the antenna near-field. Nevertheless, for a reliable and sound assessment of this procedure, further empirical investigations are necessary.

Besides the direct mitigation of far-field multipath, the findings of Section 5.4 can be integrated in the planning process for GNSS measurements. A conceivable approach could be to use the data of an almanac to determine satellite positions for a certain observation period and to forecast the expectable far-field multipath situation for one ore several site candidates using the concept of Fresnel zones in combination with an LOD model of the environment. This could enable the identification of both, the optimal observation period as well as the optimal antenna location.

6.4 Influence of antenna calibration parameters from different facilities

In GNSS-based positioning applications with highest accuracy requirements a careful consideration of antenna related effects, induced by the antenna near-field and individual phase center characteristics (PCO and PCV) is essential. In Section 5.1 it was demonstrated that these effects can largely be reduced during the double-differencing process by using individual antenna calibration parameters and an identical antenna setup. Particularly in already existing permanent reference station networks this is difficult to achieve, since

different antenna setups and antenna types are often used. For example at 508 sites of the global IGS network, 99 different combinations of antenna and radom types are in use (status as of December 2017)[Villiger & Dach, 2018].
Due to the rapid extension of the Galileo constellation in the last years, the efforts to integrate Galileo signals in permanent networks increase. For example, since 2018, in some federal states of Germany[5], Galileo is included in the high precision real-time service of the German satellite positioning service (SAPOS). A further example are current tests to use type mean calibrations derived from chamber calibrations in conjunction with calibration parameters of the Galileo satellites, disclosed in 2017 [GSA, 2017], to contribute to the scale determination of the next ITRF solution [Villiger et al., 2018, 2019].
In both cases, there is a need for providing and applying calibration parameters for the new Galileo signals, in particular for the E5, E5b and E6 frequencies. At the time of writing this dissertation, officially, these calibration parameters were solely provided by chamber calibrations and from robot calibrations by the Institut für Erdmessung (IfE[6]) [Kröger et al., 2019], whereby the main reason for the lack of robot calibrations from other facilities is the dependency on the status of the satellite constellation. Therefore, and in particular in view of other institutes providing the same data from robot calibrations in the near future, this will lead to a mixture of used calibration parameters from different facilities. As already described in Section 3.2.4, this is problematic, since the near-field situation present during the calibration process can influence the PCO and PCV parameters. Consequently, the calibration parameters provided by different facilities for the same antenna can differ from each other. In many of the recent investigations on the consistency of robot and chamber calibrations, the parameters are either directly compared (cf. e.g. [Becker et al., 2010; Aerts & Moore, 2013]), or the comparison is carried out in the coordinate domain, based on PPP solutions (cf. e.g. [Baire et al., 2014]). Nevertheless, since permanent networks usually process the observations with relative approaches, a comparison should also be performed for this kind of position determination. Furthermore, the calibration procedures, as well as the corresponding data evaluation are constantly improved and due to this ongoing optimization process, the validity of past investigations should be analyzed. First investigations in this direction are presented in Kersten et al. [2019], where the impact of antenna calibrations from different facilities on geodetic estimates in a network solution are analyzed.

In Table 6.1, first results of an initial test in the context of this dissertation are shown, where the positional differences induced by using calibration parameters from different facilities are compared for two baselines of different lengths (68km and 37km). For both baselines, a baseline solution is carried out using the ionosphere-free linear combination of dual-frequency GPS and GLONASS carrier-phase observations [Hofmann-Wellenhof et al., 2008]. Both baselines were observed in two sessions, whereby in session 1, at both ends of the baseline a Trimble Zephyr 2 antenna, and in session 2, a Leica AT504GG antenna was used. Robot calibrations from two facilities (R_A and R_B) were available for the Zephyr antenna and from one facility (R_A) for the Leica antenna. Chamber calibrations (C) were available for both antenna types. After the baseline solution, the differences to the solution where for both antennas chamber calibrations were used (C & C), were computed and transformed to a topocentric coordinate system.

Due to the low number of baselines and calibrations, a reliable assessment of the influence of calibration parameters from different facilities is not possible. However, the results indicate that further investigations are necessary in this context. In each case it is apparent that the influence on the height component is larger than on the east and north component, which only differ in the sub-millimeter range. If robot calibrations from the same facility are used, the difference to the solution with chamber calibrations are -1.9mm in the case of facility A and -3.2mm for facility B, respectively. In contrast, if the calibration parameters are mixed, the results for the two antenna types are highly different. While for both baselines the mixture of chamber and robot calibrations from facility A (C & R_A) leads to differences of approximately 1mm for the Zephyr antenna, the respective differences for the Leica antenna increase by a factor of nearly 10 to 9.1mm. This indicates that systematic effects occur during one, or both calibration procedures, which only become apparent if the calibration parameters of different facilities are used in conjunction. Furthermore, the ionosphere-free linear combination amplifies this effect.

[5] www.sapos-bw.de/trends.php
[6] www.ife.uni-hannover.de

baseline 68km		C & C	C & R_A	R_A & R_A	C & R_B	R_B & R_B
Zephyr 2	E [mm]	0.0	0.0	0.4	-0.6	-0.3
	N [mm]	0.0	-0.4	0.3	-0.2	0.5
	U [mm]	0.0	-1.1	-0.2	-2.5	-3.1
LEIAT504GG	E [mm]	0.0	-0.4	0.0	-	-
	N [mm]	0.0	0.1	0.0	-	-
	U [mm]	0.0	9.1	0.3	-	-

C...chamber calibration, R_A/R_B...robot calibration institute A/B

baseline 37km		C & C	C & R_A	R_A & R_A	C & R_B	R_B & R_B
Zephyr 2	E [mm]	0.0	0.0	0.4	-0.6	-0.3
	N [mm]	0.0	-0.3	0.3	-0.1	0.5
	U [mm]	0.0	-0.9	-1.9	-2.2	-3.2
LEIAT504GG	E [mm]	0.0	-0.3	0.0	-	-
	N [mm]	0.0	0.2	0.0	-	-
	U [mm]	0.0	9.1	0.1	-	-

Table 6.1: Positional differences induced by antenna calibration parameters from different facilities for two baselines with different lengths and different used antenna types. C denotes chamber calibrations and R_A/R_B denote robot calibrations from facilities A and B.

As already mentioned, the results presented here are not representative and do not allow for assessing the quality of the calibration parameters, neither from chamber, nor from robot calibrations. Instead, it should be emphasized that comparisons of calibration parameters from different facilities by means of extensive empirical investigations, like e.g. carried out in Kersten et al. [2019], are expedient and highly relevant, especially under the aforementioned aspects.

In the context of this dissertation, further reasons for the increasing relevance of the topic of antenna calibration can be identified. The developed methods for mitigating site-dependent effects enable to reduce the error budget of the satellite-based positioning to the millimeter level, even under severe GNSS measurement conditions. Thus, remaining uncertainties or systematic effects in the antenna calibration parameters may represent a significant, if not the dominant, remaining influence on the positional accuracy. Furthermore, based on the mitigation strategies described in this thesis, a clear separation and quantification of the single site-dependent effects may become possible. Hence, the influence of the antenna calibration parameters on the positional accuracy can be isolated, even under non-optimal conditions and without the need of specially designed experiments.

7. Conclusion and outlook

GNSS-satellite signals are subject to a variety of systematic errors along their path from the satellite to the receiver antenna. Nowadays, particularly the site-dependent parts of these error are still one of the accuracy-limiting factors for relative positioning applications with short baselines, since their dependency on the individual antenna environment deprives differential approaches of their effectiveness.

Common mitigation strategies are aiming at reducing the influence of the effects by appropriate weighting, filtering or correction of the affected signals. This dissertation takes an alternative approach, which focuses on the detection and exclusion of these signals based on antenna environment models and which in particular appears to be possible, due to the four GNSS and the associated large number of available satellites. Since site-dependent effects differ in their origin and their influence on satellite signals and the position estimation, and partially mutual dependencies between the single effects exist, the effects are investigated and analyzed separately with respect to the aforementioned alternative approach.

On the basis of these studies, and in line with the questions raised and the preliminary considerations made in the objectives, four main aspects can be emphasized that were addressed in different publications.

- **Minimization of antenna near-field effects by appropriate measurement strategies**
  The immediate vicinity of the GNSS antenna – the near-field – can change the antenna phase center characteristics and lead to an uncalibrated bias in the position estimation. Even though the individual phase center characteristics of an antenna can be determined via calibration, these parameters are actually only valid for the near-field situation present during the calibration process. If ferromagnetic materials are located inside the near-field of an antenna, the calibration parameters can change, and thus, negatively influence the position estimation. Since in this case, mainly the sensor itself, i.e. the GNSS antenna, is affected, a detection and exclusion strategy is not applicable. Nevertheless, by means of extensive empirical investigations, this dissertation demonstrates that during the measurements an nearly identical near-field situation can be established by a completely identical antenna setup. This enables to retrieve the effectiveness of differential positioning approaches, and thus, leads to a significant reduction of antenna near-field effects. In addition, recommendations for the antenna setup are made, which identify the usage of antenna spacers, intended to increase the distance between the antenna and the monumentation, as not expedient and potentially adverse. The results of the empirical investigations show that under good GNSS measurement conditions and by following this strategy, accuracies in the sub-millimeter range can be achieved for satellite-based positioning and baseline lengths of $\approx$ 1km.

- **Analysis of the influence of the satellite geometry and its consideration in kinematic applications**
  A mitigation approach that rests on detecting and excluding affected satellite signals, deliberately accepts a deterioration of the quality of the satellite geometry. This is one of the reasons, why common mitigation strategies avoid the exclusion of these signals and instead try to account for the systematic errors during the position estimation. In order to investigate the mere influence of a deteriorated satellite geometry, in this thesis, generic obstruction scenarios are simulated on otherwise perfectly GNSS observations and their impact on the positional accuracy is analyzed. It is demonstrated that this influence is marginal and actually only the combination with other accompanied systematic observation errors leads to a critical extend. Therefore, this dissertation emphasizes that in the case of a complete detection and exclusion of systematically influenced satellite signals, i.e. the best possible minimization of the observational uncertainty, the quality of the satellite geometry is of minor importance. As a further aspect, measures for the quality of the satellite constellation are used for developing a method for an optimized waypoint planning of mobile platforms. This method is based on a geometrical visibility check of the available satellite signals using a model of the antenna environment. By means of simulations on a real UAV trajectory, the potential of this optimization strategy is demonstrated for both, an a-priori waypoint planning and an adaption of the flight route during the UAV flight.

- **Mitigation of NLOS reception and signal diffraction in static and kinematic applications**
  Satellite signals can reach the antenna without a direct line of sight between the satellite and the antenna. If the signal is blocked by an obstacle in the antenna environment and only the reflected signal reaches the antenna, this is referred to as NLOS reception. Otherwise, if the satellite signal reaches the antenna after being diffracted at an edge of the obstacle and being bended into the shadowing zone, this is referred to as signal diffraction. Due to the special requirements regarding the satellite-reflector-antenna geometry in the case of NLOS reception, it can be assumed that diffraction effects occur more frequently than NLOS reception, at least during static GNSS applications. Nevertheless, since the underlying cause, i.e. the obstruction of the direct satellite signal, is identical in both cases, affected signals can be detected and excluded from the position estimation, if the antenna environment is known. In this dissertation, the current developments in the field of terrestrial measurements are taken into account and adaptive elevation masks are derived from georeferenced TLS point clouds, which represent the antenna environment including all obstruction sources. In this context, the influence of the point cloud density is analyzed and the uncertainty of the antenna position is considered by variance propagation. It is found that a minimal point-to-point distance of 20cm enables an accurate representation of the antenna environment and, at the same time, limits the computational effort. Furthermore, the concept of obstruction adaptive elevation masks (OAEM) is extended by Fresnel zones, whereby also signal distortions can be detected that potentially arise from an overlap of the obstruction sources and the region where most of the energy of the satellite signal is transmitted. The results of this investigations demonstrate that in both, static and kinematic applications, the detection and exclusion of NLOS reception and signal diffraction by OAEMs significantly improves the carrier-phase ambiguity solution (e.g. from 56% to 100% in a static and from 55% to 88% in a kinematic scenario) and enables an accurate position estimation at the millimeter level, even under severe GNSS measurement conditions. As a further aspect, an iterative algorithm is developed and assessed in this dissertation, which combines the concept of OAEMs and the georeferencing of TLS point clouds, without prior knowledge of a precise approximate positioning solution. It is demonstrated that the algorithm enables to circumvent current requirements for the location and observation duration of ground control points, and thus, can lead to a substantial increase of the time and cost efficiency.

- **Analysis of far-field multipath under consideration of Fresnel zones**
  The superimposition of direct and reflected satellite signals is denoted as far-field multipath and from a theoretical point of view, its occurrence depends on two prerequisites. First, the reflecting surface needs to be smooth enough and second, the Fresnel zone of the respective signal, that represents the region where most of the signals energy is reflected, needs to be completely located on the reflector. Consequently, in principal a detection and exclusion of affected signals can be performed by identifying combinations of signals and possible reflectors, where these prerequisites are fulfilled. Therefore, in this dissertation, the theoretical assumptions are analyzed and their validity is scrutinized by means of specially designed empirical investigations. By comparing simulated and observed SNR time series of measurements on a spatially limited and horizontal reflector it is shown that, in contradiction to the theoretical assumptions, an overlap of 50% between the Fresnel zone and the reflector is sufficient for the occurrence of far-field multipath. These results are highly relevant in two respects. On the on hand, they partially contradict the prevailing theoretical notions on the occurrence of far-field multipath, and thus, deepen the understanding of the propagation of electromagnetic waves. On the other hand, they form the basis for further algorithms that transfer the findings to arbitrarily oriented reflectors and advance the development of a detection and exclusion strategy for far-field multipath.

Although the effectiveness of the developed methods has already been demonstrated in different applications, the investigations triggered to develop a comprehensive mitigation strategy are not complete and several aspects have not been satisfactorily resolved yet. In addition to further improvements of the methods and the need for further investigations, particularly this implies the integration of other GNSS, as well as the transfer to mobile platforms.

The investigations carried out so far are based on the sole use of GPS signals. Since the methods developed here are used in particular under challenging GNSS conditions, usually a limited satellite availability already prevails due to obstructing objects in the antenna environment. Hence, the integration of further GNSS,

such as GLONASS, Galileo or BeiDou can reduce the probability that very unfavorable constellations arise due to the exclusion of satellite signals, or in the worst case, that no sufficient number of satellite signals is available at all.

The transfer to mobile platforms and in particular the implementation of the developed methods in real-time probably represents the greatest challenge. Especially the utilization of the additional onboard senors, such as cameras, inertial sensors or laser scanners, is essential for the determination of an environment model and the improvement of the positional accuracy. In this context, also the substitution of TLS point clouds by increasingly available LOD models has to be investigated and analyzed with regard to potential limitations.

The investigations on the occurrence of far-field multipath form the basis for the extension of the developed detection and exclusion techniques also for this effect. In this context, the next step is to transfer the findings to arbitrary reflecting surfaces. In addition to empirical investigations regarding the general applicability of such a procedure, the use of LOD models, for example for planning tasks, must also be analyzed in this context.

Another aspect that has not been addressed in its entirety is the near-field problem during the antenna calibration at different facilities. Since in already existing GNSS networks the use of calibration parameters of one facility may be difficult to realize, this influence has to be analyzed and quantified. In this context, representative investigations for the respective field of application are of particular interest.

Summarizing, the investigations carried out in this dissertation represent an important contribution for deepening the understanding of the individual site-dependent effects, and the methods developed for minimizing their influence on the satellite-based position determination considerably contribute to the expansion of the portfolio of available mitigation techniques. In addition, this dissertation adopts the trend described in Kuhlmann et al. [2014] from a point-based to an area-based object acquisition by revealing and exploiting the potential of a detailed and efficient acquisition of the antenna environment by TLS for minimizing and analyzing site-dependent effects in satellite-based positioning applications.

Impact of dissertation and consequences for an advanced measurement strategy

In many GNSS applications, site-dependent effects still represent one of the accuracy limiting factors. Thus, the findings of the investigations described in this dissertation and the developed mitigation methods can contribute to an advanced measurement strategy, with a special focus on minimizing the influence of site-dependent effects on the positional accuracy. Such measurement strategies are often formulated as guidelines that help the end user to optimally design the measurement campaign and the data processing, in order to achieve the accuracy requirements of the respective surveying task.

The results of the investigations related to the antenna near-field problem in Publication A [Zimmermann et al., 2016] are already partially included in guidelines for high-precision GNSS-based distance measurements [Astrua et al., 2017; Bauch et al., 2016] and for using antenna calibration parameters [Görres et al., 2018], where advice is given related to an optimized antenna setup and the correct application of the calibration parameters. By additionally integrating the developed methods for mitigating site-dependent effects, these guidelines can be extended to a comprehensive and advanced measurement strategy, which is outlined for two different types of surveying tasks in Table 7.1. The surveying tasks considered are:

1) **high-precision applications**, such as Continuously Operating Reference Station (CORS) networks or engineering geodesy tasks with accuracy requirements at the sub-millimeter to the lower millimeter level ($\sigma_{\mathrm{POS}} \leq 2 \ldots 3\mathrm{mm}$)
2) **medium-precision applications**, such as cadastral surveying with accuracy requirements at the centimeter level ($\sigma_{\mathrm{POS}} \approx 2 \ldots 4\mathrm{cm}$)

Under the assumption that far-field multipath effects can be mitigated by detecting and excluding affected satellite signals using the Fresnel zone concept, as outlined in Section 6.3, the proposed measurement strategy should considerably help to mitigate the influence of site-dependent effects on the positional accuracy. Nevertheless, since the developed methods represent an expansion of the portfolio of available mitigation techniques, a combination of different approaches could further enhance the effectiveness of this advanced measurement strategy.

	high-precision applications (e.g. CORS networks, engineering geodesy tasks) $\sigma_{\mathbf{POS}} \leq \mathbf{2}\ldots\mathbf{3mm}$	**medium-precision applications** (e.g. cadastral surveying) $\sigma_{\mathbf{POS}} \approx \mathbf{2}\ldots\mathbf{4cm}$
A	**mitigation of antenna near-field effects / antenna calibration errors** (Publication A, Zimmermann et al. [2016])	
	• geodetic grade antennas • individually calibrated by same institution • equal antenna setup at master and rover stations (tribrach, cable routing, etc.) • if antenna spacers are used $\leq$ 20cm	• rover-/smart-antenna • type-mean calibration sufficient (influence in the mm-range $\Rightarrow$ negligible)
B*	**antenna environment** (Publication D, Zimmermann et al. [2018])	
	• environment captured with TLS • point cloud georeferenced • point cloud density individually adapted	• environment available from LOD-model or captured with TLS • LOD-model or point cloud georeferenced • point cloud density $\approx$ 20cm
C**	**mitigation of NLOS reception and signal diffraction** (Publication B/C/E, Zimmermann et al. [2017a,b, 2019])	
	• Determination of OAEM from point cloud and approximate antenna position • Detection/Exclusion of affected satellite signals	• Determination of OAEM from LOD-model or point cloud and approximate antenna position • Detection/Exclusion of affected satellite signals
D	**mitigation of far-field multipath** (Publication E, Zimmermann et al. [2019])	
	• Identification of potential reflectors using Fresnel zones • Exclusion of affected satellite signals • long-term observation duration ($\geq 1\ldots2$h) for averaging remaining far-field multipath effects and minimizing observation noise	• Identification of potential reflectors using Fresnel zones • Exclusion of affected satellite signals
E	**positioning solution**	
	• static/kinematic baseline solution to master station or network solution	• averaged kinematic baseline solution to virtual reference station (VRS) for short observation duration ($\approx 10\ldots30$ seconds)

* $\rightarrow$ iterative approach of **B**–**E** if point cloud not georeferenced

** $\rightarrow$ iterative approach of **C**–**E** if approximate antenna position not accurate enough ($\sigma_{\mathrm{POS}} \leq$ 20cm)

Table 7.1: Advanced measurement strategy for mitigating site-dependent effects, exemplarily outlined for high-precision (left column) and medium-precision (right column) GNSS applications.

8. List of further publications

This chapter gives a chronological overview of further publications in which the author of this dissertation was involved. The publications listed here are either not directly related to this dissertation or are already covered by the relevant publications summarized in Chapter 4.

Peer-reviewed publications:

- Klingbeil, L., Eling, C., Zimmermann, F., & Kuhlmann, H. (2014a). Magnetic field sensor calibration for attitude determination. *Journal of Applied Geodesy*, 8(2), 97–108

Guidelines:

- Astrua, M., Pires, C., Pollinger, F., Poutanen, M., Saraiva, F., Schön, S., Tengen, D., Wallerand, J.-P., Zimmermann, F., Pellergrino, O., Niemeier, W., Marques, F., Bauch, A., Eusébio, L., Homann, C., Jokela, J., Kallio, U., Koivula, H., Kuhlmann, H., Lahtinen, S., & Zucco, M. (2017). Metrologie für die Entfernungsmessung mit GNSS und EDM. *DVW-Merkblatt*, 2017(9)
- Görres, B., Kersten, T., Schön, S., Zimmermann, F., & Wanninger, L. (2018). Berücksichtigung von Antennenkorrekturen bei GNSS-Anwendungen. *DVW-Merkblatt*, 2018(1)

Non peer-reviewed publications:

- Bauch, A., Eusébio, L., Kallio, U., Koivula, H., Lahtinen, S., Marques, F., Pellergrino, O., Pires, C., Pollinger, F., Poutanen, M., Saraiva, F., Schön, S., & Zimmermann, F. (2016). *Good practice guide for high accuracy global navigation satellite system based distance metrology.* Technical report, JRP SIB60 Surveying
- Pollinger, F., Bauch, A., Leute, J., Meiners-Hagen, K., Mildner, J., Guillory, J., Wallerand, J., Jokela, J., Kallio, U., Koivula, H., et al. (2016). JRP SIB60 Metrology for long distance surveying–a concise survey on major project results. In *Proceedings of the 3rd Joint International Symposium on Deformation Monitoring (JISDM), Vienna, Austria, March 30–April 1, 2016*
- Villiger, A., Prange, L., Dach, R., Zimmermann, F., Kuhlmann, H., & Jäggi, A. (2018). Consistency of antenna products in the MGEX environment. In *IGS Workshop 2018, Wuhan, China, October 29–November 02, 2018*
- Villiger, A., Prange, L., Dach, R., Zimmermann, F., Kuhlmann, H., & Jäggi, A. (2019). GNSS scale determination using chamber calibrated ground and space antenna pattern. In *Geophysical Research Abstracts, EGU General Assembly 2019, Vienna, Austria, April 7–12, 2019*, volume 21

List of Figures

3.1 Single and double difference . . . 15

3.2 Vector diagram for far-field multipath . . . 18

3.3 Far-field multipath . . . 18

3.4 NLOS reception and signal diffraction . . . 19

3.5 Field regions of an antenna . . . 20

3.6 Antenna model . . . 21

3.7 Fresnel zones . . . 23

3.8 Horizontal, vertical and arbitrarily oriented reflector for Fresnel zone analysis . . . 25

3.9 Fresnel zone for LOS transmission . . . 27

3.10 Radius of Fresnel zone for LOS transmission . . . 27

4.1 Content assignment of relevant publications . . . 29

5.1 Antenna near-field: Distance differences of all observed baselines . . . 37

5.2 Antenna near-field: Mean values of distance and height differences for equal antenna-spacer combinations . . . 37

5.3 Antenna near-field: Distance and height differences for equal and mixed spacer-antenna combinations. . . . 38

5.4 Satellite geometry: Generic satellite obstruction scenarios . . . 41

5.5 Satellite geometry: Number of satellites and PDOP values before and after obstruction simulation 42

5.6 Satellite geometry: Site-dependent PDOP values for trajectory of remotely controlled UAV flight. . . . 44

5.7 Satellite geometry: Site-dependent geometry map. . . . 44

5.8 NLOS reception/signal diffraction: Obstruction adaptive elevation mask and related aerial image and TLS point cloud . . . 45

5.9 NLOS reception/signal diffraction: Influence of point-to-point distance on OAEM success rate 47

5.10 NLOS reception/signal diffraction: OAEM concept – development stage 1 . . . 48

5.11 NLOS reception/signal diffraction: Diffraction identification using the Fresnel zones concept . 49

5.12 NLOS reception/signal diffraction: OAEM concept – development stage 2 . . . 50

5.13 NLOS reception/signal diffraction: Obstruction adaptive elevation mask and related aerial images for static GNSS applications . . . 51

5.14 NLOS reception/signal diffraction: Coordinate differences of epochwise baseline solution for static scenario 1 52

5.15 NLOS reception/signal diffraction: Differences of up-component to reference solution for data set modified by both development stages of the OAEM concept. 53

5.16 NLOS reception/signal diffraction: Aerial image of trajectory for kinematic OAEM test . . . 55

5.17 NLOS reception/signal diffraction: Differences of kinematic test before and after OAEM application 55

5.18 NLOS reception/signal diffraction: Aerial image of test site for iterative georeferencing and OAEM determination algorithm. 56

5.19 NLOS reception/signal diffraction: Schematic illustration of iterative georeferencing and OAEM determination algorithm 58

5.20 NLOS reception/signal diffraction: Norm of point-to-point differences to reference solution of point cloud resulting from iterative georeferencing and OAEM determination algorithm. . . . 60

5.21 Far-field multipath: Fresnel zones on building roof. 64

5.22 Far-field multipath: Original and detrended SNR time series. 65

5.23 Far-field multipath: Observed and simulated δSNR time series on building roof. 66

6.1 Skyplots and DOP values for single and multi GNSS. 70

6.2 Schematic illustration of partially overlapping Fresnel zones in case of a vertical reflector. . . 72

List of Tables

3.1 Boundary values of field regions of two different antenna types 21

3.2 Incidence angles of satellite signals and size of 1st Fresnel zones for horizontal, vertical and arbitrarily oriented reflector 25

3.3 Rayleigh criterion for different reflecting surfaces 26

5.1 Antenna near-field: Mean values and standard deviations of distance and height differences for equal and mixed antenna-spacer combinations. 38

5.2 Satellite geometry: Distance differences before and after obstruction simulation. 42

5.3 Satellite geometry: Height differences before and after obstruction simulation. 42

5.4 NLOS reception/signal diffraction: Coordinate differences for static scenario 1 52

5.5 NLOS reception/signal diffraction: Percentage of epochs with fixed ambiguities for static scenario 1. 52

5.6 NLOS reception/signal diffraction: Comparison of minimal and maximal up-differences resulting from different development stages of OAEM concept. 53

5.7 NLOS reception/signal diffraction: RMS values of coordinate differences and percentage of epochs with fixed carrier-phase ambiguities before and after application of OAEM. 55

5.8 NLOS reception/signal diffraction: Horizontal and vertical positioning errors of GCP P6 with and without RAIM-FDE algorithm. 59

5.9 NLOS reception/signal diffraction: Horizontal and vertical positioning errors of GCPs P4 and P6 before and after iterative georeferencing and OAEM determination algorithm. 59

6.1 Positional differences induced by different antenna calibration parameters. 74

7.1 Advanced measurement strategy for mitigating site-dependent effects 78

Abbreviations

ARP	antenna reference point
CORS	Continuously Operating Reference Station
DOP	dilution of precision
EDM	electronic distance measurement
FDE	fault detection and exclusion
FOC	fully operational constellation
GCP	ground control point
GDOP	geometrical DOP
GHM	Gauß-Helmert Model
GLONASS	Global'naya Navigatsionnaya Sputnikova Sistema
GNSS	Global Navigation Satellite System
GPS	Global Positioning System
HDOP	horizontal DOP
HPE	horizontal positioning error
IGS	International GNSS Service
ITRF	International Terrestrial Reference Frame
LOD	level-of-detail
LOS	line-of-sight
MoD	Mapping-on-Demand
NLOS	non-line-of-sight
OAEM	obstruction adaptive elevation mask
PCO	phase center offset
PCV	phase center variation
PDOP	positional DOP
PPP	precise point positioning
RAIM	receiver autonomous integrity monitoring
RMS	root-mean-square
RMSE	root-mean-squared error
RTK	real-time-kinematic
SA	selective availability

SAPOS satellite positioning service

SNR signal-to-noise ratio

SPP single point positioning

TDOP time DOP

TLS terrestrial laser scanner

UAV unmanned aerial vehicle

UERE user equivalent range error

VDOP vertical DOP

VPE vertical positioning error

VRS virtual reference station

References

Abdallah, A. & Schwieger, V. (2015). Kinematic Precise Point Positioning (PPP) Solution for Hydrographic Applications. In *FIG Congress 2015, Sofia, Bulgaria, 17–21 May 2015* (pp. 17–21).

Abraha, K. E., Teferle, F. N., Hunegnaw, A., & Dach, R. (2016). Impact of limited satellite visibility on estimates of vertical land movements. In *International Symposium on Earth and Environmental Sciences for Future Generations, Prague, Czech Republic, June 22–July 2, 2015* (pp. 269–276).

Aerts, W., Bruyninx, C., Defraigne, P., Vandenbosch, G. A., & Zeimetz, P. (2016). On the influence of RF absorbing material on the GNSS position. *GPS Solutions*, 20(1), 1–7.

Aerts, W. & Moore, M. (2013). *Comparison of Uni-Bonn and IGS08 antenna type means*. Report, IGS Antenna Working Group, https://kb.igs.org/hc/en-us/sections/200423428-Reports.

Agnew, D. C. & Larson, K. M. (2007). Finding the repeat times of the GPS constellation. *GPS Solutions*, 11(1), 71–76.

Ashkenazi, V. (2006). Geodesy and satellite navigation: A lighthearted look at a strange relationship. *Inside GNSS*, 1(3), 44–49.

Astrua, M., Pires, C., Pollinger, F., Poutanen, M., Saraiva, F., Schön, S., Tengen, D., Wallerand, J.-P., Zimmermann, F., Pellergrino, O., Niemeier, W., Marques, F., Bauch, A., Eusébio, L., Homann, C., Jokela, J., Kallio, U., Koivula, H., Kuhlmann, H., Lahtinen, S., & Zucco, M. (2017). Metrologie für die Entfernungsmessung mit GNSS und EDM. *DVW-Merkblatt*, 2017(9).

Baire, Q., Bruyninx, C., Legrand, J., Pottiaux, E., Aerts, W., Defraigne, P., Bergeot, N., & Chevalier, J. (2014). Influence of different GPS receiver antenna calibration models on geodetic positioning. *GPS Solutions*, 18(4), 529–539.

Balanis, C. A. (2005). *Antenna Theory: Analysis and Design*. New York, NY, USA: Wiley-Interscience.

Bauch, A., Eusébio, L., Kallio, U., Koivula, H., Lahtinen, S., Marques, F., Pellergrino, O., Pires, C., Pollinger, F., Poutanen, M., Saraiva, F., Schön, S., & Zimmermann, F. (2016). *Good practice guide for high accuracy global navigation satellite system based distance metrology*. Technical report, JRP SIB60 Surveying.

Becker, M., Zeimetz, P., & Schönemann, E. (2010). Anechoic chamber calibrations of phase center variations for new and existing GNSS signals and potential impacts in IGS processing. In *IGS Workshop, Newcastle upon Tyne, UK, June 28–July 1 2010*.

Bedford, L., Brown, N., & Walford, J. (2009). *Leica AR25*. White paper–Leica Geosystems AG, https://leica-geosystems.com/de-DE/products/gnss-reference-networks/antennas/leica-ar25.

Bilich, A. (2006). *Improving the precision and accuracy of geodetic GPS: applications to multipath and seismology*. PhD thesis, University of Colorado, Denver, CO, USA, August 2006.

Biljecki, F., Ledoux, H., Stoter, J., & Zhao, J. (2014). Formalisation of the level of detail in 3D city modelling. *Computers, Environment and Urban Systems*, 48, 1–15.

Biljecki, F., Stoter, J., Ledoux, H., Zlatanova, S., & Cöltekin, A. (2015). Applications of 3D City Models: State of the Art Review. *ISPRS International Journal of Geo-Information*, 4(4), 2842–2889.

Bock, Y. (1991). Continuous monitoring of crustal deformation. *GPS World*, 2(6), 40–47.

Böder, V., Menge, F., Seeber, G., Wübbena, G., & Schmitz, M. (2001). How to Deal With Station Dependent Errors–New Developments of the Absolute Field Calibration of PCV and Phase-Multipath With a Precise Robot. In *14th International Technical Meeting of the Satellite Division of the Institute of Navigation, ION GPS-2001, Salt Lake City, Utah, USA, September 11–14, 2001* (pp. 11–14).

Bourdeau, A., Sahmoudi, M., & Tourneret, J. (2012). Tight integration of GNSS and a 3D city model for robust positioning in urban canyons. In *Proceedings of the 25th International Technical Meeting of The Satellite Division of the Institute of Navigation (ION GNSS 2012), Nashville, TN, USA, September 17–21, 2012* (pp. 1263–1269).

Bradbury, J., Ziebart, M., Cross, P., Boulton, P., & Read, A. (2007). Code multipath modelling in the urban environment using large virtual reality city models: Determining the local environment. *The Journal of Navigation*, 60(1), 95–105.

Brunner, F. K., Hartinger, H., & Troyer, L. (1999). GPS signal diffraction modelling: the stochastic SIGMA-Δ model. *Journal of Geodesy*, 73(5), 259–267.

Bruyninx, C. (2004). The EUREF Permanent Network: a multi-disciplinary network serving surveyors as well as scientists. *GeoInformatics*, 7(5), 32–35.

Burghof, M. (2018). P40, BLK360 und RTC360 – ein Erfahrungsbericht. In *Terrestrisches Laserscanning 2018 (TLS 2018). DVW-Schriftenreihe.*

Choi, K., Bilich, A., Larson, K. M., & Axelrad, P. (2004). Modified sidereal filtering: Implications for high-rate GPS positioning. *Geophysical research letters*, 31(22).

Colomina, I. & Molina, P. (2014). Unmanned aerial systems for photogrammetry and remote sensing: A review. *ISPRS Journal of Photogrammetry and Remote Sensing*, 92, 79–97.

Dilßner, F. (2007). *Zum Einfluss des Antennenumfeldes auf die hochpräzise GNSS-Positionsbestimmung.* PhD thesis, Wissenschaftliche Arbeiten der Fachrichtung Geodäsie und Geoinformatik, Univ. Hannover, Nr. 271.

Dilßner, F., Seeber, G., Wübbena, G., & Schmitz, M. (2008). Impact of near-field effects on the GNSS position solution. In *Proceedings of the 21st International Technical Meeting of the Satellite Division of The Institute of Navigation (ION GNSS 2008), Savannah, GA, USA, September 16–19, 2008* (pp. 612–624).

Dong, D., Wang, M., Chen, W., Zeng, Z., Song, L., Zhang, Q., Cai, M., Cheng, Y., & Lv, J. (2016). Mitigation of multipath effect in GNSS short baseline positioning by the multipath hemispherical map. *Journal of Geodesy*, 90(3), 255–262.

Droeschel, D., Holz, D., & Behnke, S. (2014). Omnidirectional Perception for Lifgtweight MAVs using a Continously Rotating 3D Laser Scanner. *PFG - Photogrammetrie, Fernerkundung, Geoinformation*, 5, 451–464.

Eissfeller, B. (1997). *Ein dynamisches Fehlermodell für GPS Autokorrelationsempfänger*. Habilitation, Schriftenreihe Universität der Bundeswehr München, Band 55, München 1997.

Eling, C. (2016). *Entwicklung einer direkten Georeferenzierungseinheit zur Positions-und Orientierungsbestimmung leichter UAVs in Echtzeit.* PhD thesis, Deutsche Geodätische Komission, Reihe C, Nr. 788, München 2016.

Eling, C., Wieland, M., Hess, C., Klingbeil, L., & Kuhlmann, H. (2015). Development and Evaluation of a UAV based Mapping System for Remote Sensing and Surveying Applications. *ISPRS - International Archives of the Photogrammetry, Remote Sensing and Spatial Information Sciences*, XL-1/W4, 233–239.

Elósegui, P., Davis, J., Jaldehag, R., Johansson, J., Niell, A., & Shapiro, I. (1995). Geodesy using the Global Positioning System: The effects of signal scattering on estimates of site position. *Journal of Geophysical Research: Solid Earth*, 100(B6), 9921–9934.

Feldmann-Westendorff, U., Liebsch, G., Sacher, M., Müller, J., Jahn, C.-H., Klein, W., Liebig, A., & Westphal, K. (2016). Das Projekt zur Erneuerung des DHHN: Ein Meilenstein zur Realisierung des integrierten Raumbezugs in Deutschland. *zfv–Zeitschrift für Geodäsie, Geoinformation und Landmanagement*, 2016(5), 141.

Filippov, V., Tatarnicov, D., Ashjaee, J., Astakhov, A., & Sutiagin, I. (1998). The first dual-depth dual-frequency choke ring(for GPS L-band signal optimization in geodetic surveying systems). In *Proceedings of the 11th International Technical Meeting of the Satellite Division of The Institute of Navigation (ION GPS 1998), Nashville, TN, USA, September 15–18, 1998* (pp. 1035–1040).

Fuhrmann, T., Luo, X., Knöpfler, A., & Mayer, M. (2015). Generating statistically robust multipath stacking maps using congruent cells. *GPS Solutions*, 19(1), 83–92.

Gandor, F., Rehak, M., & Skaloud, J. (2015). Photogrammetric Mission Planner for RPAS. *International Archives of the Photogrammetry, Remote Sensing & Spatial Information Sciences*, XL-1/W4, 61–65.

Georgiadou, Y. & Kleusberg, A. (1988). On carrier signal multipath effects in relative GPS positioning. *Manuscripta geodaetica*, 13(3), 172–179.

Görres, B., Kersten, T., Schön, S., Zimmermann, F., & Wanninger, L. (2018). Berücksichtigung von Antennenkorrekturen bei GNSS-Anwendungen. *DVW-Merkblatt*, 2018(1).

Gräfe, G. (2008). Kinematic 3D laser scanning for road or railway construction surveys. In *Proceedings of the 1st International Conference on Machine Control & Guidance (MCG), Zurich, Switzerland, June 24–26, 2008* (pp. 24–26).

Groves, P. (2013). GNSS solutions: Multipath vs. NLOS signals. how does Non-Line-of-Sight reception differ from multipath interference. *Inside GNSS Magazine*, 8(6), 40–42.

Groves, P. (2016). It's Time for 3D Mapping–Aided GNSS. *Inside GNSS Magazine 2016*, (pp. 50–56).

Groves, P. D., Jiang, Z., Rudi, M., & Strode, P. (2013). A portfolio approach to NLOS and multipath mitigation in dense Urban areas. In *Proceedings of the 26th International Technical Meeting of The Satellite Division of the Institute of Navigation (ION GNSS+ 2013), Nashville, TN, USA, September 16–20, 2013* (pp. 3231–3247).

Groves, P. D., Jiang, Z., Wang, L., & Ziebart, M. K. (2012). Intelligent urban positioning using multi-constellation GNSS with 3D mapping and NLOS signal detection. In *Proceedings of the 25th International Technical Meeting of The Satellite Division of the Institute of Navigation (ION GNSS 2012), Nashville, TN, USA, September 17–21, 2012* (pp. 458–472).

GSA (2017). *Galileo satellite metadata*. European GNSS Service Center, Web document, https://www.gsc-europa.eu/support-to-developers/galileo-satellite-metadata, (last accessed: 18.02.2019).

Hannah, B. M. (2001). *Modelling and simulation of GPS multipath propagation*. PhD thesis, Queensland University of Technology, Brisbane, Australia, March 2001.

Hartinger, H. (2001). *Development of a continuous deformation monitoring system using GPS*. PhD thesis, Ingenieurgeodäsie – TU Graz, Shaker Verlag, Aachen.

Heister, H. (2012). Die neue Kalibrierbasis der UniBW München. *Allgemeine Vermessungs-Nachrichten, AVN*, 119(10), 336–343.

Heßelbarth, A. (2011). *Statische und kinematische GNSS-Auswertung mittels Precise Point Positioning (PPP)*. PhD thesis, Deutsche Geodätische Komission, Reihe C, Nr. 667, München 2011, München.

Heunecke, O. (2015). Die neue Neubiberger Pfeilerstrecke. *Zeitschrift für Geodäsie, Geoinformation und Landmanagement, ZFV*, 140(6), 357–364.

Hirt, C., Schmitz, M., Feldmann-Westendorff, U., Wübbena, G., Jahn, C.-H., & Seeber, G. (2011). Mutual validation of gnss height measurements and high-precision geometric-astronomical leveling. *GPS Solutions*, 15(2), 149–159.

Hofmann-Wellenhof, B., Lichtenegger, H., & Wasle, E. (2008). *GNSS–Global Navigation Satellite Systems: GPS, GLONASS, Galileo, and more*. Springer, Wien, NewYork, USA.

Holst, C. (2015). *Analyse der Konfiguration bei der Approximation ungleichmäßig abgetasteter Oberflächen auf Basis von Nivellements und terrestrischen Laserscans*. PhD thesis, Deutsche Geodätische Komission, Reihe C, Nr. 760, München 2015.

IGS (2015). *IGS Site Guidelines*. International GNSS Service, Web document, https://kb.igs.org/hc/en-us/articles/202011433-Current-IGS-Site-Guidelines (last accessed: 26.02.2019).

Irsigler, M. (2008). *Multipath propagation, mitigation and monitoring in the light of Galileo and the modernized GPS*. PhD thesis, Universität der Bundeswehr München, Fakultät für Luft- und Raumfahrttechnik, July 2008.

Jokela, J., Kallio, U., Koivula, H., Lahtinen, S., & Poutanen, M. (2016). FGI's contribution in the JRP SIB60 'Metrology for Long Distance Surveying'. In *Proceedings of the 3rd Joint International Symposium on Deformation Monitoring (JISDM), Vienna, Austria, March 30–April 1, 2016*.

Kallio, U., Koivula, H., Lahtinen, S., Nikkonen, V., & Poutanen, M. (2018). Validating and comparing GNSS antenna calibrations. *Journal of Geodesy*, 93(1), 1–18.

Kersten, T., Kröger, J., Breva, Y., & Schön, S. (2019). Deficiencies of phase centre models: Assessing the impact on geodetic parameters. In *Geophysical Research Abstracts, EGU General Assembly 2019, Vienna, Austria, April 7–12, 2019*, volume 21.

Kersten, T. & Schön, S. (2016). Receiver Antenna Phase Center Models and Their Impact on Geodetic Parameters. In *International Symposium on Earth and Environmental Sciences for Future Generations, Prague, Czech Republic, June 22–July 2, 2015* (pp. 253–259).

Kersten, T. & Schön, S. (2017). GNSS-Monitoring of Surface Displacements in Urban Environments. In *Lienhart, W: Ingenieurvermessung 17, Beiträge zum 18. Internationalen Ingenieurvermessungskurs, Graz, Austria* (pp. 415–426).: Wichmann, Berlin, Offenbach.

Klingbeil, L., Eling, C., Zimmermann, F., & Kuhlmann, H. (2014a). Magnetic field sensor calibration for attitude determination. *Journal of Applied Geodesy*, 8(2), 97–108.

Klingbeil, L., Nieuwenhuisen, M., Schneider, J., Eling, C., Droeschel, D., Holz, D., Läbe, T., Förstner, W., Behnke, S., & Kuhlmann, H. (2014b). Towards autonomous navigation of an UAV-based mobile mapping system. In *Proceedings of the 4th International Conference on Machine Control & Guidance (MCG), Braunschweig, Germany, March 19–20, 2014* (pp. 136–147).

Klostius, R., Wieser, A., & Brunner, F. K. (2006). Treatment of diffraction effects caused by mountain ridges. In *Proceedings of 3rd IAG/12th FIG Symposium, Baden, Austria, May 22–24, 2006.*

Knöpfler, A. (2015). *Korrektur stationsabhängiger Fehler bei GNSS.* PhD thesis, Schriftenreihe des Studiengangs Geodäsie und Geoinformatik / Karlsruher Institut für Technologie, Studiengang Geodäsie und Geoinformatik, KIT Scientific Publishing, Karlsruhe 2015.

Koch, K. (1999). *Parameter Estimation and Hypothesis Testing in Linear Models.* Springer, Berlin, Heidelberg, New York.

Kouba, J. & Héroux, P. (2001). Precise point positioning using IGS orbit and clock products. *GPS Solutions*, 5(2), 12–28.

Kröger, J., Breva, Y., Kersten, T., & Schön, S. (2019). Phase center corrections for new gnss-signals. In *Geophysical Research Abstracts, EGU General Assembly 2019, Vienna, Austria, April 7–12, 2019*, volume 21.

Kuhlmann, H. & Klingbeil, L. (2016). *Mobile Multisensorsysteme.* Freeden, W. & Rummel R. *(Eds.).* Handbuch der Geodäsie: 5 Bände, Springer Berlin Heidelberg, 1–36.

Kuhlmann, H., Schwieger, V., Wieser, A., & Niemeier, W. (2014). Engineering Geodesy-Definition and Core Competencies. *Journal of Applied Geodesy*, 8(4), 327–334.

Kunysz, W. et al. (2000). High performance GPS pinwheel antenna. In *Proceedings of the 13th International Technical Meeting of the Satellite Division of The Institute of Navigation (ION GPS 2000), Salt Lake City, UT, USA, September 19–22, 2000* (pp. 2506–2511).

Langley, R. B. (1999). Dilution of precision. *GPS world*, 10(5), 52–59.

Larson, K. M. & Nievinski, F. G. (2013). GPS snow sensing: results from the EarthScope Plate Boundary Observatory. *GPS Solutions*, 17(1), 41–52.

Lau, L. (2012). Comparison of measurement and position domain multipath filtering techniques with the repeatable GPS orbits for static antennas. *Survey Review*, 44(324), 9–16.

Lau, L. & Cross, P. (2006). A new signal-to-noise-ratio based stochastic model for GNSS high-precision carrier phase data processing algorithms in the presence of multipath errors. In *Proceedings of the 19th International Technical Meeting of the Satellite Division of the Institute of Navigation (ION GNSS 2006), Fort Worth, TX, USA, September 26–29, 2006* (pp. 276–285).

Lau, L. & Cross, P. (2007). Development and testing of a new ray-tracing approach to GNSS carrier-phase multipath modelling. *Journal of Geodesy*, 81(11), 713–732.

Leick, A., Rapoport, L., & Tatarnikov, D. (2015). *GPS satellite surveying.* John Wiley & Sons.

Meguro, J.-i., Murata, T., Takiguchi, J.-i., Amano, Y., & Hashizume, T. (2009). GPS multipath mitigation for urban area using omnidirectional infrared camera. *IEEE Transactions on Intelligent Transportation Systems*, 10(1), 22–30.

Misra, P. & Enge, P. (2001). *Global Positioning System - Signals, Measurements and Performance.* Lincoln, Massachusetts: Ganga-Jamuna Press.

Moreau, J., Ambellouis, S., & Ruichek, Y. (2017). Fisheye-based method for GPS localization improvement in unknown semi-obstructed areas. *Sensors*, 17(1), 119.

Nieuwenhuisen, M. & Behnke, S. (2015). 3D planning and trajectory optimization for real-time generation of smooth MAV trajectories. *2015 European*

Conference on Mobile Robots (ECMR 2015), Lincoln, UK, September 2–4, 2015, (pp. 1–7).

Parkinson, B. & Spilker, J. (1996). *The global positioning system: theory and applications, Volume II*. Number 164 in Progress in astronautics and aeronautics. American Institute of Aeronautics and Astronautics, Washington, DC.

Pollinger, F., Bauch, A., Leute, J., Meiners-Hagen, K., Mildner, J., Guillory, J., Wallerand, J., Jokela, J., Kallio, U., Koivula, H., et al. (2016). JRP SIB60 Metrology for long distance surveying–a concise survey on major project results. In *Proceedings of the 3rd Joint International Symposium on Deformation Monitoring (JISDM), Vienna, Austria, March 30–April 1, 2016*.

Rao, B. R., Kunysz, W., & McDonald, K. (2013). *GPS/GNSS Antennas*. Artech House.

Ray, J. K. & Cannon, M. E. (1999). Characterization of GPS carrier phase multipath. In *Proceedings of the 1999 National Technical Meeting of The Institute of Navigation, San Diego, CA, USA, January 25–27, 1999* (pp. 343–352).

Ray, J. K., Cannon, M. E., & Fenton, P. C. (1999). Mitigation of static carrier-phase multipath effects using multiple closely spaced antennas. *Journal of the Institute of Navigation*, 46(3), 193–201.

Rizos, C. (2002). Network RTK research and implementation: A geodetic perspective. *Journal of Global Positioning Systems*, 1(2), 144–150.

Rost, C. (2011). *Phasenmehrwegereduzierung basierend auf Signalqualitätsmessungen geodätischer GNSS-Empfänger*. PhD thesis, Technische Universität Dresden, Fakultät Forst-, Geo- und Hydrowissenschaften, Dresden, Germany, July 2011.

Santerre, R. (1991). Impact of GPS satellite sky distribution. *manuscripta geodaetica*, 16(1), 28–53.

Santerre, R., Geiger, A., & Banville, S. (2017). Geometry of GPS dilution of precision: revisited. *GPS Solutions*, 21(4), 1747–1763.

Scaramuzza, D. & Fraundorfer, F. (2011). Visual odometry [tutorial]. *IEEE robotics & automation magazine*, 18(4), 80–92.

Schmitz, M., Wübbena, G., & Boettcher, G. (2004). *Near Field Effects of a Car Roof on TPSHIPER-PLUS Phase Variations*. Geo++ White Paper, http://www.geopp.de/publications-by-geo/.

Schneider, J., Eling, C., Klingbeil, L., Kuhlmann, H., Förstner, W., & Stachniss, C. (2016a). Fast and Effective Online Pose Estimation and Mapping for UAVs. In *Proceedings of the IEEE International Conference on Robotics & Automation (ICRA), Stockholm, Sweden, May 16–21, 2016* (pp. 4784–4791).

Schneider, J., Stachniss, C., & Förstner, W. (2016b). On the Accuracy of Dense Fisheye Stereo. *IEEE Robotics and Automation Letters (RA-L) and IEEE International Conference on Robotics & Automation (ICRA), Stockholm, Sweden, May 16–21, 2016*, 1(1), 227–234.

Schön, S. & Kersten, T. (2013). On adequate Comparisons of Antenna Phase Center Variations. In *American Geophysical Union, Annual Fall Meeting, San Francisco, CA, USA, December 9–13, 2013*.

Seeber, G. (2003). *Satellite geodesy: foundations, methods, and applications*. Walter de Gruyter, Berlin, Boston.

SMBI.NRW (2017). *Erhebung der Geobasisdaten des amtlichen Vermessungswesens in Nordrhein-Westfalen - Erhebungserlass (ErhE)*. Ministerialblatt (MBI.NRW), Ausgabe 2017, Nr. 29, 05.10.2017, pp. 845–890, https://recht.nrw.de/lmi/owa/.

Smyrnaios, M., Schön, S., & Nicolás, M. L. (2013). Multipath Propagation, Characterization and Modeling in GNSS. In *Geodetic Sciences-Observations, Modeling and Applications*. Shuanggen Jin, IntechOpen.

Strode, P. R. & Groves, P. D. (2016). GNSS multipath detection using three-frequency signal-to-noise measurements. *GPS Solutions*, 20(3), 399–412.

Teunissen, P. & Montenbruck, O. (2017). *Springer handbook of global navigation satellite systems*. Springer, Wien, New York.

Verhagen, S. & Teunissen, P. J. (2006). New global navigation satellite system ambiguity resolution method compared to existing approaches. *Journal of Guidance, Control, and Dynamics*, 29(4), 981–991.

Villiger, A. & Dach, R. (2018). *IGS Technical Report 2017*. Technical report, International GNSS Service (IGS), https://kb.igs.org/hc/en-us/articles/360004995512-Technical-Report-2017.

Villiger, A., Prange, L., Dach, R., Zimmermann, F., Kuhlmann, H., & Jäggi, A. (2018). Consistency of antenna products in the MGEX environment. In *IGS Workshop 2018, Wuhan, China, October 29–November 02, 2018*.

Villiger, A., Prange, L., Dach, R., Zimmermann, F., Kuhlmann, H., & Jäggi, A. (2019). GNSS scale determination using chamber calibrated ground and space antenna pattern. In *Geophysical Research Abstracts, EGU General Assembly 2019, Vienna, Austria, April 7–12, 2019*, volume 21.

Vogel, H. & Gerthsen, C. (2013). *Gerthsen Physik*. Springer-Lehrbuch. Springer Berlin Heidelberg.

Wang, L., Groves, P. D., & Ziebart, M. K. (2013). GNSS shadow matching: Improving urban positioning accuracy using a 3D city model with optimized visibility scoring scheme. *Journal of the Institute of Navigation*, 60(3), 195–207.

Wanninger, L. (2006). Netz-RTK. In *GPS und Galileo – Methoden, Lösungen und neueste Entwicklungen; Beiträge zum 66. DVW-Seminar, Darmstadt, Germany, February 21–22, 2006* (pp. 59–69).

Wieser, A. (2002). *Robust and fuzzy techniques for parameter estimation and quality assessment in GPS*. PhD thesis, Ingenieurgeodäsie – TU Graz, Shaker Verlag, Aachen.

Wübbena, G., Bagge, A., Boettcher, G., Schmitz, M., & Andree, P. (2001). Permanent object monitoring with GPS with 1 millimeter accuracy. In *Proceedings of the 14th International Technical Meeting of the Satellite Division of The Institute of Navigation (ION GPS 2001), Salt Lake City, UT, USA, September 11–14, 2001* (pp. 1000–1008).

Wübbena, G., Schmitz, M., & Boettcher, G. (2006). Near-field effects on gnss sites: analysis using absolute robot calibrations and procedures to determine corrections. In *IGS Workshop 2006, Darmstadt, Germany, May 8–12, 2006*.

Wübbena, G., Schmitz, M., Menge, F., Böder, V., & Seeber, G. (2000). Automated absolute field calibration of GPS antennas in real-time. In *Proceedings of the 13th International Technical Meeting of the Satellite Division of The Institute of Navigation (ION GPS 2000), Salt Lake City, UT, USA, September 19–22, 2000* (pp. 2512–2522).

Zeimetz, P. (2010). *Zur Entwicklung und Bewertung der absoluten GNSS-Antennenkalibrierung im HF-Labor*. PhD thesis, Deutsche Geodätische Komission, Reihe C, Nr. 682, München 2012.

Zeimetz, P. & Kuhlmann, H. (2008). On the accuracy of absolute GNSS antenna calibration and the conception of a new anechoic chamber. In *Proceedings of the FIG Working Week, Stockholm, Sweden, June 14–19, 2008*.

Zhang, L. (2016). *Qualitätssteigerung von Low-Cost-GPS Zeitreihen für Monitoring Applikationen durch zeitlich-räumliche Korrelationsanalyse*. PhD thesis, Deutsche Geodätische Komission, Reihe C, Nr. 776, München 2016.

Zhang, L. & Schwieger, V. (2016). Improving the Quality of Low-Cost GPS Receiver Data for Monitoring Using Spatial Correlations. *Journal of Applied Geodesy*, 10(2), 119–129.

Zhang, L. & Schwieger, V. (2017). Investigation of a L1-optimized choke ring ground plane for a low-cost GPS receiver-system. *Journal of Applied Geodesy*, 12(1), 55–64.

Zhu, N., Marais, J., Betaille, D., & Berbineau, M. (2018). GNSS Position Integrity in Urban Environments: A Review of Literature. *IEEE Transactions on Intelligent Transportation Systems*, 19(9), 2762–2778.

Zimmermann, F., Eling, C., & Kuhlmann, H. (2016). Investigations on the Influence of Antenna Near-field Effects and Satellite Obstruction on the Uncertainty of GNSS-based Distance Measurements. *Journal of Applied Geodesy*, 10(1), 53–60.

Zimmermann, F., Eling, C., & Kuhlmann, H. (2017a). Empirical assessment of obstruction adaptive elevation masks to mitigate site-dependent effects. *GPS Solutions*, 21(4), 1695–1706.

Zimmermann, F., Eling, C., Klingbeil, L., & Kuhlmann, H. (2017b). Precise Positioning of UAVs–Dealing with challenging RTK-GPS measurement conditions during automated UAV flights. *ISPRS Annals of Photogrammetry, Remote Sensing & Spatial Information Sciences*, IV-2/W3, 95–102.

Zimmermann, F., Holst, C., Klingbeil, L., & Kuhlmann, H. (2018). Accurate georeferencing of TLS point clouds with short GNSS observation durations even under challenging measurement conditions. *Journal of Applied Geodesy*, 12(4), 289–301.

Zimmermann, F., Schmitz, B., Klingbeil, L., & Kuhlmann, H. (2019). GPS Multipath Analysis using Fresnel Zones. *Sensors*, 19(1), 25.

Zumberge, J., Heflin, M., Jefferson, D., Watkins, M., & Webb, F. H. (1997). Precise point positioning for the efficient and robust analysis of GPS data from large networks. *Journal of geophysical research: solid earth*, 102(B3), 5005–5017.

In der Schriftenreihe des Instituts für Geodäsie und Geoinformation
der Rheinischen Friedrich-Wilhelms-Universität Bonn sind erschienen:

2699-6685 (Online)

Heft 60 2020 — Florian Zimmermann
Analysis and mitigation of site-dependent effects in static and kinematic GNSS applications

---

ISSN 1864-1113

Heft 59 2018 — Sebastian Halsig
Atmospheric refraction and turbulence in VLBI data analysis

Heft 58 2017 — Sebastian Alexander Kropp
Hochwasserrisiko und Immobilienwerte

Heft 57 2017 — Sujit Kumar Sikder
Exploring Urban Structure to Approach Energy Optimization

Heft 56 2017 — Asad Asadzadeh
Conceptualizing the concept of disaster resilience: a hybrid approach in the context of earthquake hazard

Heft 55 2017 — Stefan Paulus
Potentiale von Laserscannern zur Phänotypisierung von Pflanzen für den Einsatz im Hochdurchsatz-Screening

Heft 54 2017 — Proceedings of the First International Workshop on VLBI Observations of Near-field Targets

Heft 53 2016 — Christian Eling
Entwicklung einer direkten Georeferenzierungseinheit zur Positions- und Orientierungsbestimmung leichter UAVs in Echtzeit

Heft 52 2016 — Maike Schumacher
Methods for assimilating remotely-sensed water storage changes into hydrological models

Heft 51 2015 — Christoph Holst
Analyse der Konfiguration bei der Approximation ungleichmäßig abgetasteter Oberflächen auf Basis von Nivellements und terrestrischen Laserscans

Heft 50 2015 — Lutz Rolf Roese-Koerner
Convex Optimization for Inequality Constrained Adjustment Problems

Heft 49 2015 — Jan Martin Brockmann
On High Performance Computing in Geodesy
Applications in Global Gravity Field Determination

Heft 48 2015 — Judith Leek
The application of impact factors to scheduling VLBI Intensive sessions with twin telescopes

Heft 47 2015 — Thomas Artz
Determination of Sub-daily Earth Rotation Parameters from VLBI Observations

Heft 46 2015 — Roelof Rietbroek
Retrieval of Sea Level and Surface Loading Variations from Geodetic Observations and Model Simulations: an Integrated Approach

Heft 45 2014 — Ehsan Forootan
Statistical Signal Decomposition Techniques for Analyzing Time-Variable Satellite Gravimetry Data

Heft 44 2014	Erich Weiß Lebensbilder der preußischen Verwaltung des 19. und 20. Jahrhunderts im Wandel Eine Sammlung biographischer Miniaturen
Heft 43 2014	Neysa Jacqueline Setiadi Assessing People´s Early Warning Response Capability to Inform Urban Planning Interventions to Reduce Vulnerability to Tsunamis Case Study of Padang City, Indonesia
Heft 42 2013	Nils Leber Entwicklungsperspektiven metropolitaner Peripherien im Rahmen Stadtregionaler Planungs- und Entwicklungsprozesse am Beispiel Nordrhein-Westfalen
Heft 41 2013	Sophie Schetke Socio-environmental impacts of settlement growth under conditions of fostered infill development: a methodological framework for a multicriteria assessment
Heft 40 2013	Ribana Roscher Sequential Learning Using Incremental Import Vector Machines for Semantic Segmentation
Heft 39 2013	Michael Ying Yang Hierarchical and Spatial Structures for Interpreting Images of Man-made Scenes Using Graphical Models
Heft 38 2013	Sabine Daniela Bauer Automatische Detektion von Krankheiten auf Blättern von Nutzpflanzen
Heft 37 2013	Martin Drauschke Ein hierarchischer Ansatz zur Interpretation von Gebäudeaufnahmen
Heft 36 2013	Timo Dickscheid Robust Wide-Baseline Stereo Matching for Sparsely Textured Scenes
Heft 35 2013	Alexander Barth Vehicle Tracking and Motion Estimation Based on Stereo Vision Sequences
Heft 34 2013	Richard Steffen Visual SLAM from image sequences acquired by unmanned aerial vehicles
Heft 33 2013	Till Rumpf Finding spectral features for the early identification of biotic stress in plants
Heft 32 2012	Christian Siemes Digital Filtering Algorithms for Decorrelation within Large Least Squares Problems
Heft 31 2012	Silvia Becker Konsistente Kombination von Schwerefeld, Altimetrie und hydrographischen Daten zur Modellierung der dynamischen Ozeantopographie
Heft 30 2013	Annette Eicker / Jürgen Kusche (eds.) Lecture Notes from the Summer School of DFG SPP1257 Global Water Cycle
Heft 29 2012	Matthias Siemes Ein Beitrag zur koordinatengesteuerten Aussaat von Rübenpflanzen mittels Multi-Sensor-System und Filteransatz
Heft 28 2012	Jörg Schmittwilken Attributierte Grammatiken zur Rekonstruktion und Interpretation von Fassaden

Heft 27 2012	Markus Rembold Die Anerkennung und Feststellung von Grundstücksgrenzen Ein Beitrag zur Entwicklung des Liegenschaftskatasters im Lande Nordrhein-Westfalen in Vergangenheit, Gegenwart und Zukunft
Heft 26 2012	Lihua Li Separability of deformations and measurement noises of GPS time series with modified Kalman filter for landslide monitoring in real-time
Heft 25 2012	Benedikt Frielinghaus Ökonomisches Entscheidungstool zur Wohnbaulandentwicklung Wirtschaftlichkeitsanalysen potenzieller Wohnbauflächen auf der Ebene des Flächennutzungsplanes
Heft 24 2011	Enrico Kurtenbach Entwicklung eines Kalman-Filters zur Bestimmung kurzzeitiger Variationen des Erdschwerefeldes aus Daten der Satellitenmission GRACE
Heft 23 2011	Sarah Böckmann Robust determination of station positions and Earth orientation parameters by VLBI intra-technique combination
Heft 22 2011	20th Meeting of the European VLBI Group for Geodesy and Astronomy Proceedings
Heft 21 2011	Philipp Zeimetz Zur Entwicklung und Bewertung der absoluten GNSS-Antennenkalibrierung im HF-Labor
Heft 20 2011	Alessandra Roy Effects on the Geodetic-VLBI Observables Due to Polarization Leakage in the Receivers
Heft 19 2011	Dietmar Weigt Auswirkungen von Flughäfen insbesondere von Fluglärm auf den Immobilienmarkt am Beispiel des Marktsegments „individuelles Wohnen“
Heft 18 2011	Anno Löcher Möglichkeiten der Nutzung kinematischer Satellitenbahnen zur Bestimmung des Gravitationsfeldes der Erde
Heft 17 2010	Basem Elsaka Simulated Satellite Formation Flights for Detecting the Temporal Variations of the Earth’s Gravity Field
Heft 16 2010	2nd International Conference on Machine Control & Guidance Proceedings
Heft 15 2009	Alexandra Weitkamp Brachflächenrevitalisierung im Rahmen der Flächenkreislaufwirtschaft
Heft 14 2008	Akbar Shabanloui A New Approach for a Kinematic-Dynamic Determination of Low Satellite Orbits Based on GNSS Observations
Heft 13 2008	Frank Friesecke Stadtumbau im Konsens!? Zur Leistungsfähigkeit und Fortentwicklung des städtebaulichen Instrumentariums unter Schrumpfungsbedingungen
Heft 12 2008	Heinz Rütz Zur Kostenanalyse der privaten Umlegung als Teil der konsensualen integrierten Baulandentwicklung

Heft 11 2008	Gaby Alexandra Boele-Keimer Kommunales Kennzahlenmanagement am Beispiel von Vermessungs- und Katasterämtern in Nordrhein-Westfalen
Heft 10 2008	Annette Eicker Gravity Field Refinement by Radial Basis Functions
Heft 9 2008	Torsten Mayer-Gürr Gravitationsfeldbestimmung aus der Analyse kurzer Bahnbögen
Heft 8 2008	Boris Kargoll On the Theory and Application of Model Misspecification Tests
Heft 7 2008	Hamza Alkhatib On Monte Carlo Methods
Heft 6 2008	Klaus Borchard Annäherungen an Städtebau und Raumentwicklung
Heft 5 2008	Jens Jähnke Zur Teilmarktbildung beim Landerwerb der öffentlichen Hand
Heft 4 2008	Atef Abd-Elhakee Makhloof The Use of Topographic Isostatic Mass Information
Heft 3 2008	Markus Vennebusch Singular Value Decomposition and Cluster Analysis
Heft 2 2007	Christian Beder Grouping Uncertain Oriented Projective Geometric Entities
Heft 1 2007	Klaus Börger Geodäsie und Quantenphysik

2699-6685 (Online)